Université de Montréal

The Global Structure of Hot Star Winds:
Constraints from Spectropolarimetry

par
Thomas Eversberg
Département de physique
Faculté des arts et des sciences

Thèse présentée à la Faculté des études supérieures
en vue de l'obtention du grade de
Philosophiæ Doctor (Ph.D.)
en physique

Septembre, 1999

Université de Montréal

Faculté des études supérieures

Cette thèse intitulée:

The Global Structure of Hot Star Winds:

Constraints from Spectropolarimetry

présentée par:

Thomas Eversberg

a été évaluée par un jury composé des personnes suivantes:

Pierre Bastien,   président-rapporteur

Anthony Moffat,   directeur de recherche

Gilles Fontaine,   membre du jury

Karen Bjorkman, examinateur externe

Thèse acceptée le: ....

"Es gibt keine großen Entdeckungen solange noch ein Kind auf Erden Hunger leidet."

("There can't be great discoveries, as long as one child on earth is still starving.")

(Albert Einstein)

Für

Barbara, Johannes und Verena

Contents

List of Figures

List of Tables

RÉSUMÉ

Afin de pouvoir analyser la structure du vent dans les étoiles chaudes, trois projets de recherche différents ont été réalisés:

1. j'ai étudié des sous-structures dans le vent de l'étoile O super-géante ζ Puppis pour obtenir des informations concernant la similarité et le lien évolutif entre les étoiles O et leurs descendantes, les étoiles Wolf-Rayet;

2. j'ai participé à la mise en œuvre du nouveau spectro-polarimètre William-Wehlau pour l'observation de sources ponctuelles. Après une description de l'instrument, les premiers résultats pour un échantillon d'étoiles standard sont donnés. Les problèmes physiques et techniques sont soulignés et différentes solutions sont proposées;

3. je présente l'étude du vent de l'étoile binaire WR+O, γ^2 Velorum, réalisée à partir d'observations obtenues avec le spectro-polarimètre William-Wehlau. Les variations du vent et leur interprétation sont rapportées.

1.) De denses régions éjectées dans le vent de l'étoile O super-géante ζ Puppis

ζ Pup est l'étoile de type O la plus brillante dans le ciel et, par conséquent, une étoile de prédilection pour l'étude des étoiles très massives. Les étoiles de type O sont supposées être les parents des étoiles Wolf-Rayet (WR) (Langer et al. 1994). Les étoiles WR et quelques étoiles de type O montrent des raies d'émission dans leur spectre optique; ces raies sont interprétées comme la manifestation de

xiii

matière éjectée sous forme de vent stellaire. Les étoiles WR sont connues pour présenter, dans leurs fortes raies d'émission, de petites variations stochastiques attribuées à des zones de matière denses éjectées par l'étoile ("clumps"; Moffat & Robert 1992). Ces régions denses sont créées par des chocs dûs à des éléments turbulents qui se déplacent à des vitesses supersoniques dans le vent (Henriksen 1994) et qui sont entretenues par des instabilités radiatives (Owocki 1994). La question demeure à savoir si les étoiles de type O, avec leur vent plus faible mais parfois aussi plus rapide et d'opacité plus faible, présentent des structures similaires dans leurs raies d'émission. Et, si de telles structures existent, quels sont leurs paramètres physiques?

Pour répondre à ces questions, nous avons observé ζ Pup durant deux demi-nuits avec le télescope de 3,6m du CFH (Canada-France-Hawaii). Nous avons obtenu une série temporelle de spectres (environ toutes les 10 minutes) à haut rapport signal sur bruit et à très haute résolution spectrale (~ 1000/pixel = 0.03Å) de la raie en émission He II λ 4686, sur une durée totale de 5 heures par nuit. Après un traitement soigné des données , nous avons additionné tous les spectres et formé ainsi un spectre moyen par nuit qui a été soustrait des spectres individuels. Dans les résidus des spectres, nous avons trouvé des sous-structures qui se déplacent toujours du centre de la raie vers les bords. En outre, toutes ces structures ont tendance à disparaître avec le temps, l'intensité augmentant tout d'abord puis chutant. Nous avons montré que toute la raie He II λ 4686 était affectée par cette variabilité, ce qui est compatible avec la supposition que tout le vent de ζ Pup est également sujet à une telle variabilité. Nous notons que le degré de variabilité est légèrement plus élevé pour l'aile bleue.

Le fait de suivre temporellement la sous-structure la plus évidente nous permet d'estimer son accélération moyenne (Robert 1992). En supposant que les structures les plus rapides se déplacent radialement et que les structures stables en vitesse ont un déplacement quasi-perpendiculaire à la ligne de visée, nous

pouvons estimer leur mouvement selon les différentes valeurs du paramètre β dans l'expression de la loi de vitesse standard[1] et l'angle de visée. Nous avons trouvé que la valeur standard de $\beta = 0.8$ est trop petite dans le cas de l'étoile ζ Pup et que $\beta \sim 1.1$ est plus réaliste (ceci en accord avec le récent travail théorique de Puls et al. 1996).

En considérant des paramètres prédits auparavant pour la vitesse terminale v_∞ (Puls et al. 1996) et le rayon stellaire $R_\star$ (Kudritzki et al. 1983), nous montrons que les régions denses dans le vent de ζ Pup apparaissent à une petite distance de l'étoile $R \sim 1.2R_\star$ et disparaissent à un rayon $R \sim 2R_\star$. Il faut remarquer que cette distance modeste est probablement la raison pour expliquer moins de variabilité dans l'aile rouge de la raie d'émission, par un effet d'ombre lorsque l'étoile elle-même cache une partie du vent variable sur l'aile rouge de la raie.

Les régions denses détectées dans le vent de ζ Pup nous amènent à une des plus importantes conséquences de nos observations. Les simulations théoriques pour la prédiction du taux de perte de masse $\dot{M}$ via l'ajustement de la raie Hα supposent généralement des vents homogènes, sans parties plus denses. Or, nous avons montré que la raie He II, formée encore plus proche de l'étoile que la raie Hα, révèle une structure morcelée du vent. Comme le flux de la raie de recombinaison est proportionel au carré de la densité de matière, les taux de perte de masse théoriques seront sous-estimés lorsque des vents seront supposés être homogènes, au moins dans le cas de ζ Pup, et vraisemblablement pour toutes les étoiles O, si elles montrent également des régions denses dans leur vents étendus.

2.) Le spectro-polarimètre William-Wehlau : détermination des quatre paramètres de Stokes pour la polarisation des étoiles chaudes

---

[1]$v(r) = v_\infty(1 - R_\star/r)^\beta$ avec typiquement $\beta = 0.8$ pour les vents d'étoiles OB. Remarquez que plus β est grand, plus le vent a une vitesse faible à un rayon donné.

Pour l'étude de différents types d'étoiles, les collaborateurs des Universités de Western Ontario, de Brandon et de Montréal ont développé et construit un nouveau polarimètre ajustable au foyer Cassegrain de différents télescopes. Ce polarimètre, couplé à un spectrographe standard, peut devenir un spectro-polarimètre. L'instrument est ainsi appelé spectro-polarimètre William-Wehlau[2]. Nous l'avons utilisé au cours de quatre missions d'observations à l'Observatoire Austral de l'Université de Toronto (University of Toronto Southern Observatory, UTSO) et à l'Observatoire du Mont-Mégantic (OMM).

L'instrument utilise les techniques habituelles pour mesurer la polarisation de la lumière : une lame retardatrice décâle l'angle de phase d'une des deux composantes perpendiculaires de la lumière polarisée d'un angle τ, un polariseur les sépare en deux faisceaux, qui suivent la loi de réfraction. Les deux faisceaux, ordinaire et extraordinaire, sont envoyés au moyen de fibres optiques vers un spectrographe à détecteur CCD. Les deux faisceaux contiennent alors l'information complète polarimétrique et spectrale. Pour la calibration, un prisme de Glan-Taylor, qui polarise linéairement presque 100% toutes les longueurs d'onde de la lumière, peut être inséré devant les lames retardatrices.

L'extraction de l'information polarimétrique est faite suivant la méthode de Mueller. Il sera clairement démontré ci-dessous que, pour la déduction des *quatre* paramètres de Stokes ($I(\lambda)$, $Q(\lambda)$, $U(\lambda)$ et $V(\lambda)$), nous devons utiliser de façon indépendante deux lames quart-d'onde identiques comme retardateurs.

D'après le calcul de Mueller et les règles d'algèbre matricielle, nous pouvons calculer les quatre paramètres de Stokes pour cette configuration avec un retard τ (idéalement de 90°) pour les deux lames quart-d'onde. Soit $\mathbf{A}$ le vecteur initial de Stokes (I,Q,U,V), et soit $\mathbf{A}'$ le vecteur final de Stokes (I',Q',U',V') après passage à travers des deux lames retardatrices de matrices $\mathbf{R}_1$ et $\mathbf{R}_2$ et à travers

---

[2]Du nom du premier responsable du projet William H. Wehlau, qui décéda en février 1995, juste après mon arrivée au Canada.

le polariseur de matrice $\mathbf{P}$, nous avons alors (en écrivant $\mathbf{A}$ et $\mathbf{A}'$ sous forme verticale) :

$$\mathbf{A}' = \mathbf{P} \times \mathbf{R_2} \times \mathbf{R_1} \times \mathbf{A}.$$

En utilisant les matrices pour les lames quart-d'onde (Serkowski 1962) à différentes orientations (ex : $-45°$, $0°$ et $45°$) et suivant l'orientation des deux faisceaux polarisés ($\parallel$ ou $\perp$, i.e. $0°$ ou $90°$, respectivement), nous obtenons trois paramètres de Stokes :

$$q \equiv \frac{Q}{I} = \frac{R_Q - 1}{R_Q + 1}$$

$$u \equiv \frac{U}{I} = \frac{R_U - 1}{R_U + 1}$$

$$v \equiv \frac{V}{I} = \frac{R_V - 1}{R_V + 1} \quad ,$$

où

$$R_Q = \sqrt{\frac{I'_{0,0,\parallel} \cdot I'_{45,45,\perp}}{I'_{0,0,\perp} \cdot I'_{45,45,\parallel}}}$$

$$R_U = \sqrt{\frac{I'_{0,45,\parallel} \cdot I'_{0,-45,\perp}}{I'_{0,45,\perp} \cdot I'_{0,-45,\parallel}}}$$

$$R_V = \sqrt{\frac{I'_{-45,0,\parallel} \cdot I'_{45,0,\perp}}{I'_{-45,0,\perp} \cdot I'_{45,0,\parallel}}} \quad .$$

Les paramètres de Stokes normalisés q, u et v doivent en principe être purement limités par le bruit de photons car toute variation temporelle et un facteur

de gain, indépendants du temps, s'annulent grâce à la double division obtenue. Le paramètre de Stokes I peut être extraît en additionnant deux spectres d'une image donnée, après détermination satisfaisante des facteurs de gain suite à la division par une image de plage-uniforme ("flat-fielding").

Après avoir calculé les valeurs finales $I_\parallel$ et $I_\perp$ attendues pour différentes positions de la lame quart-d'onde avec le prisme de Glan-Taylor (lumière en sortie polarisée linéairement à 100%) et les avoir comparées avec des mesures réalisées à chaque 10°, nous avons trouvé de petites déviations par rapport à la situation idéale. Le retard des deux lames quart-d'onde semble être dépendant de l'angle de position. En appliquant un retard lié à l'angle de position dans l'ajustement par χ^2 de nos données, nous avons découvert la raison de ce comportement dans les lames quart-d'onde elles-mêmes. Nos lames achromatiques sont composées de quatre lames cristallines séparées par de l'air et montées sur une roue dentée. Une composante de la lame 1 est désalignée par rapport à l'axe optique (deux dans le cas de la lame 2). Cela ne devrait pas poser de problème parce qu'un décalage seul ne modifie pas le retard. Cependant, en plus, les lames quart-d'onde dans leur ensemble ont du être imparfaitement montées à l'intérieur des roues dentées, et ainsi l'effet de décalage introduit une dépendance $I(\psi)$ (au lieu de $I(2\psi)$)[3] pour les vecteurs de polarisation.

Nous avons aussi obtenu une série de poses d'étoiles brillantes avec le prisme de Glan-Taylor afin de mesurer l'efficacité totale de l'instrument et l'interférence possible entre différents paramètres de Stokes suivant plusieurs longueurs d'onde. Dans notre cas, l'interférence entre différents paramètres de polarisation montre des structures ondulatoires en fonction de la longueur d'onde, dont l'amplitude ne dépasse jamais 5%. Une partie du décalage différent de zéro dans $\bar{u}$ pourrait être due à une déviation légère dans la rotation du prisme de Glan-Taylor. Nous pouvons cependant exclure ceci comme raison du comportement imparfait du

---

[3] ψ est l'angle de rotation en rapport de l'axe rapide du prisme Wollaston.

retard τ avec l'angle et la longueur d'onde.

Selon le calcul de Mueller et les doubles divisions résultantes, on devrait exécuter chaque opération sur les pixels de la même manière, pour obtenir des spectres q, u et v purement limités par le bruit de photons. Cela signifie que chaque étape mathématique devrait être faite sur les images à 2 dimensions. Cependant, pour réduire l'espace-disque et le temps de calcul, on peut additionner les lignes des images 2D brutes en des spectres 1D et exécuter ultérieurement les opérations dans l'espace 1D. Après avoir appliqué diverses techniques de réduction, nous n'avons trouvé aucune différence significative entre ces deux possibilités. Par simplicité, nous avons décidé de réaliser la réduction de données dans l'espace 1D en utilisant les procédures standards d'IRAF.

Un fait très inquiétant était la variabilité de la polarisation du continu ($\sim$ 1%), pour toutes les étoiles observées, d'une séquence de polarisation à l'autre. Ceci a été trouvé dans nos données obtenues à UTSO aussi bien que dans celles obtenues à l'OMM. Par conséquent, cette déviation doit être d'origine instrumentale. Elle est probablement due à de petites variations, d'une pose à l'autre, de l'illumination globale des deux fibres, dont les surfaces sensibles extérieures ne sont jamais parfaitement uniformes. Cet effet peut se produire en raison de fluctuations du *seeing* ou de légères oscillations du télescope lors du suivi de l'étoile. Nous avons trouvé une confirmation de notre hypothèse en obtenant des plages-uniformes sur l'écran du dome: les fibres sont alors illuminées uniformément et invariablement avec le temps. Les spectres de plages-uniformes à bande large résultants étaient stables, au bruit de Poisson près.

Un problème s'est produit avec les spectres obtenus à UTSO. Des spectres du faisceau extraordinaire étaient légèrement élargis dans la direction de dispersion, de sorte que des structures en forme de chapeau mexicain se sont produites à la position de raies d'absorption après la double division des quatre ouvertures. Nous avons appliqué avec succès une étape de correction à ces données mais la

raison de ce comportement demeure inconnue.

Nous présentons ci-dessous les premiers résultats obtenus avec le spectro-polarimètre William-Wehlau pour quatre étoiles différentes :

1. nous rapportons des structures variant (au-delà de 3σ) avec la polarisation linéaire dans les fortes raies d'émission C III $\lambda\,5696$ et C IV $\lambda\,5802/12$ (voir le Chapitre 4) dans l'étoile binaire WR+O γ^2 Velorum. Nous ne détectons aucune polarisation circulaire significative dans les raies au-dessus du niveau 3σ;

2. nous confirmons les structures significatives de polarisation précédemment détectés (Poeckert & Marlborough 1977) dans la raie de Hα de l'étoile Be lumineuse γ Cas;

3. nous confirmons la polarisation circulaire précédemment détectée (Borra & Landstreet 1980) dans les raies de l'étoile de type Ap, 53 Cam. La structure observée est compatible avec un champ de dipôle de 28 000 Gauss mesuré à cette phase;

4. nous ne trouvons pas d'effet de raie dans la polarisation pour aucun des paramètres de Stokes au-dessus de 0.2% à travers la raie Hα de l'étoile la plus lumineuse du Trapèze d'Orion, la jeune étoile variable O7 θ^1 Ori C.

3.) La spectro-polarimétrie de l'étoile binaire WR+O γ^2 Velorum en fonction de la phase

Nous présentons des observations spectro-polarimétriques à moyenne résolution obtenues avec le nouveau spectro-polarimètre William-Wehlau en fonction de la phase de la binaire WR+O γ^2 Velorum de période P=78.5 jours. Le suivi quasi-simultané de chacun des quatre paramètres de Stokes $I(\lambda)$, $q(\lambda)$, $u(\lambda)$

et $v(\lambda)$ a été effectué à l'UTSO pendant un intervalle de 31 nuits lors du passage au périastre de la binaire.

γ^2 Vel est l'étoile de type Wolf-Rayet la plus lumineuse dans le ciel, et par conséquent, une cible standard pour étudier les phénomènes des WR. Elle est une des étoiles binaires dans lesquelles l'interaction vent-vent se produit. Entre les deux étoiles on s'attend que le vent des deux composantes vienne à un arrêt complet au point de contact. La matière tombe alors suivant une zone de choc en forme de cône et s'enroule autour de l'étoile O avec le plus faible vent (Stevens et al. 1992). Le choc crée une région où la matière est fortement excitée : il se forme des raies de recombinaison en émission qui permettent le refroidissement radiatif rapide du gaz comprimé (par exemple, St Louis et al. 1993). En outre, γ^2 Vel est connue pour montrer une variabilité stochastique de son vent émis (Lépine et al. 1998), présumée être la manifestation de variations de densité (les "clumps", voir chapitre 1). La réduction de données est effectuée de la même manière que décrite au chapitre 2.

γ^2 Velorum a été observée pendant une mission de cinq semaines avec le spectro-polarimètre William-Wehlau monté sur le télescope UTSO de 0,6m, situé au sommet du Cerro Las Campanas, Chili. Nous avons obtenu des spectres pour chacun des quatre paramètres de Stokes en fonction de la longueur d'onde durant 21 nuits entre le 18 février et le 20 mars 1997 autour du passage du périastre ($\Delta\phi \sim \pm 0.2$). De multiples spectres ont été enregistrés environ toutes les 3 minutes. La résolution était d'à peu près 2 Å par pixel dans le domaine de longueur d'onde $5200 - 6000$ Å, couvrant principalement les raies He II $\lambda\,5411$, C IV $\lambda\,5471$, C III $\lambda\,5696$, C IV $\lambda\,5471/12$ et la raie d'émission He I $\lambda\,5875$.

Nous étudions cinq types différents de variabilité dans γ^2 Vel : 1.) le mouvement orbital, 2.) les variations stochastiques à court terme, 3.) les variations périodiques à court terme, 4.) les variations à long terme et 5.) l'excès d'émission C III $\lambda\,5696$.

1.) le mouvement orbital

En appliquant des ajustements gaussiens simples, nous avons estimé les vitesses radiales pour chacune des cinq raies d'émission moyennées par nuit. Comparée au mouvement orbital déjà estimé avec grande précision par l'étude à haute resolution spectrale de Schmutz et al. (1998), la raie C IV λ 5471 dans nos données représente le mieux le déplacement de la composante WR.

2.) les variations stochastiques à court terme

Comme dans le cas de ζ Pup (voir 1.), nous avons aditionné tous les spectres de chaque nuit et avons formé un spectre moyen dans le système de référence de l'étoile WR; ce spectre a alors été soustrait des spectres individuels.

Dans les spectres résiduels, nous avons trouvé des sous-structures stochastiques dans chacune des cinq raies d'émission observées pendant la totalité de la mission, les plus fortes étant visibles dans la raie de C III λ 5696, comme déjà détectées par Lépine et al. (1998). Pendant quelques nuits nous avons trouvé des sous-structures s'éloignant rapidement du centre de la raie, même avec notre résolution spectrale relativement basse. En outre, de fortes modifications de la raie se sont produites d'une nuit à l'autre, révélant des régions variables de forte densité dans le vent. Deux raies dans notre échantillon, He II λ 5411 et He I λ 5875, ont été affectées par l'absorption propre relative à l'étoile de type O : cette absorption stellaire a été particulièrement observée dans la raie He II λ 5411, où l'absorption se déplace de l'aile rouge à l'aile bleue de la raie pendant le passage au périastre. Le fait que toutes les raies d'émission soient stochastiquement structurées implique que le vent entier est morcelé.

3.) les variations périodiques à court terme

Nous avons calculé les spectres de puissance (SP) (Scargle 1982) en utilisant l'algorithme CLEAN, développé par Roberts, Lehár et Dreher (1987), pour chaque pixel et longueur d'onde, afin de rechercher une éventuelle variabilité périodique dans les raies d'émission de γ^2 Vel. Nous n'avons trouvé aucune évidence de variabilité périodique dans les raies, de 6 minutes à 15 jours.

4.) les variations à long terme

Les largeurs équivalentes moyennées nuit par nuit des raies C III λ 5696 et He I λ 5875 dépendent clairement de la séparation des deux composantes de la binaire. Les deux raies sont les plus fortes au moment où les étoiles se rapprochent ($W_\lambda \sim 1/r$), comme précédemment observé par St-Louis (1996). En outre, nous trouvons de grandes variations stochastiques au-delà des erreurs de mesure. Contrairement aux raies C III et He I , les trois autres raies (toutes d'un niveau d'ionisation plus élevé), ne montrent aucune dépendance significative avec la phase orbitale.

5.) l'excès d'émission C III

Avec un certain nombre d'hypothèses, nous avons essayé de distinguer les variations de la forte raie en émission C III λ 5696, constituée de diverses composantes. Le plus important dans notre cas est l'extraction de l'émission due à la zone de choc en forme de cône. Nous avons calculé un profil minimum simple pour chaque nuit de la mission, et avons soustrait ce minimum global à chaque spectre moyenné par nuit. Pour déterminer l'émission due au choc, nous avons mesuré des vitesses et des largeurs pondérées de la raie observée à différentes nuits et avons appliqué à nos données[4] le modèle de choc conique développé par Lührs (1997). En utilisant divers paramètres connus pour l'orbite et le choc, nous trouvons un assez bon accord entre le modèle et les observations, bien que des

---

[4]Les vitesses et les largeurs pondérées sont un compromis en raison du vrai minimum de la raie qui est inconnu et de la nature fortement compliquée du C III

xxiii

déviations systématiques se produisent. En comparant notre résultat à une analyse indépendante réalisée par Schweickhard et al. (1998), nous concluons que l'équilibre variable du vent (cf. Gayley et al. 1997) dans ce système avec une orbite elliptique peut provoquer la chute du vent de l'étoile WR sur la surface de l'étoile O et accroître l'émissivité de la composante due à la collision vent-vent (par conséquent, augmenter la largeur équivalente W_λ à certaines phases). Les émissions supplémentaires dans l'aile bleue qui en découlent et un décalage du profil WR vers les vitesses négatives sont clairement vus dans nos données aussi bien que dans celles de Schweickhard et al. (1998).

SUMMARY

I present three different projects to investigate the wind structure in hot stars.

1. The O supergiant ζ Puppis was examined for substructures in its wind to obtain information about the similarity and evolutionary connection between O stars and their descendants, the Wolf-Rayet stars.

2. The newly constructed and commissioned William-Wehlau spectropolarimeter for the observation of point sources in the sky is introduced. First results for a number of different prototype stars are presented. Technical and physical problems are highlighted and different solutions are suggested.

3. I present an investigation of the wind of the WR+O binary γ^2 Velorum with the William-Wehlau spectropolarimeter. The observation of various wind variabilities and their interpretation is reported.

1.) Outmoving clumps in the wind of the hot O supergiant ζ Puppis

ζ Pup is the brightest early type O star in the sky and, hence, a standard target for O star research. O stars are assumed to be the progenitors of Wolf-Rayet (WR) stars (e.g., Langer et al. 1994). WR stars and some O stars show emission lines even in their optical spectra, which is interpreted as the manifestation of outmoving material in the form of a stellar wind . WR stars are known to show stochastically varying small-scale features in their strong emission lines, interpreted as outmoving regions of higher density (clumps; Moffat & Robert 1992), created by shocks due to supersonic turbulent velocities in the wind (Henriksen

1994) and driven by radiative instabilities (Owocki 1994). The question remained if O stars, with their weaker but sometimes faster winds of lower opacity, show similar features in their emission lines. And if such features exist, what are their physical parameters?

To answer these questions we monitored ζ Pup during parts of two nights at the 3.6m Canada-France-Hawaii Telescope. We obtained high signal-to-noise and ultra-high spectral resolution ($\sim 1000/\text{pixel} = 0.03\text{\AA}$) time-series (every $\sim$ 10min) spectra of the He II $\lambda 4686$ emission line during five hours each night. After careful data reduction we co-added all nightly spectra and calculated a mean spectrum for each night, which was then subtracted from the individual spectra. In the resulting residual spectra we found substructures always moving away from the line center to the blue/red wing of the line. In addition, all features tend to smear-out with time, while the intensity first rises, then drops. We found that the whole He II $\lambda 4686$ line is affected by this variability, which is compatible with the assumption that the whole wind of ζ Pup is affected by such variability. We note that we find a slightly larger degree of variability in the blue line wing.

Tracing the most prominent subfeatures in time enables us to estimate their average acceleration (cf. Robert 1992). Assuming that the fastest features are moving approximately in the line-of-sight (LOS), whereas stable features are moving approximately perpendicularly to the LOS, we are able to investigate their behavior with respect to different 'β-values' of the standard velocity law[5] and angles to the LOS. We discover that the standard β-value of $\beta = 0.8$ is too small for ζ Pup and $\beta \sim 1.1$ is more applicable (in agreement with recent theoretical work of Puls et al. 1996).

Applying previously predicted stellar parameters for the terminal velocity v_∞ (Puls et al. 1996) and the stellar Radius $R_\star$ (Kudritzki et al. 1983) we show

---

[5]$v(r) = v_\infty (1 - R_\star/r)^\beta$ with $\beta = 0.8$ as the standard value for OB-star winds. Note that the larger is β, the slower is the wind at a given radius.

that the clumps in ζ Pup appear at very small stellar radii of $R \sim 1.2 R_*$ and disappear at $R \sim 2 R_*$. Note that this small distance is probably the reason for smaller variability in the red line wing, introduced by a shadow effect, when the star itself hides part of the variable wind in the red.

The observed clumps lead to the most intriguing consequence of our observations: Theoretical simulations for the estimation of the mass-loss rate $\dot{M}$ on the basis of Hα line fitting, generally assume smooth winds, unaffected by clumping. We show that the He II line, formed even closer to the star than Hα, shows a clumpy wind structure. Because of the fact that recombination line flux is dependent on the square of the material density, theoretically calculated mass-loss rates will be overestimated when smooth winds are assumed, at least for ζ Pup, and possibly for all O stars, if they also show clumping in their extended winds.

2.) The William-Wehlau Spectropolarimeter: Observing Hot Stars in all Four Stokes Parameters

For the investigation of various types of stars, the University of Western Ontario, Brandon University and Université de Montréal designed, developed, constructed and commissioned a new polarimetric unit for use at the Cassegrain foci of different telescopes, which, together with a standard spectrograph, can be used as a spectropolarimeter. This instrument is called the William-Wehlau spectropolarimeter[6] and we used it during four different observing runs at University of Toronto Southern Observatory (UTSO) and Observatoire du Mont Mégantic (OMM).

The instrument applies standard techniques to measure polarized light: Generally, a retarder shifts the phase angle of one of the two perpendicular components of a polarized beam by an angle τ, a beamsplitter (or polarizer) separates

---

[6] After the initial prime investigator William H. Wehlau, who died in February 1995, just after I arrived in Canada to start this project!

these two beams, according to the refraction law. The two beams, the ordinary and the extraordinary beam, are fed into a CCD spectrograph via optical fibers and dispersed as two different intensity spectra side by side. The two beams contain the complete polarimetric and intensity information. For calibration purposes a removable Glan-Taylor prism, which produces very nearly 100% linearly polarized light at all wavelengths can be inserted in front of the retarders.

Extraction of the polarimetric information is done with the Mueller calculus. It will be clear further below that for the extraction of *all four* Stokes parameters $I(\lambda)$, $Q(\lambda)$, $U(\lambda)$ and $V(\lambda)$ we have to use two identical but independent quarter-wave plates in tandem as retarders.

Following the Mueller calculus and the rules for matrix algebra, we can calculate the four Stokes' parameters for this arrangement with retardance τ (ideally 90°) for both QWP's. With $\mathbf{A}$ the input Stokes vector (I,Q,U,V) and $\mathbf{A}'$ the output Stokes vector (I',Q',U',V') after passing through the retarder plates with matrices $\mathbf{R_1}$ and $\mathbf{R_2}$, and the polarizer with matrix $\mathbf{P}$, we have (writing $\mathbf{A}$ and $\mathbf{A}'$ in vertical form):

$$\mathbf{A}' = \mathbf{P} \times \mathbf{R_2} \times \mathbf{R_1} \times \mathbf{A}.$$

Using the matrices for quarter-wave plates (Serkowski 1962) at different angular positions with respect to the fast axis of the beam-splitter (e.g., $-45°$, $0°$ and $45°$) and orientation of the two polarizer beams ($\parallel$ or $\perp$, i.e. $0°$ and $90°$, respectively), we obtain the three Stokes polarization parameters as

$$q \equiv \frac{Q}{I} = \frac{R_Q - 1}{R_Q + 1}$$

$$u \equiv \frac{U}{I} = \frac{R_U - 1}{R_U + 1}$$

$$v \equiv \frac{V}{I} = \frac{R_V - 1}{R_V + 1} \quad ,$$

with

$$R_Q = \sqrt{\frac{I'_{0,0,\parallel} \cdot I'_{45,45,\perp}}{I'_{0,0,\perp} \cdot I'_{45,45,\parallel}}}$$

$$R_U = \sqrt{\frac{I'_{0,45,\parallel} \cdot I'_{0,-45,\perp}}{I'_{0,45,\perp} \cdot I'_{0,-45,\parallel}}}$$

$$R_V = \sqrt{\frac{I'_{-45,0,\parallel} \cdot I'_{45,0,\perp}}{I'_{-45,0,\perp} \cdot I'_{45,0,\parallel}}} \quad .$$

The normalized Stokes polarization parameters q, u and v should be purely photon-noise limited because all time dependent variations and time independent gain factors cancel out due to the double divisions above. Stokes I can be obtained by a simple addition of the two spectra on a given image, after appropriate determination of the gain factors by flat-fielding.

Calculating the expected output for $I_\parallel$ and $I_\perp$ for different quarter-wave plate positions with the Glan-Taylor prism (100% linearly polarized light as input) and comparing them with measurements for every 10°, we found small deviations from the ideal situation. The retardation of both quarter-wave plates seems to be position-angle dependent. By applying an angle-dependent redardation in the form of a χ^2 fit to our data, we found the reason for this behavior in the quarter-wave plates themselves. Our achromatic plates consist of four air-spaced crystals, mounted in a worm-gear unit. One (two) layers of plate one (two) are tilted with respect to the optical axis. This should actually be no problem because a tilt alone does not change the retardance. In addition however, the quarter-wave plates as a whole must have been imperfectly mounted in the worm-gear units, so that a wobbling effect introduced a dependence $I(\psi)$ (instead of $I(2\psi)$)[7] for

---

[7] ψ is the rotation angle of the quarter-wave plates with respect to the fast axis of the Wollaston prism

the polarization vectors.

We also obtained a number of exposures of bright stars with the Glan-Taylor prism to measure the overall efficiency and possible cross-talk between different Stokes parameters at different wavelengths. In our case, cross-talk between different parameters shows wavy structures as a function of wavelength, with an amplitude which never exceeds $\sim 5\%$. Some of the non-zero offset in $\bar{u}$ might be due to a slight misalignment in the rotation axis of the Glan-Taylor prism. We can however exclude this as the reason for the imperfect behavior of retardance τ with angle and wavelength.

According to the Mueller calculus and the resulting double divisions, one should perform each pixel operation in the same manner, to obtain purely photon-noise limited q, u and v spectra. This means, each mathematical step should be done on 2D images. However, to reduce necessary hard-disk space and time consumption, one can try to collapse raw 2D apertures to 1D spectra and subsequently perform the operations in 1D space. Applying various techniques of different reduction parameters, we found no significant difference between these two possibilities. For the sake of simplicity we decided to perform the data reduction in 1D with standard IRAF packages in chapter 2.

A very disturbing fact was the variability of the continuum polarization ($\sim$ 1%) from one polarization sequence to the next for all observed stars. This was found in our data obtained at UTSO as well as in those from OMM. Thus, this scatter must be of instrumental origin. This is probably due to small variations from one exposure to the next in overall illumination of the two fibers, whose spatial surface sensitivities are not uniform. This can happen either due to seeing fluctuations or tracking of the telescope. We found support for our assumption by obtaining dome flats, which illuminated the fibers uniformly and invariably with time. The resulting flat field broadband output spectra were stable within the Poisson noise level.

One problem occurred only in spectra obtained at UTSO. Spectra of the extraordinary beam were slightly broadened in dispersion direction, so that Mexican hat features occurred at absorption line positions after double division of the four individual spectra. We successfully applied a correction technique to these data but the reason for this behavior remains unexplained.

We present first results for four different prototype stars, obtained with the William-Wehlau spectropolarimeter:

1. We report varying linear polarization features above the 3σ level across the prominent emission lines of C III $\lambda\,5696$ and C IV $\lambda\,5802/12$ (two lines unresolvable) (see chap. 4) in the WR+O binary γ^2 Velorum. We detect no significant circular polarization across the lines above the 3σ level.

2. We confirm previously detected (Poeckert & Marlborough 1977) significant polarization features across the Hα line of the bright Be star γ Cas.

3. We confirm previously detected circular line polarization in the Ap star 53 Cam (Borra & Landstreet 1980). The observed feature is consistent with a dipole field of 28 000 Gauss measured at this phase.

4. We find no line effect in any Stokes parameter above 0.2% across the Hα line of the brightest Orion Trapezium star, the young, variable O7 V star θ^1 Ori C.

3.) Phase-dependent Spectropolarimetry of the WR+O Binary γ^2 Velorum

We present medium resolution phase-dependent spectropolarimetric observations obtained with the new William-Wehlau spectropolarimeter for the 78.5 d WR+O binary γ^2 Velorum. Quasi-simultaneous monitoring of all four Stokes pa-

rameters $I(\lambda)$, $q(\lambda)$, $u(\lambda)$ and $v(\lambda)$ was carried out at UTSO over an interval of 31 nights centered on periastron.

γ^2 Vel is the brightest WR star in the sky, and hence, a standard target for investigating WR phenomena. It is one of a number of binaries where wind-wind interaction occurs. Between the two stars the wind of both components is expected to come to a complete stop at the stagnation point. Material then flows along a shock-cone that wraps around the weaker-wind O star (Stevens et al. 1992). The shock region creates highly excited material that leads to recombination excess emission via fast radiative cooling of the shocked gas (e.g., St.-Louis et al. 1993). In addition, γ^2 Vel is known to show stochastic wind variability in its outmoving wind (Lépine et al. 1998), presumed to be the manifestation of density variations (clumps, see 1.). The data reduction is carried out in the same manner as described in (2).

γ^2 Velorum was observed during a five week run with the William-Wehlau spectropolarimeter mounted on the 0.6m telescope UTSO on Cerro Las Campanas, Chile. We obtained spectra in all four wavelength-dependent Stokes parameters during 21 nights between 1997 Feb 18 and March 20 within $\Delta\phi$ about ±0.2 of periastron passage. Individual spectra were obtained every ~ 3 minutes. The 3-pixel spectral resolution was about $6\,\text{Å}$ in the wavelength range $5200 - 6000\,\text{Å}$, covering mainly the He II $\lambda\,5411$, C IV $\lambda\,5471$, C III $\lambda\,5696$, C IV $\lambda\,5802/12$ and He I λ 5875 emission lines.

We investigate five different types of variability in γ^2 Vel: 1.) orbital motion, 2.) stochastic short-term variations, 3.) periodic short-term variations, 4.) long-term variations and 5.) C III $\lambda\,5696$ excess.

1.) – Orbital motion

By applying single Gaussian velocity fits we estimated the LOS velocities for all five observed nightly averaged emission lines. Compared with the orbital motion, already estimated with high accuracy from the high resolution study of Schmutz et al. (1998), the C IV $\lambda 5471$ line in our data represents best the orbital motion of the WR component

2.) – Stochastic short-term variations

Analogous to the procedure for ζ Pup (see 1.) we co-added all nightly spectra and calculated a mean spectrum for the whole run in the frame of the WR star, which was then subtracted from the individual spectra.

In the resulting residual spectra we found stochastic substructures in all five observed emission lines during the whole run, most prominent in C III $\lambda 5696$, as already detected by Lépine et al. (1998). During some nights we found fast substructures moving away from line center, even with our relatively low spectral resolution. In addition, strong contrast changes occurred from night to night, pointing to strong density changes in the wind. Two lines in our sample, He II $\lambda 5411$ and He I $\lambda 5875$, were affected by the respective O star absorption, most clearly seen in He II $\lambda 5411$, where the absorption moves from the red to the blue line flank during periastron passage. The fact that all emission lines are stochastically structured implies that the whole wind is affected by clumps.

3.) – Periodic short-term variations

We have calculated power spectra (Scargle 1982) including the CLEAN algorithm, developed by Roberts, Lehár, & Dreher (1987), for each pixel within our observed wavelength range, to search for periodic variability in the emission lines of γ^2 Vel. We found no evidence for any periodic variability in the lines, from 6 minutes to 15 days.

4.) – Long-term variations

Nightly-averaged equivalent widths for C III $\lambda\,5696$ and He I $\lambda\,5875$ are clearly dependent on the separation of the two binary components. Both lines are strongest at closest aproach ($W_\lambda \sim 1/r$), as previously observed by St.-Louis (1996). In addition, we find large stochastic variations exceeding the measurement errors. In contrast to C III and He I , the three other lines, all of higher ionization level, show no significant dependence on orbital phase.

5.) – C III excess

With a number of assumptions we tried to disentangle the variations in the prominent C III $\lambda\,5696$ line, consisting of various line components. Most important in our case is the extraction of shock-cone emission. We applied a pure minimum intensity profile for the whole run, and subtracted this global minimum from each nightly average spectrum. To test for shock-cone emission we measured weighted line velocities and widths and applied the shock-cone model developed by Lührs (1997) to our data[8]. Using various known parameters for the orbit and the shock-cone we find fair agreement between the model and our data, although systemetic deviations do occur. By comparing our result with an independent analysis performed by Schweickhardt et al. (1998), we conclude that the changing wind momentum balance (cf. Gayley et al. 1997) in this elliptical orbit system may provoke crashing of the WR wind onto the O star surface and increased emissivity from the wind-wind collision component (hence, an increase in W_λ at certain phases). The resulting change of mass load into the wind-wind collision zone and thus emissivity may create extra blueshifted emission and a shift of the WR profile to negative velocities is clearly seen in our data as well as in those of Schweickhardt et al. (1998).

---

[8]Weighted line velocities and widths are a compromise because of the unknown true minimum of the line and the highly complicated nature of C III $\lambda\,5696$.

INTRODUCTION

Extended atmospheres of O and WR stars

The physics of stars in the upper left Herzsprung-Russel Diagram like O, B and Wolf-Rayet stars, is of great interest for various reasons. These stars are massive, hot and very luminous. Normally, stellar spectra show absorption lines, as does our Sun. They are formed in a thin layer called the photosphere, where continuum light from below is absorbed. Two typical examples of spectra of massive stars are shown in Fig. 0.1.
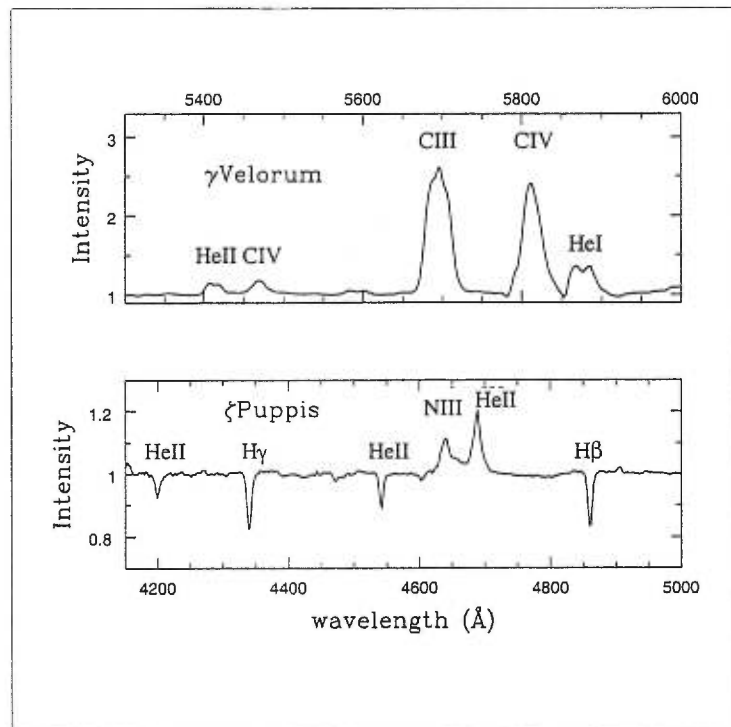

Figure 0.1. Spectra of ζ Puppis (bottom) and γ^2 Velorum (top)

The most striking evidence for material around stars are the emission lines in hot star spectra. Hot star spectra consist of Hydrogen and various ionized common species of elements, e.g., Helium, Silicon, Carbon and Nitrogen. Atomic transitions of highly ionized elements are found, which shows that high temperatures are present.

The key parameters here are the stellar mass and radius. The larger the stellar mass and the smaller the radius, the higher is the stellar temperature. If the temperature is sufficiently high and the gas density is low enough, the radiation pressure can dominate over gravity. The corresponding threshold is given by

$$L_{ed} = \frac{4\pi G c}{\bar{\kappa}} M$$

with $\bar{\kappa}$ as the average opacity in the wind. L_{ed} is called the Eddington luminosity or Eddington limit. It is the maximum radiative luminosity that a star can have and still remain in hydrostatic equilibrium. If $L > L_{ed}$, the atmosphere becomes unstable and extreme mass-loss in the form of a radiatively driven outward moving stellar wind must occur. Stellar winds can also occur at $L \lesssim L_{ed}$, however. As one can see from Fig. 0.1, all emission lines are very broad and show non-Gaussian form. In fact, this shows that unstable, outmoving atmospheres of high velocities and large mass-loss rates are present.

Evolutionary aspects

O stars are the most permanent luminous known stellar objects. They exhibit strong, fast stellar winds of relatively low opacity, driven by their strong radiation field. Luminosities are found to be up to $10^6 L_{\odot}$ (for O supergiants) with mass loss rates $\dot{M}$ of up to $5 \times 10^{-6} M_{\odot}$. Terminal wind velocities (V_{∞}) of up to 2000 km/s are found. Estimated surface temperatures are found to lie up to $\sim 50\,000$ K. A number of different spectroscopic line effects have been discovered

so far, leading to the image of dramatic changes within O star atmospheres. In addition, O stars are the major contributors to the radiation field of their respective galaxy. Because of this large-scale influence, it is of great importance to understand their general behavior.

Intense emission lines of various ionized elements are the spectral characteristics of **Wolf-Rayet stars**. Beals (1929) realized that an extended, and rapidly expanding atmosphere is responsible for these features. Among all stable hot stars, WR stars reveal the strongest mass loss via wind mechanisms. Typical mass loss rates range from $(2 - 10) \times 10^{-5} M_\odot \, yr^{-1}$, with wind velocities of 1000 - 2500 km/s (Willis 1991). The Wolf-Rayet winds are mostly optically thick, so that the surface is not visible. This means that the connection of spectral classification to photospheric core temperature is not possible as for normal stars via MK classification, and the WR classification is purely spectroscopic. WR stars are highly luminous, evolved, hot, massive stars, in the final state of nuclear He burning.

Already Chandrasekhar (1934) discussed the origin of WR stars and their exact evolutionary scenario is still in discussion. However, since Conti's proposal in 1976 based on observational data, the general idea of O type progenitors is widely accepted. Chiosi & Meader (1986) suggest that WR stars are descendants of OB stars, Langer et al. (1994) suggest for $M_{ZAMS} \geq 40 M_\odot$ the scenario O $\rightarrow$ Of $\rightarrow$ H-rich WN $\rightarrow$ LBV $\rightarrow$ H-poor WN $\rightarrow$ H-free WN $\rightarrow$ WC $\rightarrow$ SN, and Crowther et al. (1995) predict O $\rightarrow$ Of $\rightarrow$ WNL+abs $\rightarrow$ WN7 $\rightarrow$ WC $\rightarrow$ SN. If these paths are correct, we should expect that similar or even the same atmospheric effects play a role in both stellar types. This is important to know, not only for itself but for possible information about WR parameters. As mentioned above, the WR photosphere is hidden by a dense wind and information about the masses, the initial luminosities, effective temperatures, radii and mass-loss rates are difficult to obtain. Especially the mass-loss rate $\dot{M}$ is a critical point.

For instance, due to clumping, already observed in WR star spectra, $\dot{M}$ may be smaller than conventionally predicted. This would have consequences for the lifetime of the stage in which a star can be found.

The latest review about hot massive stars and their classification is given by van der Hucht (1996). One of the most intriguing questions is the so-called *momentum problem* for WR stars. We define the ratio η by:

$$\eta = \frac{\dot{M} V_\infty}{L/c} \equiv \frac{\text{Wind momentum}}{\text{Radiation momentum}} \qquad (0.1)$$

This number gives an indication of the efficiency at which radiation momentum is imparted to the gas. Single scattering delivers $\eta \leq 1$. Because $\eta \gg 1$ for many Wolf-Rayet stars it was not clear for a long time how the winds of WR stars are accelerated to their terminal velocities. The most probable answer is that multiple scattering must play a role.

During the last few years, evidence has been growing that the winds of hot stars are mostly not spherically symmetric. The prototypes having well known large-scale deviation from spherical symmetry are the Be stars with extended stable equatorial disks of mainly Hydrogen. An important question is: do other stellar atmospheres also show preferred geometries? In addition, it is shown that some stars show sub-structures across their absorption and emission lines. This is found especially in the optically thick winds of Wolf-Rayet stars (Lépine et al. 1998), as shown in Fig. 0.2 for the star γ^2 Vel.

Such perturbations in hot star spectra are believed to be created in the outmoving wind itself. The observed flux of a recombination line is proportional to the square of the material density. This means that if the emission line flux varies, material density of the emission line source should vary too. For this reason, the observed stochastic line sub-structures in hot star spectra are believed to be formed in a wind containing various density enhancements, also called clumps,
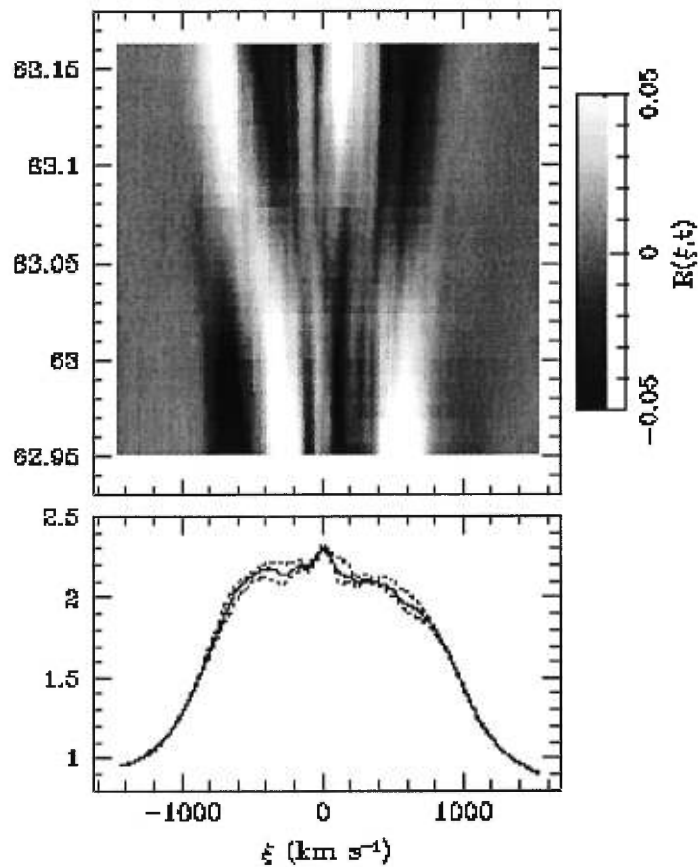
Figure 0.2. Outmoving substructures in the C III λ 5696 line of γ^2 Velorum (Lépine et al. 1998). Greyscale plot of nightly residuals from the mean rectified spectrum of one night plotted in time vs. line-of-sight velocity.

blobs and shocks[9]. One of the most plausible explanations for this phenomenon was suggested by Henriksen (1994). Supersonic velocities in the wind produce internal shocks, resulting in turbulence and density variations. Such shocks in the wind could be generated due to radiative instabilities, as suggested by Owocki (1994).

---

[9]Varying nomenclature is a sign that the true nature of such line-features is still in discussion.

If clumping is present, the theoretical smooth-wind approximation for the calculation of the mass-loss rate will not be correct. Clumped winds with regions of higher density produce increased flux due to the ρ^2 dependence, even when the mass-loss rate is the same as in the case of a smooth wind. Or vice versa, clumped material can produce the same flux as a more massive smooth wind. Thus, in the case of clumping, classical mass-loss rates based on the assumption of a smooth wind, are overestimated.

The aspects above lead to two important questions:

- Do O stars show similar small-scale structures (clumping) in their winds as do WR stars, and are their calculated mass-loss rates overestimated?

- Can we obtain information about the hidden surfaces of WR stars by constraints from the progenitors, the O stars?

Polarimetric aspects

(A) **Intrinsic linear polarization** – Intrinsic linear polarization of early-type stars arises mainly from Thomson (electron) scattering of stellar light. The fundamental condition to show any intrinsic linear polarization and/or polarimetric variability is a non spherical stellar atmosphere. If spherical or circular geometry in projection (e.g. a cylinder seen along the axis as for an equatorial disk if seen pole-on) prevails, all polarization due to Thomson scattering cancels out. But if any deviation from a radial sphere or circular geometry in projection exists (e.g., an equatorial disk not seen pole-on or localized regions of higher ionic or atomic density, so called *blobs*, or only density enhancement above the equator) an observer should be able to detect intrinsic linear polarization. The electron scattering process itself forms linearly polarized light. If an incoming beam is scattered at an electron, the electron begins to vibrate and re-emits (or scatters) a beam, which is polarized perpendicular to the scattering plane. The

scattering process changes the length of the electric vector as described in Fig. 0.3
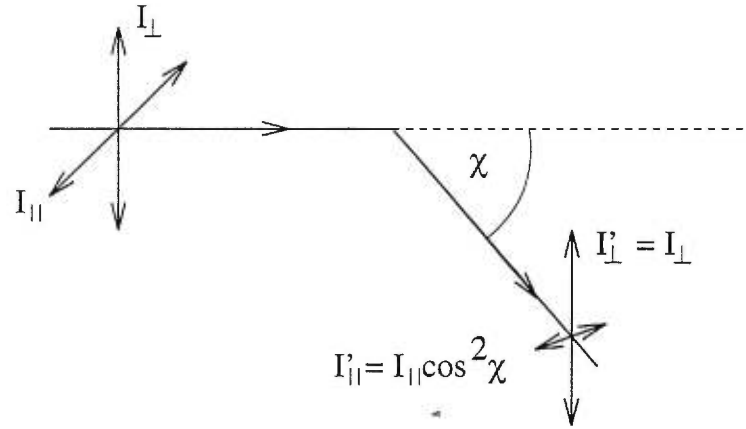

Figure 0.3. The electron scattering process. The intensity of the electric vector is reduced by $\cos^2 \chi$ for the component parallel to the scattering plane which is in the same plane as the one which contains the outgoing beam toward the observer. The perpendicular component is unaltered after scattering. χ is the scattering angle in the scattering plane, containing the original beam, the scatterer and the observer.

The degree of polarization after scattering depends on the scattering angle χ:

$$P = \frac{1 - \cos^2 \chi}{1 + \cos^2 \chi}.$$

Chandrasekhar (1946) predicted intrinsic polarization values for a stellar disk to be zero at the center and as high as $\sim 11\%$ at the limb. The electric vector then vibrates tangentially to the stellar surface. To estimate the asymmetric geometry of the star-envelope system via spectropolarimetry one has to consider the expected degree of polarization.

Polarization in early-type stars often yields intrinsic variability in time and sometimes with wavelength. Nordsieck et al. (1992) showed four different expla-

nations how the observed polarization becomes wavelength dependent and also
Schulte-Ladbeck et al. (1992c) gave a brief explanation for this behavior and the
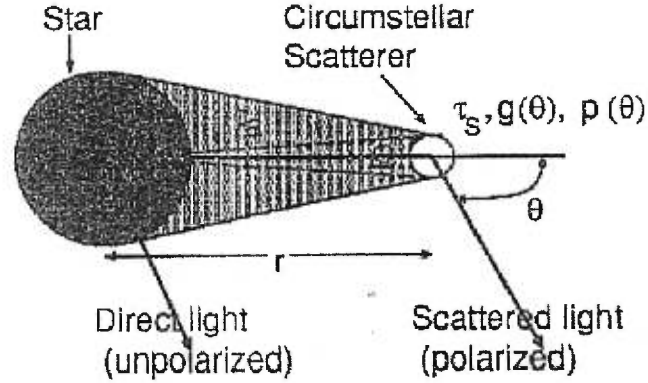physical reasons (Fig. 0.4).

Figure 0.4. Intrinsic polarization from circumstellar envelopes (Nordsieck et al.,
1992).

If the star and the scattered light are both in the observer's beam, and
the polarized scattered light L_{scat} is small compared to the direct unpolarized
starlight $L_\star$, the observed degree of polarization p_{obs} is

$$
\begin{aligned}
p_{obs} &= p(\Theta)L_{scat}/(L_\star + L_{scat}) \\
&\approx \frac{\Omega}{4\pi}p_{max}g(\Theta)\tau_s(1-\tau_s)D(r)\sin^2\Theta,
\end{aligned}
$$

where Ω is the solid angle subtended at the star by the scatterer, p_{max} is the
polarization near $\Theta = 90°$, $g(\Theta)$ is the scattering efficiency, τ_s is the scattering
optical depth, and $D(r)$ is the geometry dilution due to the finite star size. Fol-
lowing this idea the four basic ways of making p_{obs} wavelength dependent are
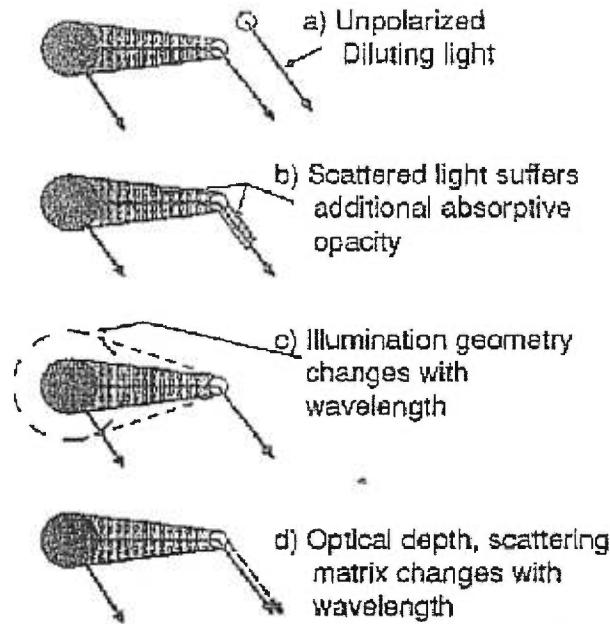illustrated in Figure 0.5.

Figure 0.5. Sources of spectropolarimetric features (Nordsieck et al., 1992).

(a) Unpolarized light L_{dil} not originating in the star (e.g., nebular emission from circumstellar material) dilutes the polarized light: $p_{obs} = p(\Theta)L_{scat}/(L_\star + L_{scat} + L_{dil})$, where $L_{dil}(\lambda)$ is wavelength dependent.

(b) Absorptive opacity may reduce scattered light more than direct starlight: $p_{obs} \sim 1 - \tau_a(\lambda)$ and we observe polarization with features that are weak or do not exist in the stellar spectrum.

(c) Different illumination geometry in different wavelengths (e.g., due to limb darkening): $p_{obs} \sim D(\lambda) \sin^2 \Theta(\lambda)$.

(d) The scattering process may itself be wavelength dependent, e.g., due to dust or atomic scattering: $p_{obs} \sim p_{max}(\lambda)g(\Theta, \lambda)\tau_s(\lambda)$. However, this is ruled out for hot stars, due to the "grey" Thomson-scattering process.

An axisymmetric scattering envelope leads to $p_{obs} \sim \tau_s(1 - 3\gamma)\sin^2 i$, where γ is an envelope shape factor (for a spherical envelope $\gamma = 1/3$; $\gamma = 0$ (1) for a flat (oblate) disk), i is the inclination, and $\tau_s = \sigma_T \int_V N_e(R)dV$, with the electron density distribution $N_e(R)$. The Thomson-scattering cross section is wavelength independent and the scattering process does not alter the scattered spectrum. Chandrasekhar suggested that the best condition for observable polarization from the limbs of early-type stars should be the symmetry breaking effect of the eclipse by a companion. This phenomenon has been reported by Robert et al. (1990) and extended by St-Louis et al. (1993) for the WR binary V444 Cygni. An example for wavelength dependence for the WR star EZ CMa is given in Fig. 0.6.

A common problem in observations of intrinsic polarization is that of small contrast. Assuming an interstellar polarization of 1%, an intrinsic stellar continuum polarization of about 0.1% and line polarization of 0%, with a flux-to-continuum ratio in the net line of 10, then the continuum polarization is 1.1% and the net line polarization is 1.01%. For a 3σ detection of this feature we need an internal accuracy of at least 0.03% per pixel. This means that a signal-to-noise ratio of 3000(!) is necessary. So, to observe not only bright but also faint stars and to understand the nature of the variability we need a large telescope for a reasonably long run.

It seems clear that deviations from spherical wind symmetry in the form of equatorial disks (Be stars, e.g., Hanuschik 1996), large-scale and small-scale wind structures (Wolf-Rayet stars, e.g., Schulte-Ladbeck et al. 1991; Moffat et al. 1988) and now also in at least one O supergiant (see chapter 1), are common phenomena in the hot star domain. Following this aspect and Nordsieck's considerations above, an interesting consequence follows from non-spherical symmetry, and hence, non-spherical density distribution, by considering polarization effects. If we are able to measure intrinsic linear polarization, we should be able to obtain information about the material density distribution around the star, as long as it
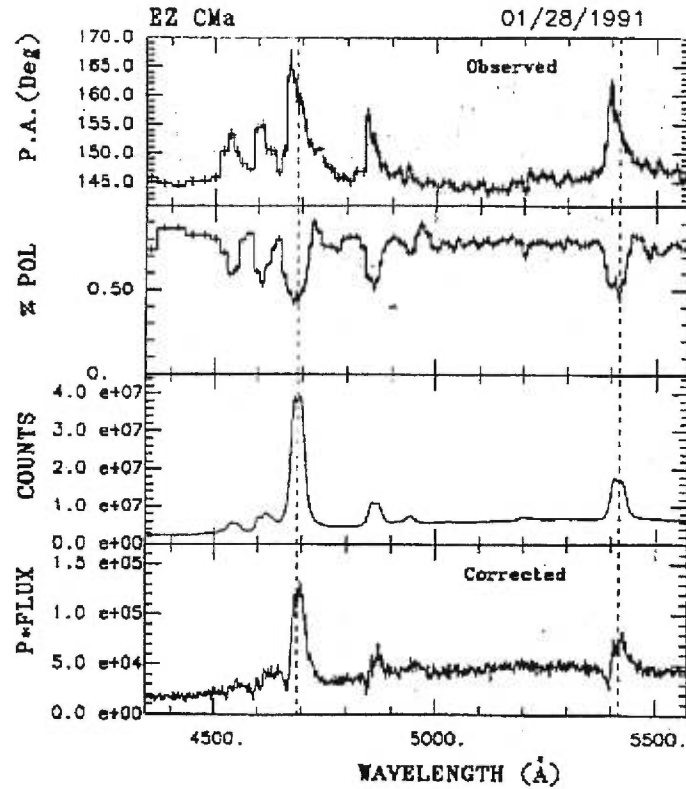
Figure 0.6. Total counts, polarization in percent, and position angle in degree versus wavelength for EZ CMa, measured at the AAT. Error bars are $\pm 1\sigma$. Changes across line profiles, which are different in flux and polarization, can be seen. P*FLUX is the spectrum of the polarized counts after correction for interstellar polarization. Dashed lines mark the positions of the observed line centers for He II $\lambda 4686$ Å and $\lambda 5412$ Å in the count spectrum. (Schulte-Ladbeck et al., 1992c).

is sufficiently ionized to produce enough free electrons to scatter light.

Two examples are:

- Linear spectropolarimetry at high signal-to-noise ratio for the Hα line of ζ Pup was presented by Harries & Howarth (1996). Their polarization measurements give values smaller than 0.1% for q and u in the lines as well as in the continuum (see page 23).

- In the first two of a number of spectropolarimetry papers, Schulte-Ladbeck et al. (1990) published the discovery of linear polarization variations in the He II λ 4686 wings of EZ CMa obtained at Pine Bluff Observatory in Wisconsin. They detected polarization across the emission lines, like those seen in Be stars. This leads to the assumption that also in this WR star an axisymmetric, electron scattering envelope could be the reason for this behavior. From their data they suggest a rotating and expanding disk-like density distribution around EZ CMa.

(B) Intrinsic circular polarization – The production of linearly *and* circularly polarized light is possible via cyclotron emission. A free electron captured by a magnetic field spins around the field lines and emits Bremsstrahlung which is polarized. The emitted wave oscillates perpendicularly to the field direction. In the direction of the field the electrons emit circularly polarized light. One refers to a transverse and a longitudinal field for the field components perpendicular and parallel to the observer's direction, respectively. This means that if we see circularly (linearly) polarized light, we look "onto" the electrons with their spin parallel (perpendicular) to the line-of-sight. As a result, circularly polarized light is a relatively unambigous indicator for intrinsic magnetic fields. However, measuring this polarization is a rather delicate business. If a field of 1000 Gauss in a typical emission line star, e.g. γ^2 Velorum (see Fig. 1.1), would be present we

could observe features in circular polarization of only 0.3 percent of the line intensity at best (see eq. 3.8). Linearly polarized light is an indicator of scattering processes as well as magnetic fields.

The detection of magnetic fields is done through the observation of the Zeeman effect in spectral lines. The energy levels of an atom in an external magnetic field are split into $2J + 1$ sublevels. The energy difference of these sublevels is $\Delta E = gehB/4\pi mc$, were g is the Landé factor. As a result, the atomic lines are also split and we call the components for which $\Delta M = \pm 1$ (quantum number M for angular momentum) the σ components and for $\Delta M = 0$ we call them the π components. These components are polarized: For a transverse field, the π components are linearly polarized parallel to the field and σ components are polarized perpendicular to it. For a longitudinal field the σ components have opposite circular polarizations, whereas the π components are not visible.

In his paper Landstreet (1979) discussed several techniques of field measurements: *photographic Zeeman polarimetry, spectroscopy of stars with resolved Zeeman structure, photoelectric spectropolarimetry of metallic lines, Balmer-line Zeeman analyzer* and the *transverse Zeeman effect*. In addition, Landstreet also discusses the limitations of various methods of measuring longitudinal fields. An interesting effect arises when there is a patchy distribution of material. In that case, elements appear to be nonuniformly distributed on the stellar surface and the measured effective field is different for different elements.

The geometries of magnetic fields can be very complex. Models are calculated for a centered dipole, a decentered one, a symmetric rotator, or a more complex one. A list of well determined geometries in several stars is given in Landstreet (1979).

In the last few years the technique of Doppler imaging (the estimation of surface structures of an unresolved star using the Doppler effect) has made large

advances. It is also possible to derive surface information about the distribution of magnetic fields with the technique of Zeeman Doppler imaging. This can be done with circularly polarized light. A description of this technique, the basic principles, numerical simulations and technical considerations are given in three publications by Semel (1989), Donati et al. (1989) and Semel et al. (1993).

The basic principles of the analysis of polarimetric measurements are given in the first paper by Semel (1989). If we assume a stellar disk, affected by two magnetc spots of opposite polarities, with no relative velocity to the observer, the sum of their circular polarizations would be reduced or cancelled out. In the case of non-zero stellar rotation, the relative velocities of the spots are separated due to the effect of circular polarization. Then,

- the measured global magnetic flux is reduced and differential measurements may lead to the determination of the line-of-sight component of the magnetic field, and

- to increase the S/N of Stokes V, one may add the signals from several lines, to increase the quality of magnetic field measurements.

From the technical point of view, the application of Zeeman Doppler imaging has some important requirements. (A) Because of polarization levels of the order of 0.1 percent, the S/N ratio must be very high. (B) To see small scale structures the spectral resolution should be reasonably high. (C) Spurious polarization levels should be reduced to the level of the photon noise.

Some previous polarimetric results

(A) O stars – No magnetic field for any O star has been detected, so far. Even ζ Puppis, the brightest and most observed O star, failed to show clearly

intrinsically generated circular polarization. Although some spectral features in circularly polarized light were detected, insufficient data quality did not lead to quantitative results.

In order to search for a magnetic field, Barker et al. (1981) tried to measure the longitudinal Zeeman effect in the wings of Hβ of ζ Puppis, with a photoelectric Pockels cell polarimeter. Their values of the measured mean longitudinal field are given in Table 0.1.

JD 2,444,300+	B_e (Gauss)	σ (Gauss)
27.83	-110	138
48.62	-71	113
50.58	+48	65

TABLE 0.1. Surface brightness weighted average of longitudinal field strengths and standard deviation (Barker et al., 1981).

From these results alone, one cannot conclude that a magnetic field is really present. Nevertheless, Barker et al. argue that there *may* be much higher field values, which were possibly not detectable because of an unfavorable combination of field geometry and stellar orientation. If a $v \sin i$ of 210km/s given in earlier publications is correct, ζ Puppis must be seen almost equator-on. For this orientation, possible field geometries are given in Fig. 0.7.

Using the expressions derived by Schwarzschild (1950) the centered dipole field with the dipole axis parallel to the rotation axis (**case A**) yields zero longitudinal field ($B_e = 0$), independent of the field strength B_p at the pole. With an inclination $i = 70°$ it is possible to have $B_p \approx 1kG$ with $B_e \leq 100$ G. **Case B** is an extreme case of an oblique rotator (common among the known magnetic stars): a centered dipole with axis in the rotational equatorial plane. B_e will vary
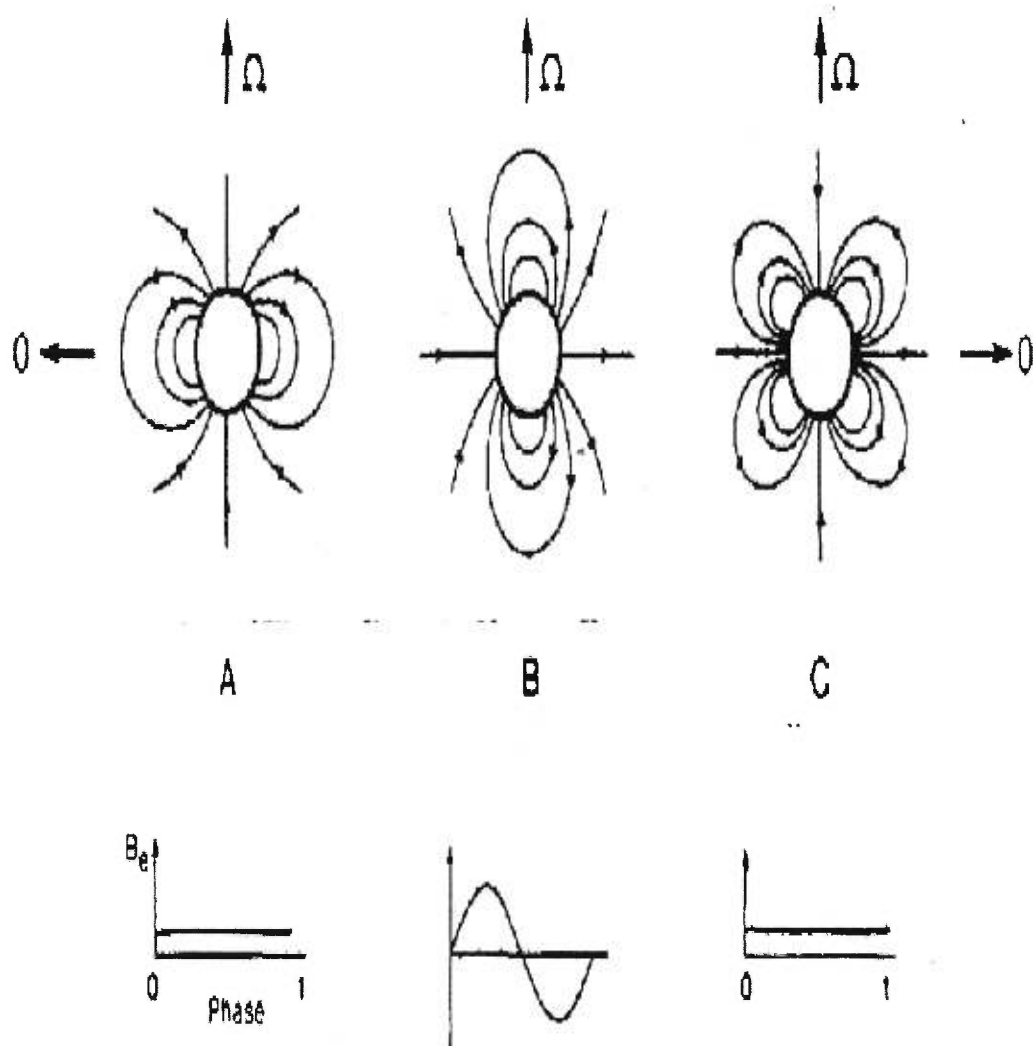
Figure 0.7. Three possible magnetic field geometries for a rotating star with a magnetic field, measured during a rotation period by an observer whose line-of-sight lies near the equatorial plane 00. (A) Centered dipole with rotation and magnetic axes parallel. (B) Centered dipole with rotation and magnetic axes orthogonal. (C) Linear quadrupole with an axisymmetric purely radial field in the equatorial plane (Barker et al., 1981).

sinusoidally and an observed $B_e \leq 100$ G implies a $B_p \leq 300$ G. Barker et al. could not exclude this possibility for ζ Pup because of incomplete phase coverage. A quadrupole geometry with an alignment of the field axis with the rotation axis (**case C**) with a $B_e \leq 100$ G implies a $B_p \leq 2$–4 kG. But no stars with predominantly quadrupole fields are known among the chemically peculiar stars, and so they conclude that it is not clear how plausible a pure quadrupole model of ζ Pup might be.

Linear spectropolarimetry at high signal-to-noise ratio for the Hα line of ζ Pup was presented by Harries & Howarth (1996). Their polarization measurements are given in Table 0.2, which lists the measured polarization in three bins; one 4-Å bin at the line centre ($\lambda 6563$ Å), one in the maximum of the line emission at $\lambda 6568$ Å, and one over a line-free continuum region at $\lambda 6760$ - 6860 Å.

Date	Line centre		Emission		Continuum	
Mar.	$\bar{q}$	$\bar{u}$	$\bar{q}$	$\bar{u}$	$\bar{q}$	$\bar{u}$
1992	(%)	(%)	(%)	(%)	(%)	(%)
15th	0.090	0.081	0.033	0.007	0.041	0.018
16th	0.096	0.093	0.035	0.007	0.042	0.024
17th	0.056	0.068	0.018	0.009	0.021	0.023

TABLE 0.2. Polarization measurements from 3 observations. The statistical errors on the line centre and maximum emission measurements are 0.008% while the error in the continuum is 0.002% (Harries & Howarth, 1996).

Recent ultra-high signal-to-noise spectroscopic measurements of the He II $\lambda 4686$ line of ζ Pup by Eversberg, Lépine & Moffat (1998, see also Chapter 1) show outmoving micro-structures in the strong O star wind. Assuming that these structures are generated by "blobs" one clearly can expect to detect linear depolarization features.

(B) WR stars -- The high degree of ionization in WR star winds coupled with a clear stratification (Schulte-Ladbeck et al. 1995), yield a large number of free electrons, which can scatter stellar light and polarize it. *Broadband* polarimetry has led to a large amount of information about WR stars. Here a group of eight papers, *"Polarization Variability among Wolf-Rayet Stars. I. - VIII."* by St.-Louis et al. (1987), Drissen et al. (1987), St.-Louis et al. (1988), Robert et al. (1989a), Robert et al. (1989b), Robert et al. (1990), Drissen et al. (1992), and Moffat & Piirola (1993) is noted.

Briefly summarized:

I. Results are considered for a complete sample of southern WC stars brighter than 9th magnitude. Binary modulation was found in polarization; less stochastic variability with faster winds; and it was suggested that "blobs" can be more easily detected in low velocity, turbulent winds.

II. This anticorrelation between stochastic polarization variability and wind velocity was confirmed by the study of the six brightest southern WN stars. No binary modulation was found in the known, long-period WN7 + O binary HD 92740, as in the suspected WN8 + c (c = compact companion) binaries HD 86161 and HD 96548.

III. A new way to derive mass-loss rates of WR stars in binaries was proposed. The estimation of the inclination of the system via polarization measurements led to a correlation between $\dot{M}$ and the mass of the WR star.

IV. Circular polarization in the continuum emission of WR stars above an instrumental level of $\sigma_V \sim 0.01\%$ was not detected.

V. Confirming the anticorrelation between stochastic polarization variability and wind velocity for seven of the eight bright Cygnus WR stars, they also developed two models to explain the origin of blobs.

VI. The orbital inclination of the WR + O binary V444 Cygni was determined to be $i = 78°.5$, in agreement with other methods. Also, they confirmed the hypothesis of Chandrasekhar that strong polarization variations should be visible during the eclipse of the WR star by the O companion. The WR radius was found to be $\leq 4R_\odot$. Note: An improved analytical model for the eclipsing WR + O binary V444 Cygni was presented later (St.Louis et al., 1993).

VII. Monitoring the three single WR stars WR14 (WC6), WR25 (WN7), and WR69 (WC9), they found no significant variation in WR14, but for the other two $\sigma \sim 0.06\%$, as expected for late-type WR stars.

VIII. Finally, observations of the two non-eclipsing WC + O binaries HD 97152 and HD 152270 show variation in the continuum but none in the strong emission-line complex of C III /C IV + He II . They deduce that mainly light from the O companion scatters off electrons in a spherically symmetric wind and introduces modulated orbital polarization.

St.-Louis et al. (1995) observed EZ CMa with the IUE satellite in their IUE MEGA Campaign during 16 consecutive days. The observed variations suggest a global wind structure pattern that remains stable during several rotation cycles in the frame of the star. It can best be explained by some kind of corotating interaction regions emanating from hot (magnetically?) active regions near the surface of the stellar core.

The first spectropolarimetric observation of a Wolf-Rayet star was made by McLean et al. (1979b) for EZ CMa (WN5) with the same instrument as for their observations of Be stars (McLean et al., 1979a) here in the range 3400 Å – 6000 Å with 48 Å resolution (for the He II λ 4686 Å line they obtained 32 Å resolution). That EZ CMa shows strong variability is a well known fact (e.g., Robert et al., 1992). Serkowski (1970) found a deviation from spherical symmetry from broadband polarization observations. The model of Cassinelli & Haisch (1974) then

explained the observed polarization with a disk-like structure. A non-spherical atmosphere was established by McLean et al. due to varying degrees of linear polarization in He I , He II , NIII, NIV and NV lines, and from their data an edge-on view can be excluded. Their data suggest a density enhanced disk-like structure in the atmosphere (see Schulte-Ladbeck et al., 1992c).

In the first two of a number of spectropolarimetry papers, Schulte-Ladbeck et al. (1990 and 1991) published the discovery of linear polarization variations in the He II wings of EZ CMa obtained at Pine Bluff Observatory in Wisconsin. Also for the first time, they detected polarization loops in the Q-U plane, like those seen in Be stars. This leads to the assumption that also in this WR star an axisymmetric, electron scattering envelope could be the reason for this behavior. From their data they suggest a rotating and expanding disk-like density distribution around EZ CMa.

In their second paper, Schulte-Ladbeck et al. (1991) probe the wind structure of EZ CMa through electron distribution as measured by spectropolarimetry. They conclude that

1. the wind of EZ CMA is not spherically symmetric, because of a large amount of continuum polarization,

2. the polarization is due to electron scattering, since the continuum polarization spectrum is flat at most epochs,

3. the spectrum of continuum polarization may rise into the UV, which is due to frequency-dependent absorptive opacity in the helium continuum,

4. the continuum polarization has a large, quasi-static component which can be explained with an inclined-disk model. The disk extends rather far into the wind, because it is seen also in line-forming regions,

5. the preferred explanation for polarization variations is from density fluctuations in the wind,

6. line photons are electron scattered, since emission lines are polarized, although not as strong as continuum light,

7. ionization stratification is seen in this star.

Recent results clearly show that the intrinsic variations are not caused by a companion. EZ CMa seems to be a single star.

The impression that the continuum polarization rises into the UV was confirmed by the first linear polarization spectrum of EZ CMa and Θ Mus (WC6 + O9.5I) obtained in the region 1400 to 3200 Å by the Wisconsin Ultraviolet Photo-Polarimeter Experiment (WUPPE) (Schulte-Ladbeck et al., 1992b). The continuum polarization, measured in several bands from around 1600 Å to 3100 Å, reached about 0.8%, which confirmed the picture of a distorted wind in EZ CMa. Although Θ Mus shows variability in polarized light of about 0.2% around a mean of 1.45% at 82° (St.-Louis et al., 1987), Schulte-Ladbeck et al. were able to fit their UV data with a Serkowski law for the interstellar polarization. The position angle did not change from one emission line feature to another. They conclude that the intrinsic polarization of the Θ Mus system is not easily distinguished from interstellar polarization.

Observations in visible light for HD 191765 (WN6) showed similar results as for EZ CMa (Schulte-Ladbeck et al., 1992a); strong wavelength-dependent continuum polarization, reduced polarization levels across emission lines, a general deviation from spherical symmetry, localized density changes, axisymmetric wind geometry and ionization stratification.

One of the most recent works about spectropolarimetry is the Ph.D. thesis of Harries (1995). Among others, he investigated 16 WR stars (mainly WN types

but also 3 WC stars, single and binary) with state-of-the-art techniques and telescopes. Among these stars he found "line effects", polarization variability across their lines, in 4 single WN stars, 1 binary, and all 3 WC stars. For a few single stars, he supports the claim of non-spherical wind structure, either in an oblate form, axisymmetric ellipsoid or disk.

Specific considerations

The present work is an attempt to give answers to some basic questions highlighted above.

Chapter 1 discusses an important part of a possible evolutionary link between O and WR stars. We show that at least in one O star clumping in the wind is present which supports the idea that O stars are the progenitors of WR stars. In an attempt to answer these questions we obtained two nights at the Canada-France-Hawaii Telescope for observation of the apparently brightest (according to its visual magnitude m_V), early-type O star in the sky, ζ Puppis. The brightness ($\sim$ 2nd mag) and the size of the telescope enabled us to obtain a number of ultra-high resolution spectra with high signal-to-noise on very short time-scales. In this chapter the first detection of a clumpy wind in an O star is presented. It is shown that the stochastically outmoving structures in the He II λ 4686 Å line of ζ Puppis behave similarly to those in WR star winds and that their outmoving acceleration is somewhat lower than previously predicted. Especially the fact that these clumps appear at very small radii supports the assumption that previously predicted mass-loss rates are probably significantly overestimated. As a consequence, stochastic clumping in He II means that also stochastic variability of linear polarization in this line should be present. Hence, our observation gives an additional indicator that spectropolarimetric measurments should be succesful for O star atmospheres.

Chapter 2 introduces a new polarimetric unit for obtaining spectropolarimetric information about extended stellar atmospheres. So far, a number of spectropolarimeter units exist. Either a half-wave plate or a quarter-wave plate is normally used as retarder to measure linear *or* circular polarization, respectively. However, it is of great interest to obtain quasi-simultaneous observations of linearly *and* circularly polarized light. This is possible by combining two rotatable quarter-wave plates as retarders with a Wollaston prism as the polarizer.

By using different fixed position angles of the quarter-wave plates with respect to the prism, it is possible to obtain all four Stokes parameters I, Q, U and V in a quasi-simultaneous manner. The main goal should be a reliable instrument, as simple as possible, compact and easy to carry, which would enable the observer to use various telescopes at different observing sites. One can take advantage of the regular presence of standard CCD-spectrographs at modern telescopes by carrying only the polarimeter unit, mounting it at the Cassegrain focus, and feeding the spectrograph by optical fibers. This has the advantage of being able to use even Coudé spectrographs with high resolution capability, although the polarimeter is connected to the Cassegrain focus to minimize linear instrumental polarization. For this reason A. Moffat, M. Debruyne, J. Rice, N. Piskunov, P. Bastien, W. Wehlau, O. Chesneau and the author of this thesis (see author's list of the respective publication in this chapter), developed a new polarimeter unit, the William-Wehlau spectropolarimeter, with two quarter-wave plates in tandem, which fullfills all the above considerations: It is light ($\sim$ 40kg), compact (length $\sim$ 1m) and feeds various spectrographs with long ($\sim$ 40m) optical fibers. The instrument is shown in Fig. 0.8. During a number of extended engineering and observation runs at Elginfield Observatory, University of Toronto Southern Observatory and Mont Mégantic Observatory, we encountered various technical problems and developed techniques to solve them.

Chapter 3 discusses spectropolarimetric results for the most prominent WR+O binary system γ^2 Velorum. The feasibility of a first scientific observation campaign with a new spectropolarimeter depends on various conditions:

1. A small or mid-size telescope: $-$ It is clear that a new spectropolarimeter must pass a number of tests, before applying for time at larger telescopes. Even with our tests at Elginfield Observatory we had little hope to accumulate observing time at large instruments, because of relatively bad weather conditions and limited infrastructure at this site.

2. Reasonable targets: – There are a number of stellar objects which are suitable canditates for detecting intrinsic linear and/or circular polarization, namely O, B, Be, Ap/Bp stars, Wolf-Rayet stars, but also late-type stars with extended atmospheres. Because of our focus on stars in the upper left part of the HR diagram, we decided to choose a number of O and WR stars.

3. Intermediate or long time coverage: – Even with a telescope of intermediate size, e.g, 2m class, the exposure time for bright stars is of the order of hours to reach 0.01% accuracies as likely necessary to detect intrinsic polarization in hot stars. To circumvent this problem, one has to repeat the observation of the target for many times.

4. Bright stars: – Using a small telescope (see 1.) with the necessity to detect very small spectral variations (see 3.) requires bright objects.

Combining these restrictions, we decided to observe bright prototype O and WR stars with the William-Wehlau spectropolarimeter at the 0.6m University of Toronto Southern Observatory on Cerro Las Campanas in Chile. We finally chose the apparently brightest (according to its visual magnitude m_V) WR star γ^2 Velorum and again the apparently brightest (according to its visual magnitude m_V) early-type O star, ζ Puppis. For ζ Puppis as the secondary target in our program we did not obtain sufficient data for a reasonable analysis.
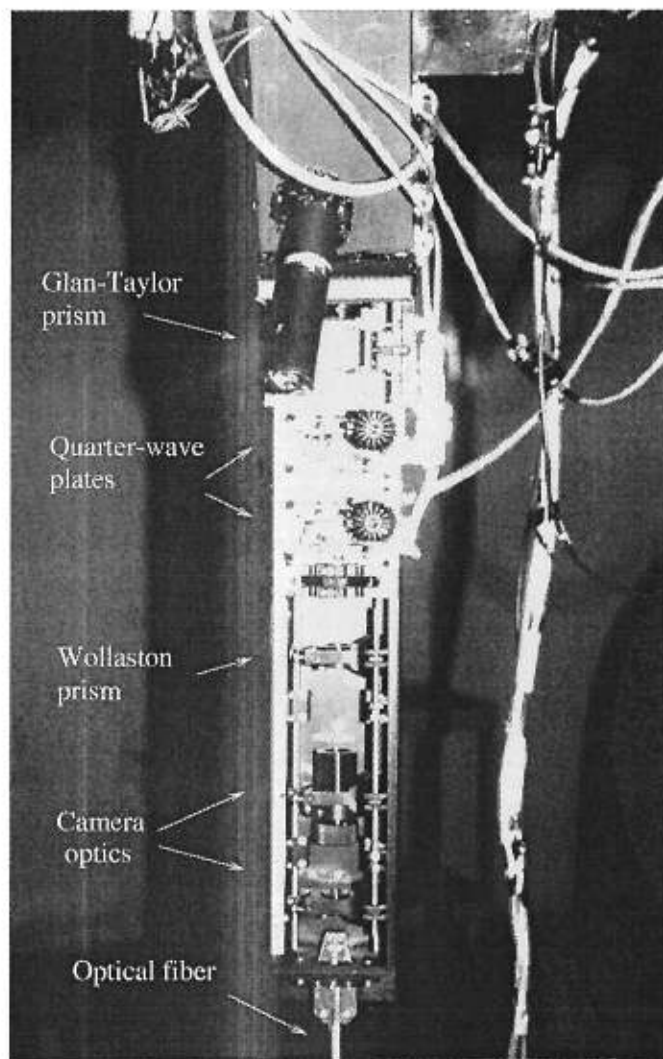
Figure 0.8. The optical channel of the William-Wehlau spectropolarimeter.

Chapter 1

Outmoving Clumps in the Wind of the Hot O-Supergiant ζ Puppis

THOMAS EVERSBERG[1], SÉBASTIEN LÉPINE[1] AND ANTHONY F.J. MOFFAT[1]

Département de Physique, Université de Montréal, C.P.6128, Succ. Centre Ville, Montréal H3C 3J7, Canada, and Observatoire du Mont Mégantic

1.1 Abstract

We present time-series of ultra-high S/N, high resolution spectra of the He II $\lambda\,4686\,\text{Å}$ emission line in the O4I(n)f supergiant ζ Puppis, the brightest early-type O-star in the sky. These reveal stochastic, variable substructures in the line, which tend to move away from the line-center with time. Similar scaled-up features are well established in the strong winds of Wolf-Rayet stars (the presumed descendants of O stars), where they are explained by outward moving inhomogeneities (e.g., blobs, clumps, shocks) in the winds. If all hot-star winds

---

[1]Visiting Astronomer, Canada-France-Hawaii Telescope, operated by the National Research Council of Canada, the Centre National de la Recherche Scientifique de France, and the University of Hawaii

are clumped like that of ζ Pup, as is plausible, then mass-loss rates based on recombination-line intensities will have to be revised downwards. Using a standard 'β' velocity law we deduce a value of $\beta = 1.0$–1.2 to account for the kinematics of these structures in the wind of ζ Pup. In addition to the small-scale stochastic variations we also find a slow systematic variation of the mean central absorption reversal.

1.2   Introduction

The most massive stable stars known have O-type spectra. Among the O stars, the hotter ones tend to have the highest masses. Coupled with this high mass is a high luminosity (and high surface temperature), which drives a strong wind and leads to various kinds of instability and variability (e.g. blue-to-red moving substructures in photospheric absorption lines associated with surface non-radial pulsations: NRP (e.g. Baade 1988); red-to-blue propagating dark absorption components DAC (e.g. Prinja & Howarth 1986) in the absorption edges of strong P Cygni lines, probably associated with corotating interacting regions: CIR – e.g. Cranmer & Owocki 1996). Conversely, study of the variability can provide useful constraints on the nature of massive stars and their strong winds.

Although O stars are very rare compared to lower-mass stars, their extremely bright intrinsic luminosity makes them appear significant in number among the apparently brightest stars in the sky. The brightest *early-type* O star in the sky is the second visual magnitude O4I(n)f star ζ Puppis. Its variability has thus been scrutinized considerably in the past. As it turns out, ζ Pup manifests a high degree of variability compared to other bright single O stars, probably because of its large $v\sin(i)$ for a supergiant of 220 km/s (Prinja 1988, Kaper et al. 1996). This high rotation velocity may be related to its runaway status (Blaauw 1993). In Table 1.1 we summarize some major properties of ζ Puppis (see also Reid & Howarth 1996).

TABLE 1.1. Observed properties of ζ Pup

Property	Value	Ref.
Spectral Type	O4I(n)f	1
V (mag)	2.26	2
T_{eff}(kK)	42.0	3,4,5
$R_\star/R_\odot$	$18.4^{+5.2}_{-3.3}$	4
$M_\star/M_\odot$	52.5	5
$\log \dot{M}(M_\odot/yr)$	-5.57 $\pm$ 0.15	6
v_∞ (km/s)	2250	5
$v \sin(i)$ (km/s)	220	5
d (pc)	429^{+120}_{-77}	6,7

(1) Walborn (1972); (2) Johnson (1965); (3) Bohannan et al. (1986); (4) Kudritzki, Simon & Hamann (1983); (5) Puls et al. (1996); (6) Schaerer, Schmutz & Grenon (1997); (7) van der Hucht et al. (1997)

In particular, ζ Pup shows three distinct timescales in its variability:

1. $P_1 = 5.1 \pm 0.1$ d, seen in Hα (e.g. Moffat & Michaud 1981; Ebbets 1982), UV P Cygni lines (e.g. Prinja 1992; Howarth, Prinja & Massa 1995), and X-rays (Berghöfer et al. 1996a). This is likely the rotation period, with $\sin i$ close to unity (Reid & Howarth 1996)

2. $P_2 = 15$ - 19 h, seen in Hα and UV wind lines (Prinja 1992; Howart et al. 1995; Reid & Howarth 1996). This is the recurrence time scale of DACs; it is not strictly periodic. Even the 16.7 ± 0.8 h periodicity found (simultaneously with Hα) in moderately high energy X-rays by Berghöfer et al. (1996a), probably falls in this category.

3. $P_3 = 8.54 \pm 0.05$ h found in blue-to-red moving bumps on photospheric absorption lines (Baade 1986, 1988; Reid & Howarth 1996). This period is

probably the result of NRP in the stellar surface, with $l = -m = 2$. Higher modes ($-m = 4, 8$) have been seen only on one occasion (Baade 1991). Whether P_3 is fundamentally related to P_2, e.g., a harmonic with $P_3 = \bar{P}_2/2$, remains to be settled. Also, with the data available presently, it is still not established whether $\bar{P}_2$ is a simple fraction (e.g., $\frac{1}{6}$) or not, of P_1, the rotation period, as expected for fixed perturbations on the rotating stellar surface. A possible connection between rapid rotation and DAC activity arises in the spectropolarimetric evidence for an aspherical wind in ζ Pup (Harries & Howarth 1996).

Another type of variability in hot stars - stochastic - has only been clearly seen directly so far in stars with very strong winds. The intense winds of Wolf-Rayet (WR) stars (the descendants of O stars) exhibit small-scale variations in their (more easily observed) optical emission lines (Robert 1992; Moffat & Robert 1992). These are believed to arise in density perturbations (clumps) throughout the WR wind, as a result of supersonic compressible turbulence (Henriksen 1994), driven by radiative instabilities (Owocki 1994; but see Chiueh 1997 for an alternative explanation). Indirect evidence for clumpy structure in O-star winds has been proposed e.g. via X-ray observations (Chlebowski, Harnder & Sciortino 1989; Hillier et al. 1993), although no stochastic X-ray variation has been clearly seen yet (Berghöfer, Schmitt & Cassinelli 1996b). Hillier et al. (1993) modeled the 0.1–2.5 keV spectrum of ζ Pup under the assumption that turbulence and associated shocks in the wind are the origin of the observed X-ray flux. Their results are supported by more recent calculations of Feldmeier et al. (1997).

A key question here concerning the heretofore lack of direct detection of such perturbations in O-star winds, is whether such perturbations simply do not arise in O-star winds, or whether the observed wind lines in O stars are so weak that their detection has been difficult. ζ Pup is an obvious first target for this purpose, since it has a relatively strong wind for an O star, and it is very bright,

allowing one to obtain very high quality spectra in a short time. In this paper, we attempt to answer this question.

1.3 Observations and Data Reduction

ζ Pup was observed at the f/8.2 Coudé focus of the 3.6m Canada-France-Hawaii Telescope for ~ 5 hours during each of the nights of 1995 December 10/11 and 12/13. Using the red Coudé train and image slicer, the 1800 l/mm holographic grating and the Reticon 1872 array as a detector (see the CFHT User's Manual and references therein), we obtained a S/N $\approx 1000/0.03$ Å pixel in 10 minutes on a total range of 60 Å centered on He II λ 4686 Å. Along with Hα, this is the strongest wind line in the optical spectrum of ζ Pup. However, He II has the advantage of forming close to the star *and* being much less affected by variable telluric features. The Reticon uses four amplifiers, one for every fourth pixel. Their different sensitivity cancels out through flat-fielding. The data reduction was carried out using IRAF with a Reticon reduction package developed by D. Bohlender and G. Hill, which includes the baseline reduction, flatfielding, heliocentric correction and wavelength calibration with a Thorium-Argon comparison spectrum. The FWHM of the Th-Ar lines covers ~ 2 pixels and the wavelength shift over each night was negligibly small. The 60 Å window is too small to cover the whole He II emission line and its blue wing is affected by the N III emission line complex. To obtain a reasonable and reproduceable quasi-continuum we have fitted a straight line through two ranges of 1 Å (≈ 30 pixels) in the extreme blue/red wings for each spectrum at the same position. This was divided into each spectrum to compute quasi rectified emission profiles.

1.4 Results and Discussion

1.4.1 Small-Scale Variations

As a first step, we have co-added all spectra to yield a mean for each night. This was then subtracted from the individual spectra. The resulting plots are shown in Fig. 1.1. The respective greyscale plots and the nightly means are shown in Fig. 1.2 and Fig. 1.3.

A first look at the greyscale plots in Fig. 1.2 and 1.3 shows that individual residual emission features move away from line-center to the blue/red wing of the line. All features tend to smear-out with time, while the intensity first rises, then drops. In order to explore the global variability we first calculated the standard deviation of pixel i:

$$\sigma_i = \sqrt{\frac{1}{n-1}\sum_{j=1}^{n}(I_{ij} - \bar{I}_i)^2} \quad , \tag{1.1}$$

where I_{ij} is the rectified intensity of pixel i of the jth spectrum, $\bar{I}_i$ the mean rectified spectrum at pixel i. The results for both nights are shown in Fig. 1.4 and Fig. 1.5. Allowing for statistical fluctuations, the variation profile across the line, $\sigma(\lambda)$, follows the same basic shape of the line profile $I(\lambda)$ itself, with $\sigma(\lambda)/I(\lambda) \sim 5\%$ and a small systematic increase in $\sigma(\lambda)$ on the blue side of the line, where a small level of P Cygni absorption likely prevails. This implies that wind variations occur *throughout* the wind where He II λ 4686 is emitted. These short-term variations in emission-line profile appear to occur without any noticeable influence from the near-central absorption reversal.

To consider the line variability in more detail we traced the radial velocities of individual subpeaks with time (see Fig.1.1). This was often a delicate operation: The He II line has a peak intensity of only 1.2 × continuum (compared to several times the continua in WR lines) and the residuals are still relatively noisy. The form of single features can change very quickly from one spectrum to the next,
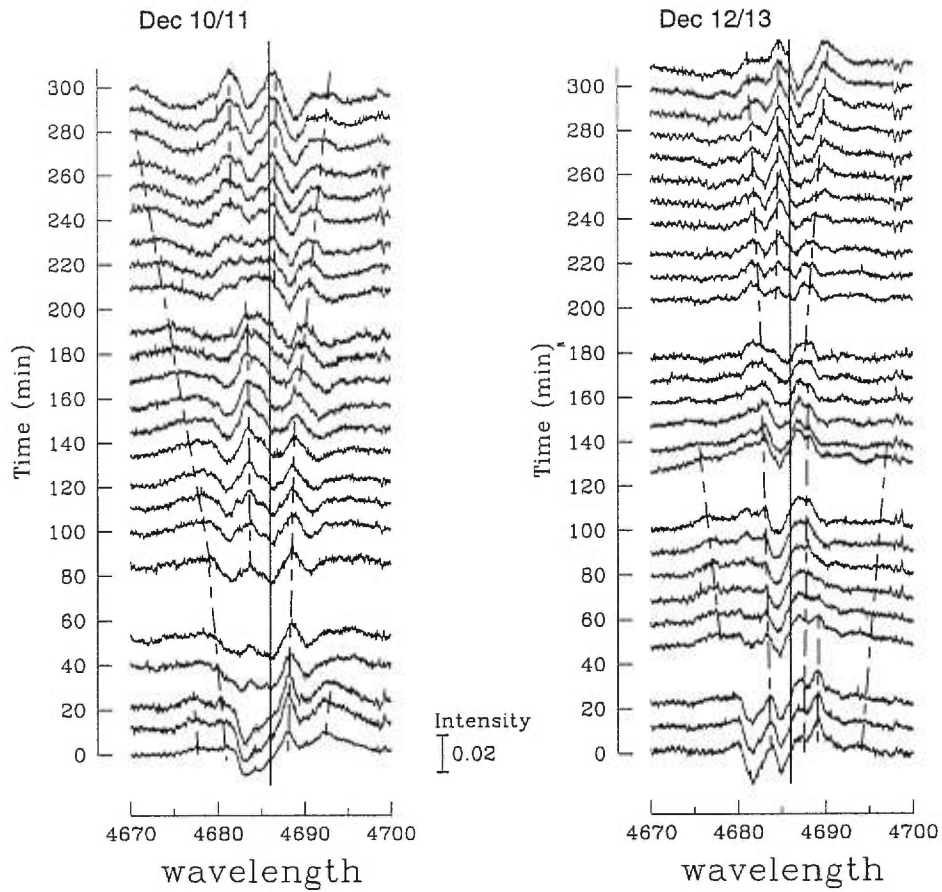
Figure 1.1. Residuals of He II λ 4686 for ζ Pup on 1995 Dec. 10/11 and Dec. 12/13. The vertical axis gives the intensity and the time, respectively. The scale for the residual intensities is indicated. Dashed lines trace detected variations during the night. Vertical solid lines indicate the rest wavelength.
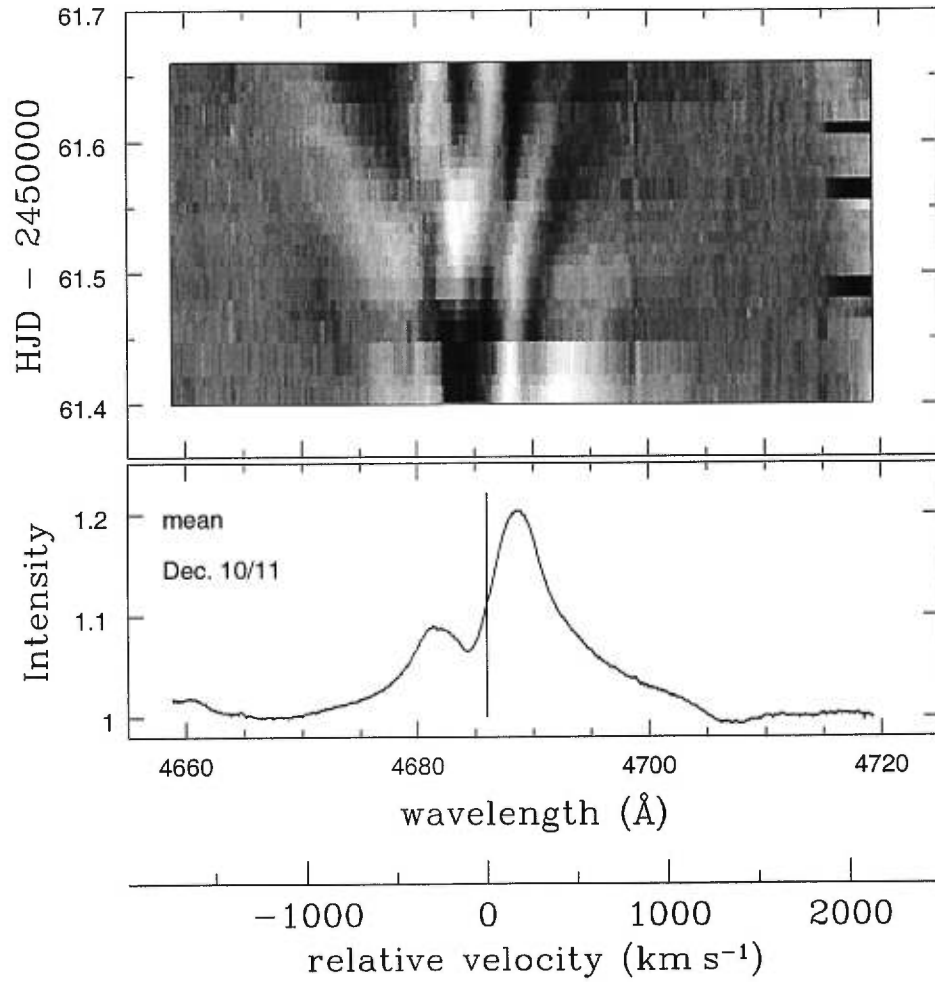
Figure 1.2. Observed He II λ 4686 spectra of ζ Pup for the night of 1995 Dec.10/11. TOP: Greyscale plot of nightly residuals from the mean rectified spectrum of each night plotted in time (stretched appropriately to fill in time gaps) vs. wavelength. BOTTOM: Mean spectrum. The vertical line corresponds to the rest-wavelength (4685.73 Å), not allowing for any peculiar motion of the star.
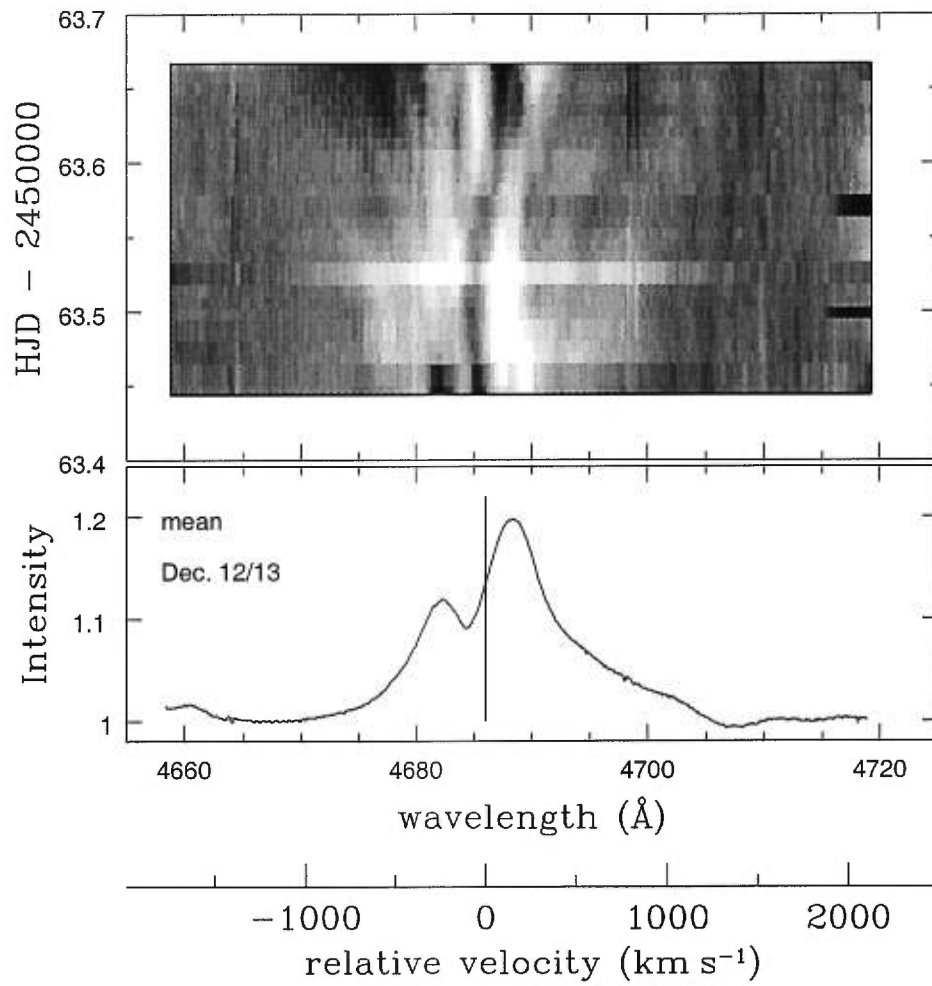
Figure 1.3. Same as in Fig. 2, but for 1995 Dec.12/13.
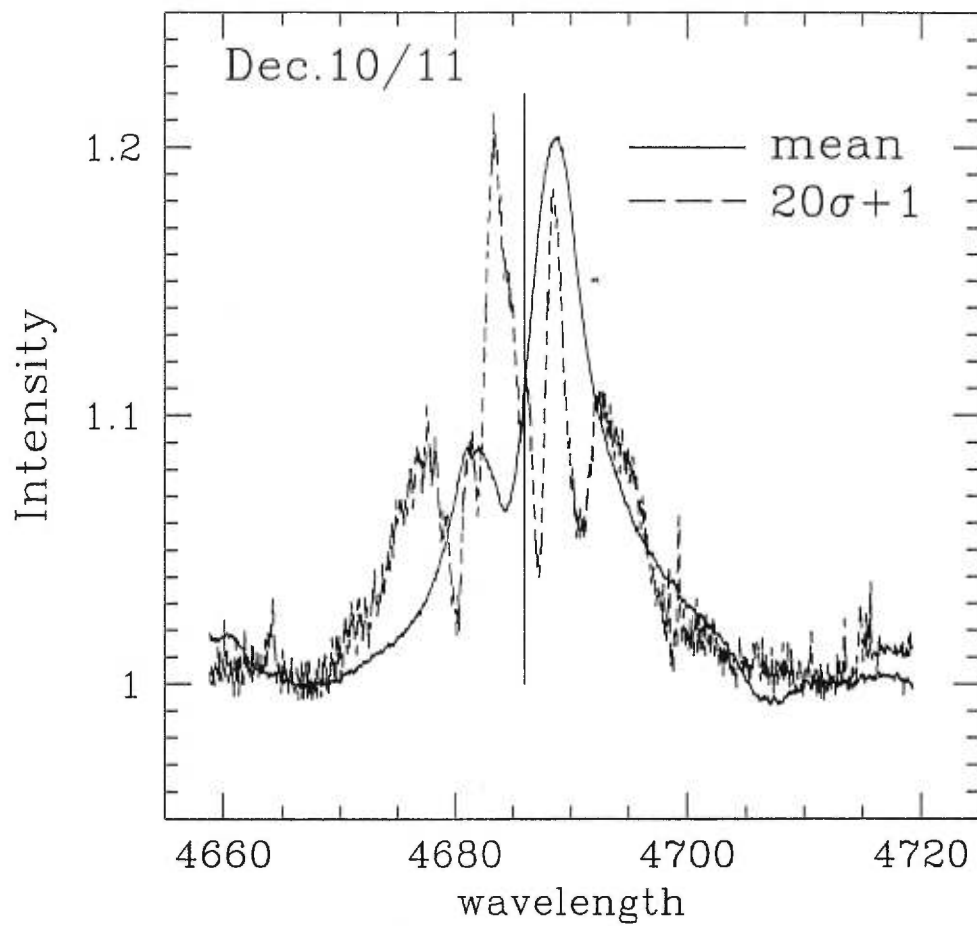
Figure 1.4. Mean rectified spectrum (solid) and standard deviation σ (dashed) for Dec. 10/11. The σ profile is expanded by a factor 20 and increased by 1.0 in intensity, to match the mean rectified line profile as closely as possible.
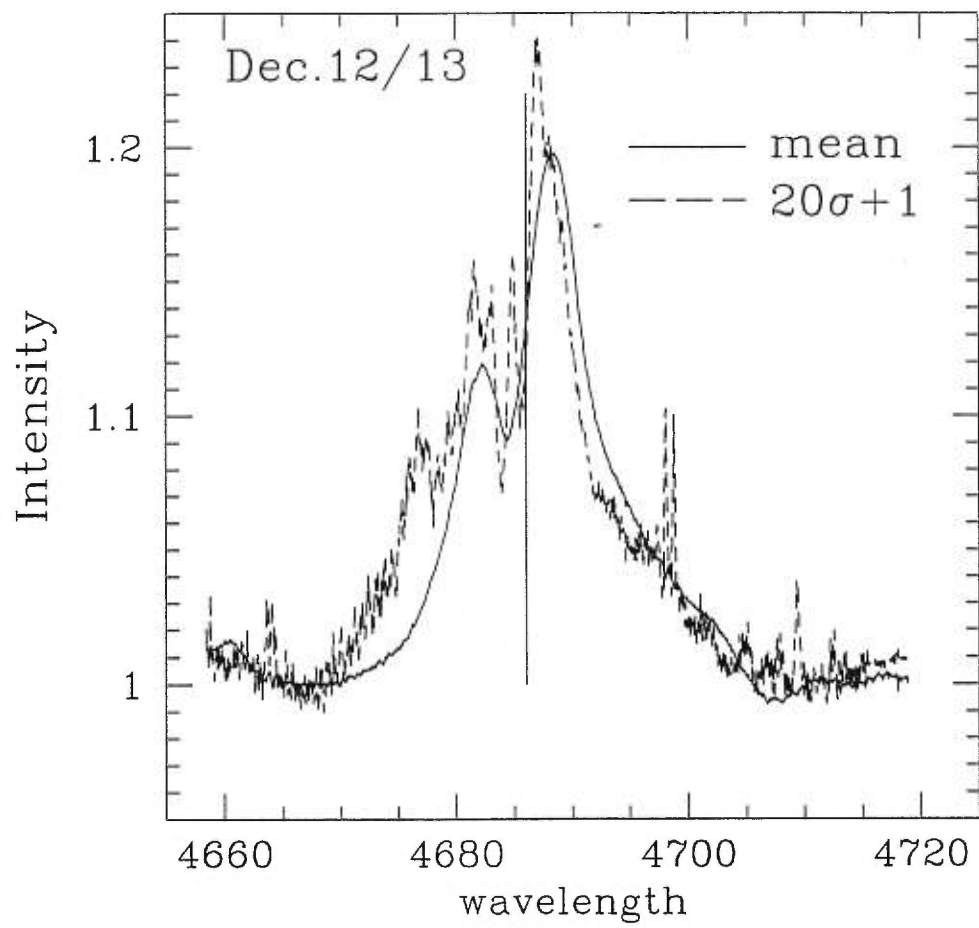
Figure 1.5. Same as Fig. 4, but for Dec 12/13.

e.g., from gaussian-like forms to double-peaked triangles. We therefore assume that the non-simple form of even the most obvious sub-features may be the result of blends of many unresolved features. After trying unsuccessfully to deblend the subpeaks with multi-gaussian fits and simple peak measurements, we decided to keep things as simple as possible by fitting single gaussians only to the most prominent features. On the other hand, this assumption for the sake of simplicity and consistency also means that we will be clearly limited in detecting a relatively small number of blobs.

Does a β velocity law fit the observed trajectories? We attempt to answer this by looking at the detailed motion of the clearest, most prominent, traced subpeak, visible on the near red side of the line center of He II $\lambda\,4686$ during the whole observing sequence of 1995 Dec 10/11 (see Fig.1.2). Fig. 1.6 shows a plot of observed velocity versus time for this feature, which actually consists of two distinct branches. Superimposed on these data are theoretical β-laws, obtained using $v(r) \equiv \frac{dr}{dt} = v_\infty(1 - \frac{R_*}{r})^\beta$ converted to v(t)[1] and then to projected velocity $V(t) \equiv v(t)\cos\theta$, for different values of β and θ (the assumed constant angle between blob trajectory and the line-of-sight). The first branch (open circles) can be matched by a β–law with $1 < \beta \lesssim 2$ (and $100° < \theta \lesssim 140°$, respectively), while the second branch (filled circles) requires $1 \lesssim \beta \ll 2$ ($112° \lesssim \theta \ll 180°$). If the clumps follow a unique β–law these two branches taken together suggest $1 < \beta < 2$. By comparison, Reid & Howarth (1996) obtained $\beta \approx 1$ using the same technique for variations with longer time coverage on the blue side of the Hα wind-line of ζ Pup.

All traced structures show nearly linear propagation with time. This may seem curious, considering the standard velocity-law with *nonlinear* behavior. However, the blobs have been traced over only a relatively small range in distance, so that linear motion is a good approximation. Then it is possible to characterize

---

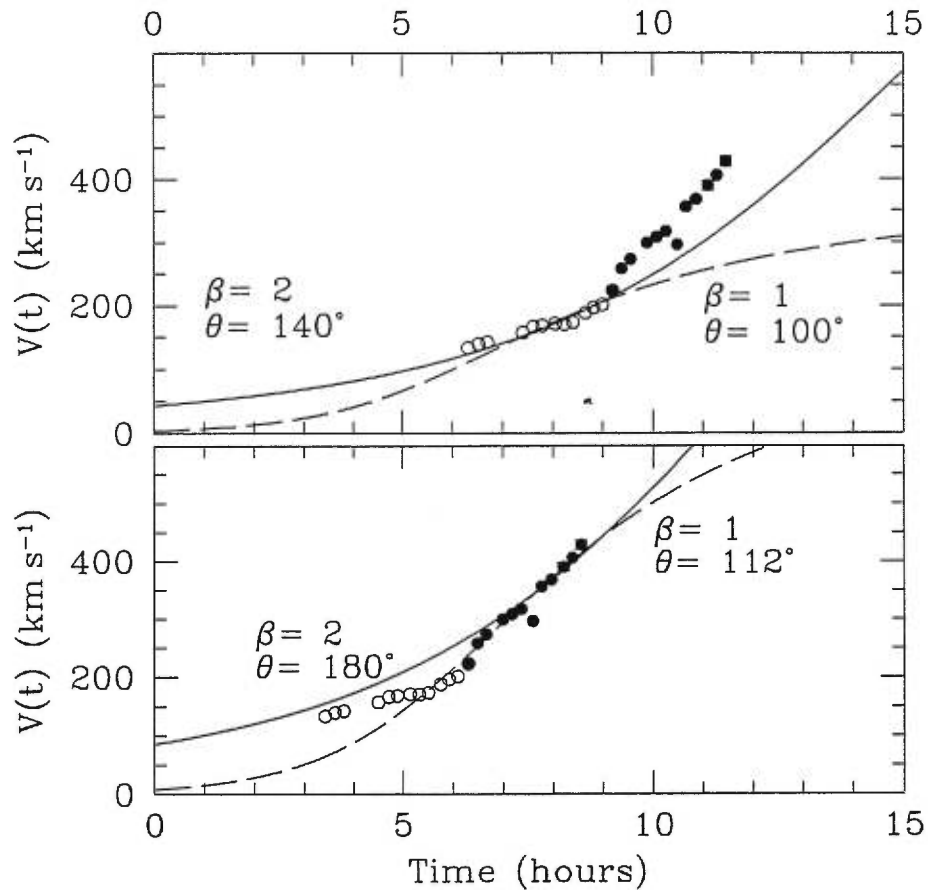[1]from $v_\infty t = \text{const.} + \int \frac{dr}{(1-\frac{R_*}{r})^\beta}$

Figure 1.6. Projected velocity versus time of the most clearly identified and traced subpeak in the wind of ζ Pup, on 1995 Dec 10/11 at $V(t) \sim 130 - 450$ km s^{-1} (see Fig. 2). This subpeak actually consists of two distinct clumps indicated by different symbols. The transition point from one clump to the other is somewhat subjective. Error-bars are indicated or are smaller than the data points. Sample lines represent the standard velocity law matched to each clump for pairs of β, θ. The origin on the time axis was arbitrarily chosen to occur when $v = 0.01v_\infty$ for the $\beta = 1$ curves.

the blob trajectories by a mean acceleration and velocity in the observer's frame, and to compare all observed blobs with the velocity law for fixed β but different θ (see also Moffat & Robert 1992). The results are shown in Fig. 1.7 and 1.8, where we explore which values of β and $R_\star$ allow one to fill in best the areas of permitted substructures, assuming they propagate like a single β-law wind. It would appear that the standard $\beta = 0.8$ law for O-star winds (Pauldrach, Puls & Kudritzki 1986) does not do this best at least for clumps, with a dearth of features for $\mid \dot{V} \mid \gtrsim 0.05$ km/s^2, where, if any features existed, they should be seen. On the other hand, a value of $\beta \approx 1.1$ does a better overall job. We claim that a value of β in the range $\approx 1.0 - 1.2$ best satisfies the data in Fig. 1.7 and Fig. 1.8. Such a range is also compatible with the detailed trajectories in Fig. 1.6. Figures 1.7 and 1.8 show also that most observed substructures are found at $R \lesssim 2R_\star$ (solid trajectories), with a preference at $R \lesssim 1.5R_\star$ for the most accelerated features.

Note that on the blue side accelerations are detected which reach higher values than on the red side. This could be due to small number statistics (we detected only 17 features). On the other hand, it could be that features in the red at large projection angles and close to the star are hidden by the star itself, so that we are seeing the manifestation of such a *shadow effect*.

Do the substructures in Fig. 1.7 and 1.8 appear randomly in time? With only 5 hours coverage each night, we are not justified looking for 8.5 hour or ~ 17 hour periods. On time scales below ~ 5 hours, however, Fig. 1.7 and 1.8 certainly do not show any obvious short periodicity, although more data will be required to check this to be absolutely sure.

Can the observed line-variations be temporally and spatially coherent, created by features of photospheric origin (NRP, CIR)? Emission lines reflect the physical behavior simultaneously in the *whole* wind, except for a cylinder behind the star. Any feature generated in the wind and rotating around the star
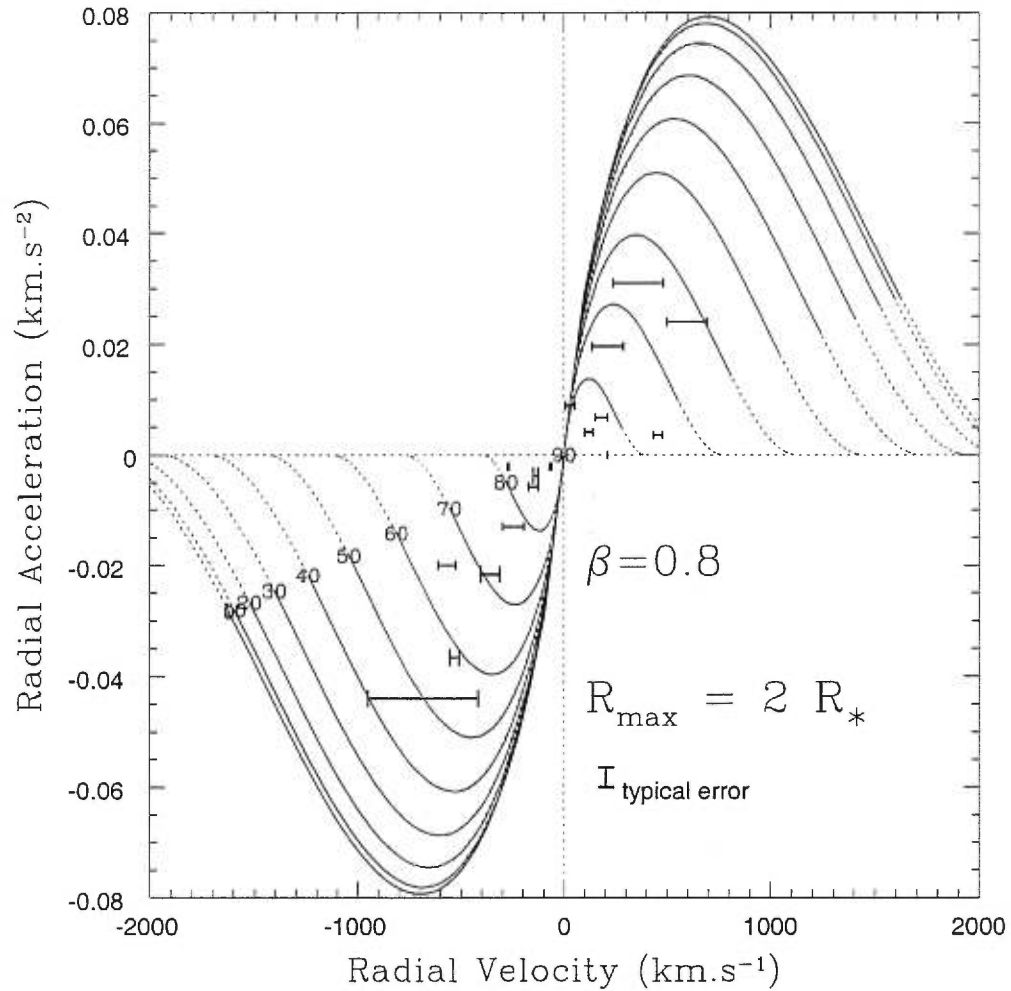
Figure 1.7. Plot of (projected) radial acceleration $\dot{V}$ versus radial velocity V for individual blobs in He II $\lambda\,4686$. Each curve represents a locus with respect to the line-of-sight from $\theta = 0°$ (lower curve) to $\theta = 180°$ (upper curve). Model loci are based on $V = v(r)\cos\theta$ and $v(r) = v_\infty(1 - R_\star/r)^\beta$ for $\beta = \mathbf{0.8}$ (the standard value for OB-star winds). Solid lines are extended by dotted lines which go beyond R_{max}. The adopted terminal velocity is $v_\infty = 2250\mathrm{km/s}$ and the adopted stellar radius is $R_\star = 18R_\odot$. Horizontal bars indicate the velocity range of an identified and traced substructure. The rms error (1 σ) for the acceleration is indicated.
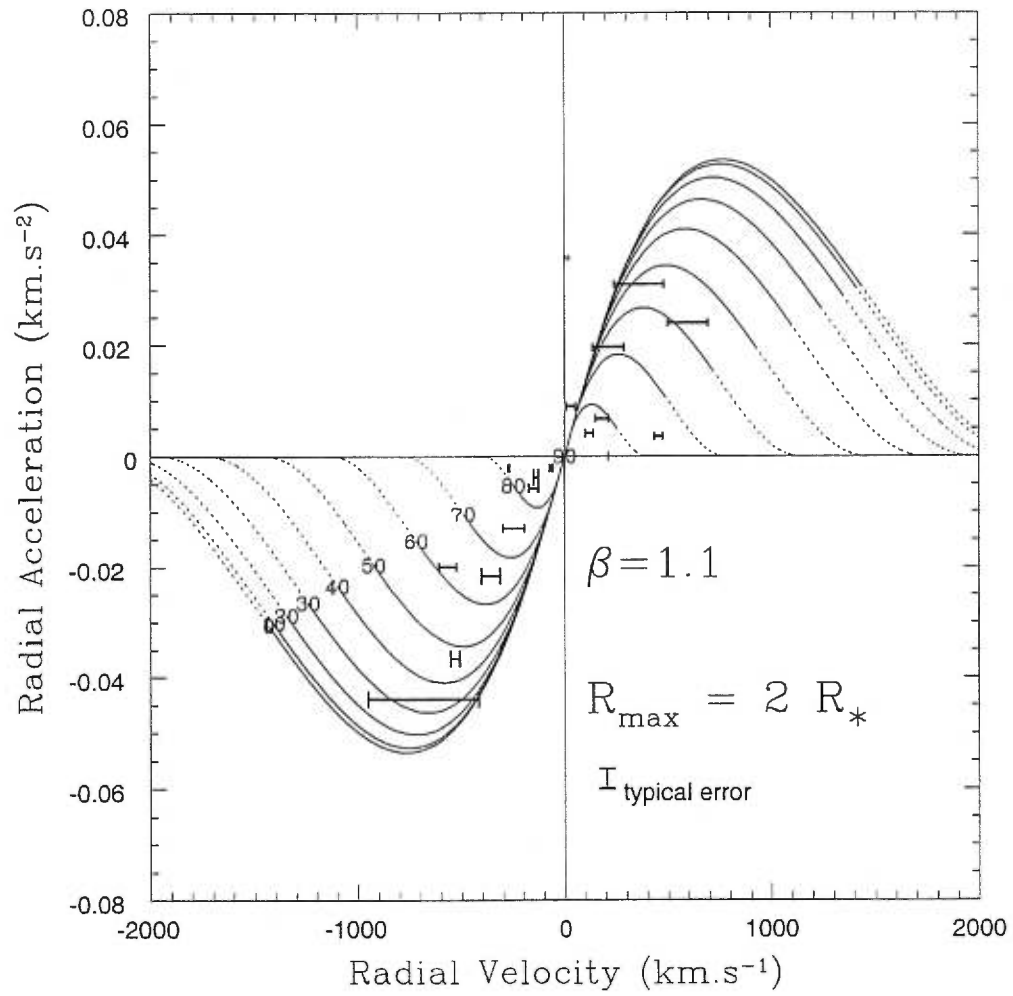
Figure 1.8. Same as Fig. 7, but for $\beta = \mathbf{1.1}$.

should produce wavelike variations in velocity space. Such features could move from blue to red, and sometimes *vice versa*, right across the line center. Because we observed features only moving *away* from the line-center in ζ Pup, we assert that the substructures likely represent the stochastic manifestation of turbulent clumps propagating outward with the wind, much the same as already seen in a significant number of WR star winds.

1.4.2 Large-Scale Variations

In Fig. 1.9 we superpose the mean profiles from each of the two nights. It is quite remarkable that the emission part of the *mean* profile shows very little change over the 2-day interval. This is likely a consequence of the stochastic nature of the clumps. On the other hand, the near-central absorption dip exhibits a clear global decrease over the two days, with $\triangle I/I_c \sim 0.03$. This systematic variation is significantly larger than the *mean* variation caused by clumps. Such long-term behavior of He II λ 4686 is very similar to what is seen in Hα (constant emission, slowly varying near-central absorption) in ζ Pup by Moffat & Michaud (1981). It remains to be seen whether the λ 4686 central absorption follows the rotation period of $P \sim 5.1$ d as seen in the Hα central absorption.

1.5 Conclusions

The wind of ζ Puppis shows spectral substructures similar to those seen in the winds of Wolf-Rayet stars, which are the likely descendants of O and Of stars. These substructures are likely the consequence of excess emission from clumps caused by supersonic, compressible turbulence in the wind. These observations lead naturally to the important question whether in fact all winds in hot stars show such turbulence at one level or another. We note the following for He II λ 4686 in ζ Puppis:
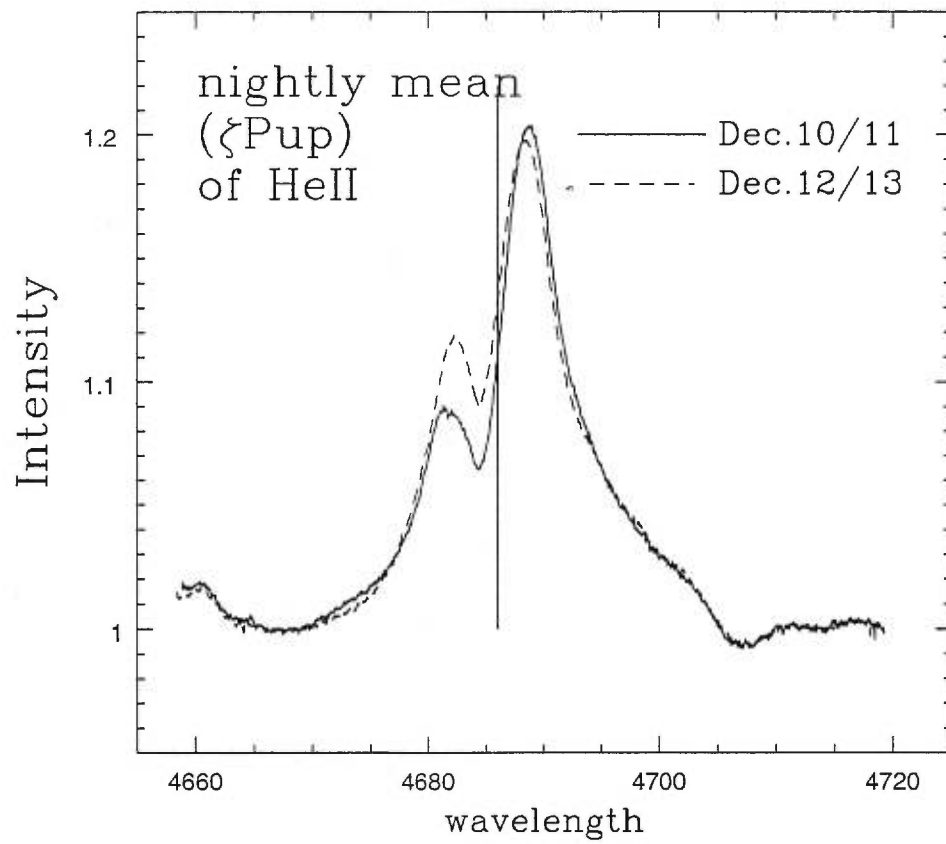
Figure 1.9. Nightly mean of Dec.10/11 (solid line) compared to Dec.12/13 (dashed line).

1. As the substructures accelerate towards the blue/red wing of the line, they tend to smear out. Their velocity width is larger when looking along the line-of-sight. Both of these are observed in WR spectral lines.

2. The variation profile across the line, $\sigma(\lambda)$, follows the emission line profile itself, with $\sigma(\lambda)/I(\lambda) \sim 5\%$ and some increase in $\sigma(\lambda)$ on the blue side, as seen in WR lines (Robert 1992). This is compatible with the whole wind being affected by stochastic variations.

3. Tracing individual substructures and comparison with the standard β-velocity law yields $\beta \sim 1.0 - 1.2$, somewhat larger than the standard value for OB winds ($\beta = 0.8$).

4. Using a standard 'β' velocity law for ζ Pup with an adopted stellar radius $R_\star = 18$ $R_\odot$ (Kudritzki, Simon & Hamann, 1983) and a terminal velocity of $v_\infty = 2250$ km/s (Puls et al. 1996), all blobs in He II λ 4686 appear near the star's surface and disappear at $\sim 2R_\star$.

5. The near central absorption component apparently varies slowly on a nightly basis, much like that seen previously for ζ Pup in Hα (Moffat & Michaud 1981), with $P \approx 5$d. This variation is likely coupled to the stellar rotation.

Recently Puls et al. (1996) presented a new method to determine mass-loss rates of O stars from Hα line profiles using NLTE techniques, along with the β-law *Ansatz* for the wind velocity. For ζ Puppis their calculations yield $\beta = 1.15$, which is in very good agreement with our observations. They state that *"...the wind emission contribution to Hα for O-stars comes from lower wind layers, typically between 1.0 and 1.5 stellar radii. Very recent hydrodynamical simulations for self-excited wind instabilities show that these layers are unaffected by shocks and that instabilities only occur further out in the wind..."*. However, in ζ Puppis we have observed clumping in the He II λ 4686 line at radii *below* $R \sim 1.5R_\star$. Hence, we presume that the Hα line is also affected by clumping. This would thus imply that

mass-loss rates of ζ Pup (and possibly for all O-stars) calculated from the Hα line profile are overestimated, due to the density-squared dependence of recombination emission, as in WR winds (Moffat & Robert 1994).

1.6 Acknowledgments

References

Baade, D. 1986, in Proc. NATO Workshop, Seismology of the Sun & the Distant Stars, ed. D.O. Gough, (Reidel:Dordrecht), p.465

Baade, D. 1988, in O Stars and Wolf-Rayet Stars, eds. P.S. Conti & A.B. Underhill, (NASA SP-497), p. 137

Baade, D. 1991, in ESO Workshop on Rapid Variability of OB Stars: Nature & Diagnostic Value, ed. D. Baade, ESO Proc. No. 36, p. 21

Berghöfer, T.W., Baade, D., Schmitt, J.H.M.M., Kudritzki, R.-P., Puls, J., Hillier, D.J., Pauldrach, A.W.A. 1996a, A&A, 306, 899

Berghöfer, T.W., Schmitt, Cassinelli, J.P. 1996b, A&AS, 118, 481

Blaauw, A. 1993, ASPC, 35, 207

Bohannan, B., Abbott, D.C., Voels, S.A., Hummer, D.G., 1986, ApJ, 308, 728

Chiueh, T. 1997, ApJ, 482, L179

Chlebowski, T., Harnder, F.R., Sciortino, S. 1989, ApJ, 341, 427

Cranmer, S.R., Owocki, S.P. 1996, ApJ, 462, 469

Ebbets, S.D. 1982, ApJS, 48, 399

Feldmeier, A., Kudritzki, R.-P., Palsa, R., Pauldrach, A.W.A., Puls, J. 1997, A&A, in press

Harries, T., Howarth, I.D. 1996, A&A, 310, 533

Henriksen, R.N. 1994, ApSpSc, 221, 25

Hillier, D.J., Kudritzki, R.-P., Pauldrach, A.W.A., Baade, D., Cassinelli, J.P., Puls, J., Schmitt, J.H.M.M. 1993, A&A, 276, 128

Howarth, I.D., Prinja, R.K., Massa, D. 1995, ApJ, 452, L65

Johnson, H.L. 1965, ApJ, 141, 923

Kaper, L., Henrichs, H.F., Nichols, J.S., Snoek, L.C., Volten, H., Zwarthoed, G.A.A. 1996, A&AS, 116, 257

Kudritzki, R.-P., Simon, K.P., Hamann, W.-R. 1983, A&A, 118, 245

Moffat, A.F.J., Michaud, G. 1981, ApJ, 251, 133

Moffat, A.F.J., Robert, C. 1992, in: Nonisotropic and Variable Outflows from Stars, A.S.P. Conference Series, Vol.22, eds. L. Drissen, C. Leitherer & A. Nota, p.203

Moffat, A.F.J., Robert, C. 1994, ApJ 421, 310

Owocki, S.P. 1994, ApSpSc, 221, 3

Pauldrach, A.W.A., Puls, J., Kudritzki, R.-P. 1986, A&A, 164, 86

Prinja, R.K., Howarth, I.D. 1986, ApJS, 61, 357

Prinja, R.K. 1988, MNRAS, 231, 21

Prinja, R.K. 1992, in: Nonisotropic and Variable Outflows from Stars, A.S.P. Conference Series, Vol.22, eds. L. Drissen, C. Leitherer & A. Nota, p.167

Puls, J., Kudritzki, R.-P., Herrero, A., Pauldrach, A.W.A., Haser, S.M., Lennon, D.J., Gabler, R., Voels, S.A., Vilchez, J.M., Wachter, S., Feldmeier, A. 1996, A&A, 305, 171

Reid, A.H.N., Howarth, I.D. 1996, A&A, 311, 616

Robert, C. 1992, Ph.D. Thesis, Département de Physique, Université de Montréal

Schaerer, D., Schmutz, W., Grenon, M. 1997, ApJL (1 Aug)

van der Hucht, K.A., et al. 1997, New Astronomy, in press

Walborn, N.R. 1972, AJ, 77, 312

Chapter 2

The William-Wehlau Spectropolarimeter: Observing Hot Stars in all Four Stokes

Thomas Eversberg[1,2], Anthony F.J. Moffat[1,2], Michael
Debruyne[3,2], John B. Rice[4], Nikolai Piskunov[3,5], Pierre Bastien[1],
William H. Wehlau[3,6] and Olivier Chesneau[7]

2.1 Abstract

We introduce a new polarimeter unit which, mounted at the Cassegrain focus of any telescope and fiber-connected to a fixed CCD spectrograph, is able

[1]Département de Physique, Université de Montréal, C.P. 6128, Succ. Centre-Ville, Montréal, QC, H3C 3J7, Canada, and Observatoire du mont Mégantic

[2]Visiting Astronomer, University of Toronto Southern Observatory, Las Campanas, Chile

[3]Department of Physics and Astronomy, The University of Western Ontario, London, ON, N6A 3K7, Canada

[4]Brandon University, 270 - 18th Street, Brandon, MB, R7A 6A9, Canada

[5]Uppsala University, Box 5151, S-751 20 Uppsala, Sweden

[6]deceased

[7]Observatoire de la Côte d'Azur, 2130 route de l'Observatoire, Caussols, 06460 St. Vallier de Thiey, France

to measure all Stokes parameters I, Q, U and V across spectral lines of bright stellar targets and other point sources in a quasi-simultaneous manner. Applying standard reduction techniques for linearly and circularly polarized light we are able to obtain photon-noise limited line polarization. We briefly outline the technical design of the polarimeter unit and the linear algebraic Mueller calculus for obtaining polarization parameters of any point source. In addition, practical limitations of the optical elements are outlined.

We present first results obtained with our spectropolarimeter for four bright, hot-star targets: We confirm previous results for Hα in the bright Be star γ Cas and find linear depolarization features across the emission line complex C III /C IV (λ 5696/λ 5808 Å) of the WR+O binary γ^2 Vel. We also find circular line polarization in the strongly magnetic Ap star 53 Cam across its Hα absorption line. No obvious line polarization features are seen across Hα in the variable O star θ^1 Ori C above the $\sigma \sim 0.2\%$ instrumental level.

2.2   Introduction

Obtaining polarization spectra of stars is a relatively young topic. Only a few instruments exist for mid- and large-size telescopes – needed to detect the generally low polarization levels. Most popular is the use of a rotatable half-wave retarder plate along with a crystal polarizer to measure linearly polarized light. Examples of where this is done are the Anglo-Australian (Bailey 1991) and Herschel (Tinbergen & Rutten 1992) telescopes. At Keck the so-called "dual-waveplate" method is used (see, e.g., Cohen et al. 1996, Goodrich et al. 1995) consisting of a quarter-wave and a half-wave plate. Using a quarter-wave plate (QWP), e.g., at ESO/CASPEC, allows one to measure circularly polarized light (Mathys & Stenflo 1986). However, there are only a few instruments able to conveniently measure both linearly and circularly polarized light together. A very recent example is the new spectropolarimeter at the Bernard Lyot Telescope at

Pic Du Midi (Donati et al. 1997).

Some stars are well known to show intrinsic linear (e.g., St-Louis et al. 1987) as well as circular (e.g., Borra & Landstreet 1980) *continuum* polarization. The main sources of intrinsic continuum polarization are electron (Thomson) and (less important) Rayleigh scattering in stellar atmospheres and environments, whereas non-relativistic gyrating electrons in magnetic fields yield broadband linear *and* circular polarization (e.g., Schmidt 1988). Interstellar grains normally lead to smoothly wavelength-dependent linear polarization (Serkowski et al. 1975), with low-amplitude circular polarization crossing over at linear peak (Martin & Campbell 1076). Intrinsic *line* polarization can occur due to the Zeeman effect (circular and to a lesser extent linear, depending on the magnetic field strength and orientation) and asymmetries between line and continuum sources (linear). For example, emission lines formed further out in a stellar wind are generally less polarized, leading to linear depolarization across the line, if asymmetries such as wind flattening are present (Schulte-Ladbeck et al. 1992).

Spectropolarimetry is relatively rarely used in stellar astronomy. In this paper we focus on spectropolarimetry of hot stars only, for which the main difficulties are:

- The degree of hot-star (from $T_{eff} = 7500\,\mathrm{K}$ for an A9 star to $50\,000\,\mathrm{K}$ for an O3 star) polarization is often much less than 1% in the continuum, 0.1% in lines (excluding Ap stars), which requires long exposure times and/or large telescopes.

- If in a stellar atmosphere, the source of electron (or Rayleigh) scattering shows radial symmetry, most of the polarization cancels out. As a consequence, deviations from spherical symmetry or a structured wind are the fundamental conditions for detection of intrinsic, non-magnetic linear polarization.

- A global stellar magnetic dipole is the field configuration with the highest probability of detection in circular polarization. Detection of higher order or localized dipole field geometries is more difficult, requiring high spectral resolution aided by stellar rotation or wind expansion.

On the other hand the step from measuring broadband to measuring narrowband (i.e. spectral) polarization allows one to better disentangle the global structure of hot star winds and/or to provide more detailed information about magnetic field geometries. Furthermore it is of great interest to measure both linear *and* circular polarization at the same (or nearly so) time, since, e.g., in hot stars, the magnetic configuration creating circular line polarization is expected to be associated with wind asymmetries yielding linear polarization. For a more detailed review about the use of spectropolarimetry in hot stars we refer to Eversberg (1996).

2.3   The Polarimeter Unit and the Mueller Calculus

The newly built William-Wehlau-Spectropolarimeter is a combination of retarder consisting of two rotatable QWP's and a Wollaston prism as beam-splitter and double-beam polarizer, leading light from stellar point sources via a double fiber-feed into a fixed CCD slit spectrograph. The instrument was developed and built at the University of Western Ontario in collaboration with Brandon University (Manitoba) and Université de Montréal (Québec). Figure 2.1 shows the basic design of the polarimeter unit.

The WW Spectropolarimeter performs polarimetric analysis of starlight. It is designed to be mounted at the $\approx$ f/8 Cassegrain focus of medium or large size telescopes. Incoming starlight passes through an input aperture (pinhole, normally with a diameter D = 200 μm) and is collimated by an f/8 system of lenses. The collimated light then passes through the analyzing section of the in-
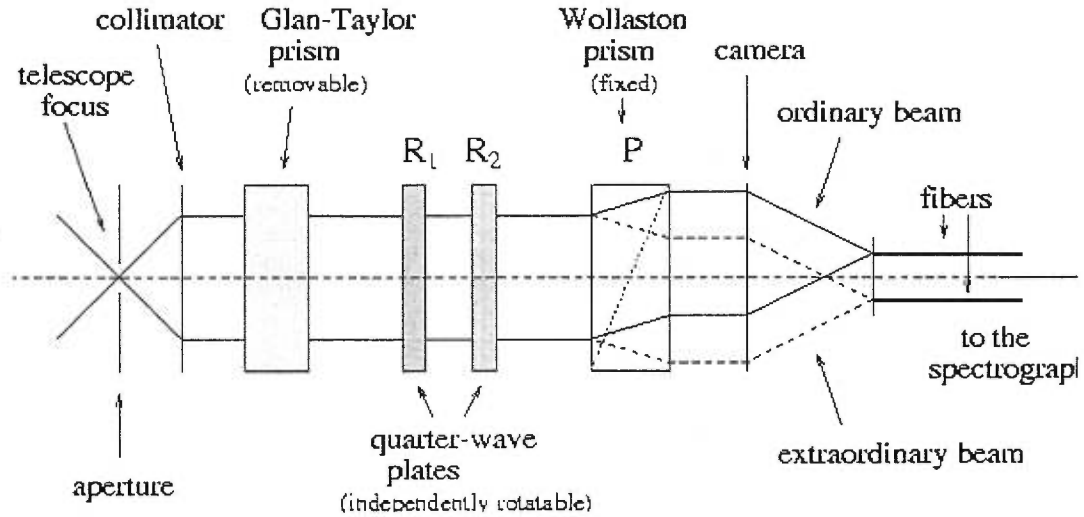
Figure 2.1. Simple sketch of the William-Wehlau-Spectropolarimeter.

strument consisting of two rotatable achromatic AR coated QWP's (controlled by a personal computer), and a fixed Wollaston prism as polarizer. The independent rotation of the QWP's relative to the Wollaston prism determines the polarization components that are being measured. The Wollaston prism separates the components into two linearly polarized beams whose polarization orientations are parallel (ordinary ray, $I_\parallel$) and perpendicular (extraordinary ray, $I_\perp$) to the fast axis of the prism. The two beams exit the Wollaston prism separated by an angle of 0.67°, with each beam deviating the same amount from the optical axis. A zoom lens system then focuses the aperture for each beam to D = 100 μm at f/4 onto twin D = 150 μm optical fibers (silica, step indexed, high OH, polymide buffer) which are separated by 1 mm. Therefore, light that is always ≈ 100 % polarized parallel to the fast axis is focused onto one fiber, while light that is always ≈ 100 % polarized perpendicular to the fast axis is focused onto the other fiber. Note that a deviation between the orientation axes of the Wollaston prism and the zero positions of the QWP's is necessary so that this can occur (see below).

The fibers then feed the light for each beam to the slit of a spectrograph, where the ≈ f/4 emerging light from the fibers is re-imaged to f/8 at the slit.

The spectra of the light from each fiber are imaged so that they are parallel and adjacent, with sufficient space between them on the CCD detector of the spectrograph. The two components can be combined over an observing sequence to obtain all four Stokes' parameters, that fully define the polarization of the light. When the light is dispersed by the spectrograph, the polarization of the starlight may be calculated as the wavelength-dependent quantities $I(\lambda), Q(\lambda), U(\lambda)$ and $V(\lambda)$ via the Mueller calculus (see below).

For calibration purposes and locating the zero position of the QWP's [1], a removable Glan-Taylor prism, which produces nearly 100% linearly polarized light at all optical wavelengths, can be inserted in front of the retarders. The fast axes of the QWP's must first be aligned with the symmetry axis of the Wollaston prism to obtain simple orientation relations for the polarimetric output. This can be entirely done automatically using a computer algorithm or step-by-step by rotating each QWP to locate intensity extrema of the 100% polarized beam exiting the Glan-Taylor prism. The polarization axis of the Glan-Tayler prism is normally aligned with the axis of the Wollaston prism. This is necessary to get a simple output for 100% polarized light (maximum in one beam, minimum in the other). The fiber positions are aligned with the Wollaston axis by shining light back through the fibers, whose orientation as well as that of the Wollaston axis is adjusted so that one sees two colinear pairs of beams arriving at the aperture plane (viewed by reflection from behind). The two inner beams of each pair must superimpose onto the aperture for correct alignment.

Following the Mueller calculus and the rules for matrix algebra, we can calculate the four Stokes' parameters for this arrangement with retardance τ (ideally 90°) for both QWP's. With **A** the input Stokes vector (I,Q,U,V) and

---

[1] According to the manufacturer's specifications, the currently installed achromatic QWP's have ideal retardances ($\tau = 90°$) at two wavelengths only, $\lambda = 4300$ and $6000\,\text{Å}$. Between, and out to several $100\,\text{Å}$ beyond these values, the retardance varies in a simple but non-linear fashion between 85° and 95°.

$\mathbf{A}'$ the output Stokes vector (I',Q',U',V') after passing the retarder plates with matrices $\mathbf{R_1}$ and $\mathbf{R_2}$, and the polarizer with matrix $\mathbf{P}$, we have (writing $\mathbf{A}$ and $\mathbf{A}'$ in vertical form):

$$\mathbf{A}' = \mathbf{P} \times \mathbf{R_2} \times \mathbf{R_1} \times \mathbf{A}. \tag{2.1}$$

Note that we can only actually measure intensities I' of the output beams. The general forms of $\mathbf{R_{1,2}}$ and $\mathbf{P}$ (assumed to be well aligned in the beam) are given by Serkowski (2):

$$\mathbf{R} = \begin{pmatrix} 1 & 0 & 0 & 0 \\ 0 & \cos^2 2\psi + \sin^2 2\psi \cos\tau & (1-\cos\tau)\cos 2\psi \sin 2\psi & -\sin 2\psi \sin\tau \\ 0 & (1-\cos\tau)\cos 2\psi \sin 2\psi & \sin^2 2\psi + \cos^2 2\psi \cos\tau & \cos 2\psi \sin\tau \\ 0 & \sin 2\psi \sin\tau & -\cos 2\psi \sin\tau & \cos\tau \end{pmatrix} \tag{2.2}$$

and

$$\mathbf{P} = \frac{1}{2} \begin{pmatrix} 1 & \cos 2\varphi & \sin 2\varphi & 0 \\ \cos 2\varphi & \cos^2 2\varphi & \cos 2\varphi \sin 2\varphi & 0 \\ \sin 2\varphi & \cos 2\varphi \sin 2\varphi & \sin^2 2\varphi & 0 \\ 0 & 0 & 0 & 0 \end{pmatrix} \tag{2.3}$$

where ψ is the rotation angle of the redardation plate axis with respect to the polarizer axis measured counterclockwise as seen looking toward the sky, and φ is the transmission angle of the polarizer ($\varphi = 0°$ for $\parallel$, $\varphi = 90°$ for $\perp$).

Following these expressions for different angular positions of the QWP's and adopting $\tau \equiv 90°$ for both plates, we get a number of resulting equations for the final, observed Stokes parameters, of which the intensity I' (after allowance for various gain factors) contains all the information we need to derive I, Q, U and V of the original beam $\mathbf{A}$. If we indicate the intensity in either of the

detected output beams $I'_{\psi_1,\psi_2,\|}$, $I'_{\psi_1,\psi_2,\perp}$, with respect to the angular values of the two retarders, and orientation of the beams from the polarizer ($\|$ or $\perp$), in this order; F as a time-dependent varying function, which is the same for each beam, here F_{ψ_1,ψ_2} (e.g., atmospheric seeing, transparency); and G the time-independent gain factor for each beam (e.g., fiber transmission, pixel sensitivity), we obtain, for example [2]:

$$I'_{0,0,\|} = 1/2(I+Q)F_{0,0}G_\| \tag{2.4}$$

$$I'_{0,0,\perp} = 1/2(I-Q)F_{0,0}G_\perp \tag{2.5}$$

$$I'_{45,45,\|} = 1/2(I-Q)F_{45,45}G_\| \tag{2.6}$$

$$I'_{45,45,\perp} = 1/2(I+Q)F_{45,45}G_\perp \tag{2.7}$$

$$I'_{0,45,\|} = 1/2(I+U)F_{0,45}G_\| \tag{2.8}$$

$$I'_{0,45,\perp} = 1/2(I-U)F_{0,45}G_\perp \tag{2.9}$$

$$I'_{0,-45,\|} = 1/2(I-U)F_{0,-45}G_\| \tag{2.10}$$

$$I'_{0,-45,\perp} = 1/2(I+U)F_{0,-45}G_\perp \tag{2.11}$$

$$I'_{-45,0,\|} = 1/2(I+V)F_{-45,0}G_\| \tag{2.12}$$

$$I'_{-45,0,\perp} = 1/2(I-V)F_{-45,0}G_\perp \tag{2.13}$$

$$I'_{45,0,\|} = 1/2(I-V)F_{45,0}G_\| \tag{2.14}$$

$$I'_{45,0,\perp} = 1/2(I+V)F_{45,0}G_\perp \quad . \tag{2.15}$$

With these equations we easily obtain the intensity-normalized Stokes parameters q, u and v:

$$q \equiv \frac{Q}{I} = \frac{R_Q - 1}{R_Q + 1} \tag{2.16}$$

---

[2]Intermediate QWP positions are also usable, in principle, though requiring more complicated calculations.

$$u \equiv \frac{U}{I} = \frac{R_U - 1}{R_U + 1} \tag{2.17}$$

$$v \equiv \frac{V}{I} = \frac{R_V - 1}{R_V + 1} \quad , \tag{2.18}$$

with

$$R_Q = \sqrt{\frac{I'_{0,0,\parallel} \cdot I'_{45,45,\perp}}{I'_{0,0,\perp} \cdot I'_{45,45,\parallel}}} \tag{2.19}$$

$$R_U = \sqrt{\frac{I'_{0,45,\parallel} \cdot I'_{0,-45,\perp}}{I'_{0,45,\perp} \cdot I'_{0,-45,\parallel}}} \tag{2.20}$$

$$R_V = \sqrt{\frac{I'_{-45,0,\parallel} \cdot I'_{45,0,\perp}}{I'_{-45,0,\perp} \cdot I'_{45,0,\parallel}}} \quad . \tag{2.21}$$

Note that these double ratios[3] are impervious to both time dependent variations and time independent gain factors (no flat-fielding necessary), as long as the two beams are measured simultaneously on the same part of the detector each time. This is normally the case. They should therefore be purely photon-noise limited. The intensity I, within a constant factor (which will vary smoothly with wavelength, as for any spectrograph), is easy to get from a simple addition of both beams on a given image, after appropriate determination of the gain factors by flat-fielding. Since q, u and v are independent of these gain factors, it is clear that one can obtain much higher precision for them compared to I. Also note that any of the angles ψ of the $\lambda/4$ plates can be replaced by $\psi \pm 180°$ with identical results, providing the surfaces of the plates are not inclined to the optical axis (Serkowski 1974). This is shown in 2-dimensional mode in Table 1 for the two QWP position angles ψ_1 and ψ_2 and the corresponding output $I'_\parallel / I'_\perp$.

If τ deviates from 90°, the matrix $\mathbf{R}$ introduces cross-talk in the output Stokes' parameters. In our case, measured values for the output $I'_\parallel / I'_\perp$ using the

---

[3]This is referred to as self-calibration by Miller et al. (1).

TABLE 2.1. Output matrix for the ratio $I'_\parallel/I'_\perp$ and different QWP positions according to eqns. (4a) − (4l), generalized to include all useful angles that measure one Stokes' polarization parameter at a time, but neglecting $G_\parallel/G_\perp$.

ψ_2 \ ψ_1	−90°	−45°	0°	45°	90°	135°	180°	225°
−180°	$\frac{I+Q}{I-Q}$	$\frac{I+V}{I-V}$	$\frac{I+Q}{I-Q}$	$\frac{I-V}{I+V}$	$\frac{I+Q}{I-Q}$	$\frac{I+V}{I-V}$	$\frac{I+Q}{I-Q}$	$\frac{I-V}{I+V}$
-135	$\frac{I-U}{I+U}$	$\frac{I+Q}{I-Q}$	$\frac{I+U}{I-U}$	$\frac{I-Q}{I+Q}$	$\frac{I-U}{I+U}$	$\frac{I+Q}{I-Q}$	$\frac{I+U}{I-U}$	$\frac{I-Q}{I+Q}$
−90°	$\frac{I+Q}{I-Q}$	$\frac{I+V}{I-V}$	$\frac{I+Q}{I-Q}$	$\frac{I-V}{I+V}$	$\frac{I+Q}{I-Q}$	$\frac{I+V}{I-V}$	$\frac{I+Q}{I-Q}$	$\frac{I-V}{I+V}$
−45°	$\frac{I+U}{I-U}$	$\frac{I-Q}{I+Q}$	$\frac{I-U}{I+U}$	$\frac{I+Q}{I-Q}$	$\frac{I+U}{I-U}$	$\frac{I-Q}{I+Q}$	$\frac{I-U}{I+U}$	$\frac{I+Q}{I-Q}$
0	$\frac{I+Q}{I-Q}$	$\frac{I+V}{I-V}$	$\frac{I+Q}{I-Q}$	$\frac{I-V}{I+V}$	$\frac{I+Q}{I-Q}$	$\frac{I+V}{I-V}$	$\frac{I+Q}{I-Q}$	$\frac{I-V}{I+V}$
45°	$\frac{I-U}{I+U}$	$\frac{I+Q}{I-Q}$	$\frac{I+U}{I-U}$	$\frac{I-Q}{I+Q}$	$\frac{I-U}{I+U}$	$\frac{I+Q}{I-Q}$	$\frac{I+U}{I-U}$	$\frac{I-Q}{I+Q}$
90°	$\frac{I+Q}{I-Q}$	$\frac{I+V}{I-V}$	$\frac{I+Q}{I-Q}$	$\frac{I-V}{I+V}$	$\frac{I+Q}{I-Q}$	$\frac{I+V}{I-V}$	$\frac{I+Q}{I-Q}$	$\frac{I-V}{I+V}$
135°	$\frac{I+U}{I-U}$	$\frac{I-Q}{I+Q}$	$\frac{I-U}{I+U}$	$\frac{I+Q}{I-Q}$	$\frac{I+U}{I-U}$	$\frac{I-Q}{I+Q}$	$\frac{I-U}{I+U}$	$\frac{I+Q}{I-Q}$

[4]The QWP angles refer to ideal values ψ, not ψ_{obs} − see text. Values of ψ do not run from 0° to 360° for each plate, due to limitations in rotation of the QWP's in the WW spectropolarimeter (cf. Table 2)

Glan-Taylor prism deviate slightly from expected values. This is shown in Table 2, where each matrix element consists of the theoretically expected value above the measured output value $I'_\parallel / I'_\perp$ in brackets.

While modern achromatic polarizing elements (e.g., Glan-Taylor prisms, Wollaston prisms) can be manufactured to very high tolerances, the same cannot be claimed for retarders, even if "superachromatic" (Vats 1997). In an attempt to calculate the real retardance for each QWP at a fixed wavelength, we start with:

$$\mathbf{A}' = \mathbf{P} \times \mathbf{R} \times \mathbf{A}. \tag{2.22}$$

Using the Mueller matrices $\mathbf{P}$ and $\mathbf{R}$, we have for the ordinary beam

$$I'_\parallel = \frac{F_\psi G_\parallel}{2} [I + Q(\cos^2 2\psi + \sin^2 2\psi \cos \tau) + U(1 - \cos \tau) \cos 2\psi \sin 2\psi - V \sin 2\psi \sin \tau] \tag{2.23}$$

and for the extraordinary beam

$$I'_\perp = \frac{F_\psi G_\perp}{2} [I - Q(\cos^2 2\psi + \sin^2 2\psi \cos \tau) - U(1 - \cos \tau) \cos 2\psi \sin 2\psi + V \sin 2\psi \sin \tau]. \tag{2.24}$$

With 100% polarized light in Q (i.e. with the aligned Glan-Taylor prism) we have $U = V = 0$ and $Q = I$ and we get:

$$I'_\parallel = \frac{F_\psi G_\parallel I}{2} [1 + \cos^2 2\psi + \sin^2 2\psi \cos \tau] \tag{2.25}$$

and

$$I'_\perp = \frac{F_\psi G_\perp I}{2} [1 - \cos^2 2\psi - \sin^2 2\psi \cos \tau]. \tag{2.26}$$

For $\tau = 90°$, we have the ideal case:

$$I'_\parallel = \frac{F_\psi G_\parallel I}{2} [1 + \cos^2 2\psi] \tag{2.27}$$

and

$$I'_\perp = \frac{F_\psi G_\perp I}{2} \sin^2 2\psi. \tag{2.28}$$

TABLE 2.2. Example output matrix with the Glan-Taylor prism inserted ($Q = I, U = V = 0$) for the ratio $I'_\parallel/I'_\perp$ and different QWP positions in a narrow band centered near Hα. Each matrix element consists of the theoretical output (with $G_\parallel/G_\perp=1$) and the measured value in brackets. Angles have been corrected to coincide with appropriate extrema (ψ, not ψ_{obs}, see Fig.2.2).

ψ_2 \ ψ_1	$-90°$	$-45°$	$0°$	$45°$	$90°$	$135°$	$180°$	$225°$
$-180°$	∞ (141)	1 (0.87)	∞ (66)	1 (0.98)	∞ (33)	1 (1.09)	∞ (435)	1 (0.81)
$-135°$	1 (1.06)	∞ (132)	1 (1.52)	0 (0.01)	1 (0.79)	∞ (73)	1 (1.16)	0 (0.002)
$-90°$	∞ (179)	1 (0.92)	∞ (109)	1 (0.88)	∞ (34)	1 (1.14)	∞ (455)	1 (0.75)
$-45°$	1 (1.26)	0 (0.009)	1 (0.85)	∞ (222)	1 (1.63)	0 (0.027)	1 (1.16)	∞ (135)
0	∞ (476)	1 (0.68)	∞ (62)	1 (1.15)	∞ (90)	1 (0.84)	∞ (370)	1 (1.00)
$45°$	1 (0.94)	∞ (204)	1 (1.32)	0 (0.022)	1 (0.69)	∞ (233)	1 (1.04)	0 (0.008)
$90°$	∞ (93)	1 (1.12)	∞ (556)	1 (0.72)	∞ (29)	1 (1.36)	∞ (112)	1 (0.62)
$135°$	1 (1.20)	0 (0.021)	1 (0.81)	∞ (667)	1 (1.52)	0 (0.046)	1 (1.15)	∞ (101)

However, $I'_\parallel$ and $I'_\perp$ deviate slightly from the expected ideal output functions at certain angular positions. In detail within the constants $G_\parallel$ and $G_\perp$, $I'_\parallel + I'_\perp$ is conserved, whereas maxima of $I'_\perp$ and minima of $I'_\parallel$ appear to follow a simple sine-wave with rotation angle. This behavior must obviously be caused by small deviations of τ from 90° for both QWP's. By using

$$\cos\tau = c_1 + c_2 \sin\psi + c_3 \cos\psi. \qquad (2.29)$$

we fitted eqns. (9a) and (9b) via χ^2 minimization, leading to $(F_\psi G_\parallel I/2, F_\psi G_\perp I/2) =$ (5303, 4559), $c_1 = 0.050$, c_2 = -0.049 and c_3 = -0.001 for QWP 1 and $(F_\psi G_\parallel I/2, F_\psi G_\perp I/2)$ = (5330,4700), $c_1 = 0.160$, $c_2 = 0.017$ and $c_3 = 0.002$ for QWP 2. The fit also yielded a slight shift of the extrema from their theoretically expected positions, leading to corrections $\psi = 0.994 \cdot \psi_{obs} - 10.12°$ for QWP1 and $\psi = 0.999 \cdot \psi_{obs} - 13.87°$ for QWP2. The deviation from unity of the slopes is likely a consequence of imperfections in the stepping motors.

To illustrate this for the WW polarimeter, we show in Fig. 2.2 for each QWP separately, combined with the aligned Glan-Taylor and Wollaston prisms, how the outputs $I'_\parallel$ and $I'_\perp$ vary compared with predictions.

We dicovered the reason for this behavior by sending a laser-beam through each QWP independently. In transmission, the outcoming beams were geometrically highly stable while rotating the plates, whereas in reflection both plates showed one or two beams that rotated in elliptical patterns around a geometrically stable central beam.

The variation of the effective retardation of the QWPs with rotation angle arises because of the varying angle of inclination that the collimated beam has with the QWP (or one of its individual layers) as the QWP is rotated. If the QWP were mounted in its cell so that the surfaces were not normal to the axis of the cell and the cell axis were properly aligned with the optical axis of the collimated beam, then that one misalignment by itself would produce no change
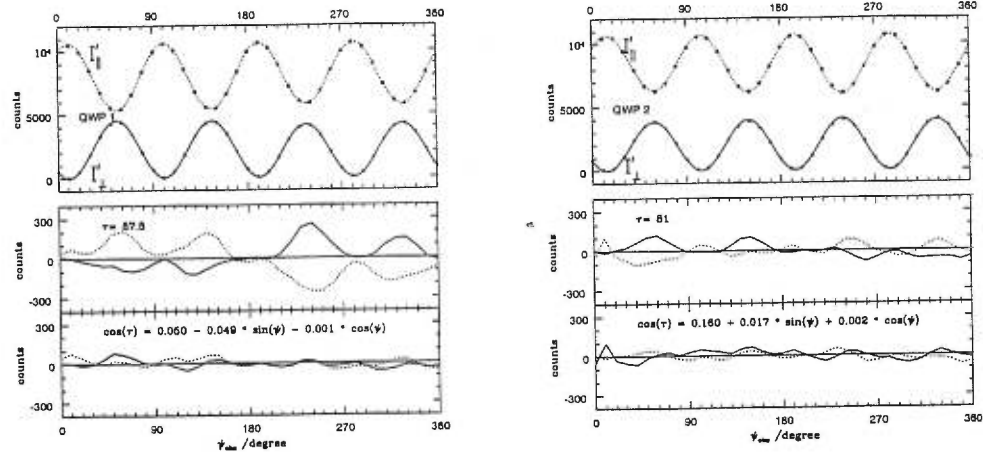
Figure 2.2. Output of the two beams with the Glan-Taylor prism, QWP 1 (left) and QWP 2 (right) and the Wollaston prism, in a narrow band centered near $H\alpha$. Top panel: Open and filled circles, respectively, represent the measured average intensity in the ordinary beam ($I'_\parallel$) and extraordinary beam ($I'_\perp$). The curves represent the fits using eqns. (9a), (9b) and (11) after allowing for a shift in angle to match best our data points. Bottom panel: Top: Residuals from a χ^2 minimum fit for $\tau = $ constant, as indicated for both QWP's. Bottom: Residuals from a χ^2 minimum fit using eq. (11). Values obtained for c_1, c_2 and c_3 are indicated.

in inclination as the cell is rotated. If the cell were rotated about an axis that is misaligned with the optical axis but the QWP were properly mounted normal to the axis of the cell then again there would be no variation in the inclination angle with rotation as a result of that misalignment alone. However, if both misalignments are present, i.e. the orientation of the QWP in its cell is not normal to the axis of rotation *and* the axis of rotation is not aligned with the optical axis, then we have an oblique rotator. As the cell is rotated, the angle of inclination will nod with respect to the optical axis and the effective retardation will vary. If the misalignments are only a few minutes of arc, then the variation will be small, of course. In our case we found that the *front* surface of each multi-element QWP was normal to the rotation axis of the cell but that the air gap between some of the additional components was a wedge so that some parts of the QWP participated in the oblique rotator behaviour. This varying inclination introduces small angle-dependent deviations from the mean retardance (see eqns. 8.3.2 and 8.3.3 in Serkowski 1974). A sine-wave behavior for τ (or $\cos\tau$ for τ moderately close to 90°) is thus quite reasonable, as found above.

The solution to this problem is simple. Either be more careful that there is no misalignment of any of the components of the QWPs in their cells or be careful that the rotation axis is quite precisely aligned with the optical axis. Either will suffice but obviously if both are accomplished the effect we have seen will be removed. It is important to note that we chose to use QWPs with an air gap so that even with variation in the angle of the surfaces of the components to the incident angle of the transmitted beam in a collimated beam situation, there would be absolutely no movement of the image formed by the camera optics. A QWP that is inclined to the collimated beam would generate a displacement of the collimated beam but no deviation in direction. That is a consequence of the fact that a QWP must have, by its very nature, surfaces that are parallel to one another to a very high degree of precision.

It is not obvious that superachromatic retarders (although giving better tolerances on τ close to 90°, compared to the achromats here) would behave much better (Donati et al. 1997), since they are even more complex, requiring more dielectric layers (Vats 1997).

We also obtained a number of exposures of bright stars with the Glan-Taylor prism to measure the overall efficiency and possible cross-talk between different Stokes' parameters at different wavelengths. As seen in Fig. 2.3, cross-talk between different polarization parameters shows wavy structures as a function of wavelength, with an amplitude which never exceeds 4%. Some of the non-zero offset in $\bar{u}$ might be due to a slight misalignment in the rotation of the Glan-Taylor prism. We can however exclude this as the reason for the imperfect behavior of retardance τ with angle and wavelength. We find similar behavior also in our UTSO data in the blue.

The bottom line here is that we can probably eliminate these deviations by applying first-order corrections and/or using better QWP's. For our described observations with imperfect QWP's we minimize the impact on deviations in the final Stokes values by choosing ranges of rotation for the QWP's where the two required ratio peaks are more nearly the same and overall deviations from $\tau = 90°$ are smallest.

2.4 Observations

In order to test the WW polarimeter on the sky, we have observed a number of different hot star prototypes to cover various spectropolarimetric outputs. These include the brightest Be star visible in the sky γ Cas (B0 IVe), the young variable Orion Trapezium star θ^1 Ori C (O7 V) and the strongly magnetized Ap star 53 Cam (A2p). These were observed during two runs at the 1.6m telescope of the Observatoire du mont Mégantic (OMM) in September and December 1997
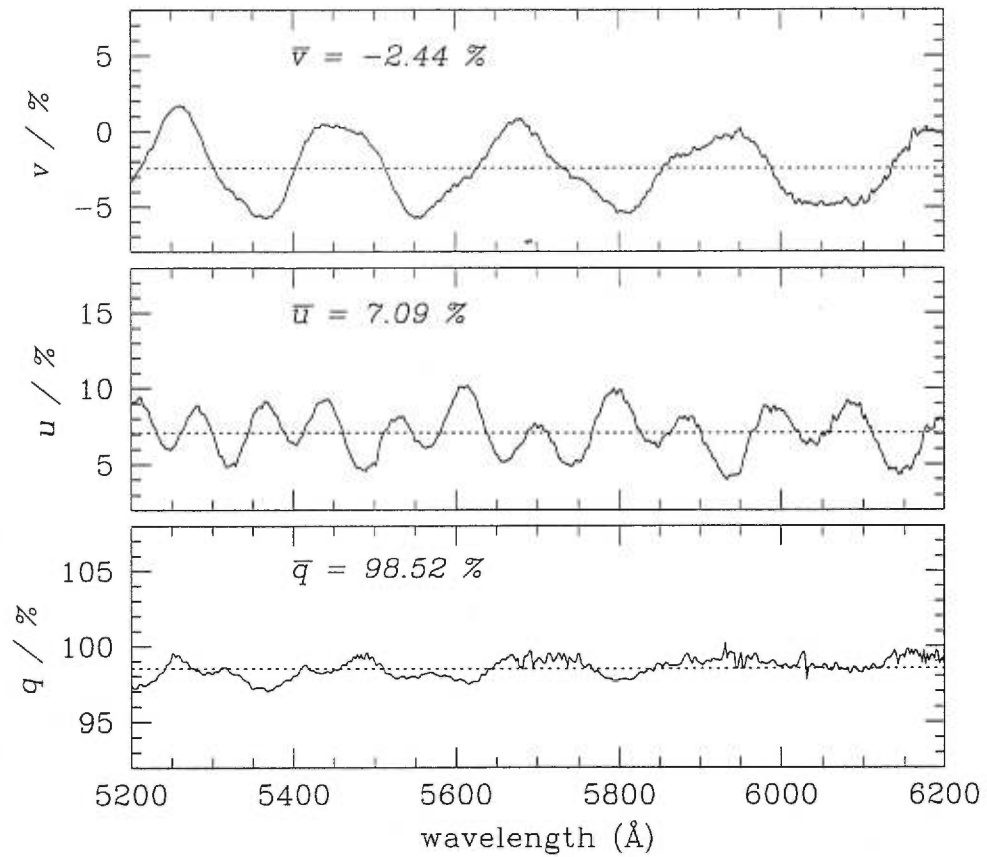
Figure 2.3. Stokes q, u and v for Sirius (α CMa) observed with the Glan-Taylor prism at UTSO. Average values in the wavelength range 5200 – 6200 Å are indicated. Note that v should be zero for a perfect instrument.

using the William-Wehlau spectropolarimeter at the Cassegrain focus. With the 600 l/mm grating of the fiber-fed spectrograph we obtained a net (FWHM) resolution of 1.9 Å in the wavelength range 5800 − 7100Å, to cover mainly Hα, HeI 5876 and HeI λ 6678.

We have also observed the 78-day WR+O binary γ^2 Vel (WC8+O9 I) during a five week run in Feb/March 1997 at the University of Toronto Southern Observatory (UTSO) at Las Campanas, Chile. We obtained spectra during 21 nights within $\Delta\phi \sim \pm 0.2$ of periastron passage. Using the Garrison spectrograph the 3-pixel spectral resolution was about 6 Å in the effective wavelength region 5200 − 6000Å covering mainly the HeII λ 5411, CIII λ 5696, CIV λ 5802/12 and HeI λ 5876 emission lines.

The very first step for each night was the calibration of the QWP positions. For this we sent an artificial light source through the system including the Glan-Taylor prism. With 100% input polarized light, we located where the intensities $I'_{\parallel}$ and $I'_{\perp}$ reached extreme values. Actually, our computer program is able to find these extrema by itself. However, we found a small, but significant inconsistency in the computer output positions, probably introduced by the chromatic- and angle-dependent nature of the quarter-wave plates.

For each program star we obtained a number of exposure sequences, each containing two, four or six spectral images at different QWP positions to measure $v(\lambda)$; $q(\lambda)$ and $u(\lambda)$; or $q(\lambda)$, $u(\lambda)$, $v(\lambda)$; respectively, as indicated above (cf. eqns. (4a) − (6c)). One sequence was obtained with the Glan-Taylor prism when necessary, to correct for possible cross-talk between different Stokes parameters and to evaluate the overall efficiency of detecting polarization. Complete sequences for non-polarized standard stars (e.g. β Cas at OMM and α CMa at UTSO) were also observed. Polarized standards are generally too faint to be observed for our purpose, compounded with a problem of reliably measuring continuum polarization (see below).

A number of flat-field images, wavelength comparison spectra and bias images were obtained at the beginning and end of each night. The procedures for flat-fielding and wavelength calibration were different at each telescope:

- At UTSO we used an internal Tungsten lamp in the optical feeding box between the polarimeter and the telescope for flat-fielding. A Fe-Ne lamp in the same feeding box was used for wavelength calibration.

- At OMM we used the auto-guider of the telescope. For this reason we could not use the feeding optics and obtained dome-flats in the usual manner. For wavelength calibration we used a Cu-Ar lamp in the spectrograph.

As one can see, light from the comparison lamp at UTSO passes through the whole instrument, whereas at OMM the comparison light originated in the spectrograph. Despite these different configurations, we found no significant differences between these techniques.

2.5 Data Reduction

As one can see from the final equations, a full observing sequence for all 4 Stokes parameters consists of 6 exposures at different QWP positions. Each exposure results in a two-dimensional CCD image with two spectra, one for the ordinary beam and one for the extraordinary beam.

After bias subtraction, the possibility of blending between the two beams (see Harries 1995 in the case of an echelle spectrograph, where free space between adjacent orders is limited) was considered. Because of ample separation between the two fibers, both where they receive and deliver the light beams, blending is negligible in our case. In addition we checked for any shift of the spectral pair from one image to another on the CCD chip. This is necessary to avoid division

by different pixels, and hence different sensitivities on the chip, within the same observing sequence. For this reason we cross-correlated the first image in a given fixed wavelength range with all other images in a direction perpendicular to the dispersion. The shift was always found to be negligibly small.

The next step was to check for deviations from ideal geometrical orientation of the spectra on the CCD chip, in order to avoid problems in tracing the apertures when collapsing the spectra (see Donati et al. 1997). The angle between the dispersion direction and the CCD axis was small: 1.0° at UTSO and 0.14° at OMM. With such small angles, we do not have to worry about significant spectral smearing during the extraction.

The reduction procedure was carried out with IRAF and its standard tools. One problem was the strong asymmetric shape and its slight variation with wavelength of one of the spectrum pairs perpendicular to the dispersion in the UTSO data. The IRAF/APSUM task traces the line peak and averages flux perpendicular to the dispersion direction, so that one might expect glitches in tracing the aperture as the peak shifts along the spectrum. After trying different techniques for the two 10-pixel wide spectra separated centre-to-centre by about 30 pixels, we decided to choose broad, 30-pixel windows and use the first nightly spectrum as a template for all other spectra in the same night in the same wavelength range, in order to guarantee division always by the same pixels according to eqns. (6a) – (6c). Note that we have ratioed the two spectra to obtain $q(\lambda)$, $u(\lambda)$, $v(\lambda)$ *after* collapsing to 1D, rather than in the 2D domain. This is quite acceptable (and simplifies the extraction technique), as pointed out below in the context of obtaining $I(\lambda)$. The above procedure was also used for our OMM data, with a window width for collapsing of 30 pixels. We note that tracing the apertures was not a problem here because of symmetric shapes of our two spectra perpendicular to the dispersion.

Cosmic ray (CR) rejection was done iteratively. At first CRs were identified

by eye on the original image and rejected by replacing their intensities by the mean of neighboring unaffected pixels. After collapsing the spectra, any residual spikes in the 1D spectra were deleted by using again the mean of neighboring unaffected pixels after re-identifying them in the 2D input images as cosmic rays. Ratioing the spectra as necessary to obtain q, u and v has the advantage that cosmic rays, found usually only in one aperture at a time, appear as even stronger, easy-to-identify spikes relative to the normally uncomplicated q, u, v spectra, after double-ratioing.

We also subtracted the image background, consisting mostly of dark current, which was extremely small compared to the stellar source. For this, we used a median grid of 5 pixels in windows of 10 pixel width centered at 25 pixels on either side of each beam and a background fit in the dispersion direction of 3rd order. The background level increases linearly with exposure time. This also applies to the OMM data, but with a background window of 30 pixel width.

As a final test we extracted the spectra by using simple averages of image windows independent of IRAF/APSUM. We calculated a 20 pixel wide average on the spectra and subtracted 10 pixel wide background averages on both sides of each beam. There is no significant difference between this and the IRAF result. For this reason we took the easy route by extracting all the spectra in one step within IRAF.

Because $I(\lambda)$ cannot be obtained from double-ratios as can q, u and v but must be obtained from simple additions of two spectra in one image, we are obliged to reduce pixel-to-pixel variations $I'(\lambda)$ by flat-fielding. This reduction step was done after collapsing the flats to 1D spectra using the same nightly template as for starlight. This is possible because the two beams always have the same *relative* pixel-to-pixel illumination, even always the same $\approx 100\%$ linear polarization input into each of the ordinary and extraordinary beam fibers. The only thing that varies at a given wavelength is the relative intensity of each beam,

regardless of the spectral and polarimetric details of the stellar source.

The wavelength calibration was carried out for each beam separately using the same nightly stellar extraction template. This was done *before* double-ratioing the spectra to avoid any shift in wavelength space (e.g., due to the dispersion direction being inclined to the CCD axis) between the two spectra. For best results we determined individual residuals of each arc with respect to its rest wavelength and eliminated strong deviators. A fifth order Legendre polynomial fit related pixel positions to wavelength. The wavelength drift between comparison spectra taken at the beginning and the end of the night was found to be negligibly small. This is not surprising, in view of the stable configuration with the fiber-fed spectrograph fixed in the dome.

After computing all Stokes' parameters for γ^2 Vel we found that the continuum polarization varies from one polarization sequence to the next. Further examination revealed that this occurs for all observed stars and thus must be instrumental in origin. The continuum polarization varies in such a way that strong stochastic deviations from the mean arise, combined with varying gradients $\delta q/\delta\lambda$, $\delta u/\delta\lambda$ and $\delta v/\delta\lambda$. Two examples for consecutive sequences of Stokes q, u and v obtained at UTSO and OMM are given in Fig. 2.4.

A typical stochastic rms scatter of $\sim 1\%$ broadband continuum polarization is found in q, u and v at both telescopes. The most likely explanations for this are due to (1) small variations in overall illumination of the two fibers, whose spatial surface sensitivities are never perfectly uniform, and (2) possible metallic aperture edge effects, both caused ultimately by seeing/guiding fluctuations. The first effect dominates in our data, since it appears equally in q, u and v, whereas the second effect is only expected in q and u. These two effects introduce a time dependence in the gain factors, G (see eqns. (4) above), that are different for the two beams. These effects also appear to be worse at blue wavelengths. We believe this is due to wavelength-dependent sensitivity at the fiber-face, that degrades
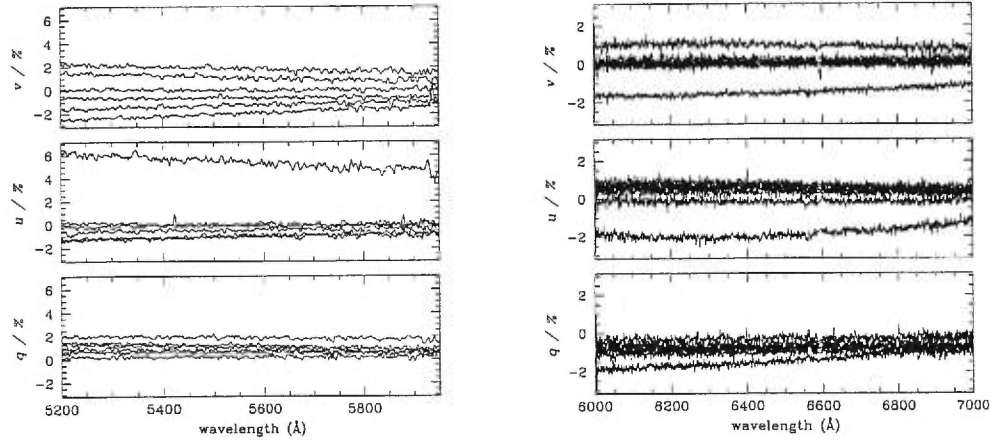
Figure 2.4. Left: Six consecutive observing sequences of Stokes q, u and v for γ^2 Vel during one night at UTSO (hand guided). Right: Seven consecutive sequences of γ Cas during one night at OMM (auto-guided).

gradually towards shorter wavelengths, as is well known for fiber transmission. Note that at OMM we used the auto-guider, whereas at UTSO guiding was done by eye, leading to somewhat better results at OMM. We find support for the assumed instrumental origin of this scatter by obtaining all Stokes' parameters for dome flats, which illuminate the fibers more uniformly and invariably with time. As one can see in Fig. 2.5, the broadband output is stable within ~ 0.04 %, i.e. the Poisson noise level.

Donati et al. (1997) have had the same experience with their twin fiber-fed spectropolarimeter. This appears to be a general limitation of such double-fiber configurations. In our polarimeter the pinhole-aperture is imaged onto the fibers. A possible (but difficult) way to avoid variations in broadband polarization could be via imaging of a pupil instead of the star onto the fibers, using Fabry lenses, and via use of a non-metallic aperture.

As a starting point to circumvent the problem of instrumental variations in continuum polarization, we applied a weighted linear fit to all UTSO $q(\lambda), u(\lambda), v(\lambda)$
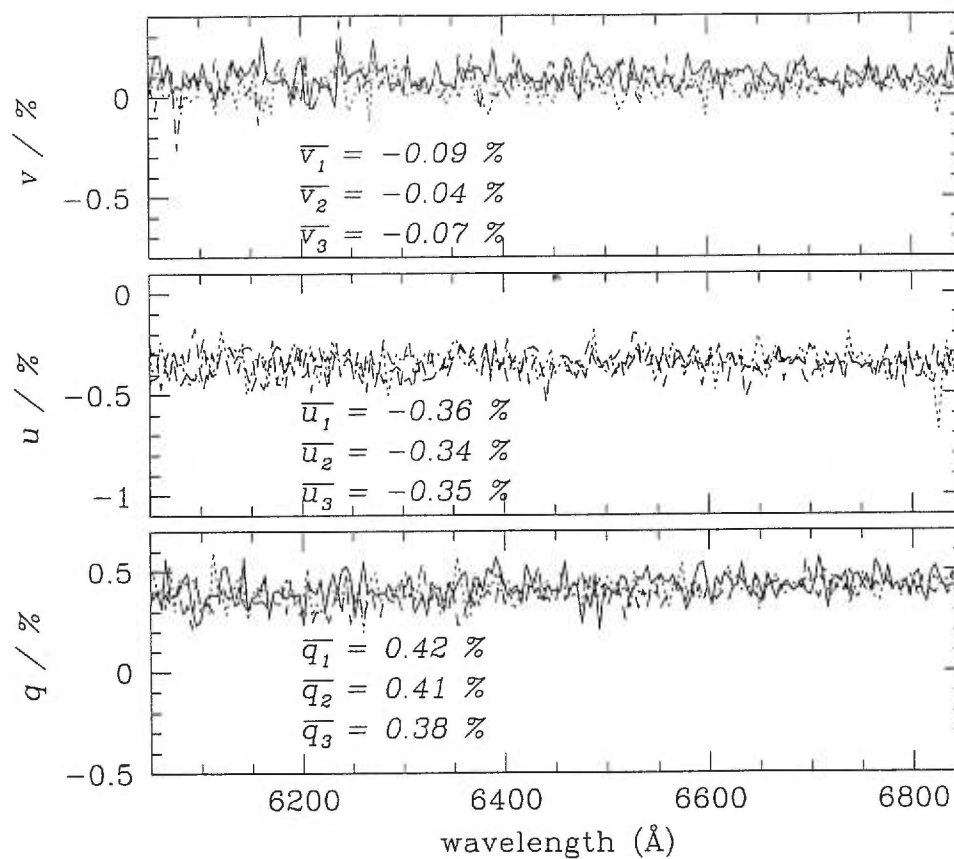
Figure 2.5. Three consecutive observing sequences of Stokes q, u and v for dome flats at OMM. Average values for q, u and v in the wavelength range $6050 - 6850$ Å are indicated. The non-zero means in q and u are likely due to a small level of linear polarization in the dome flat light.

spectra, yielding a slope and zero point, neglecting interstellar polarization. (For the OMM data we used a parabolic fit.) Along with other observations, the data in Fig. 2.4 give the impression that the curves tend to converge to the red. In fact, we found a fairly clear correlation between the slopes and their corresponding zero points. However, when applied to the data, the noise of this correlation would introduce continuum variations of up to 2%, which is not acceptable. Thus, we cannot estimate the exact continuum polarization. For this reason we simply subtracted a fit to the original individual Stokes q, u and v spectra in each sequence and thus neglected broadband polarization, when combining sequences to get mean $q(\lambda)$, $u(\lambda)$ and $v(\lambda)$ spectra. This procedure allows us to obtain reliable, empirical estimates of the *scatter* in polarization as a function of wavelength. On the other hand, *small-scale relative variations of polarization with wavelength (i.e. line polarization), the main goal of this instrument, are impervious to this broadband effect.*

After combining to average q, u and v spectra for various stars of the whole UTSO run, we found Mexican-hat features at atomic line positions in *all* observed absorption lines in *all* Stokes spectra. The amplitude was typically $\sim 0.1\%$ polarization for narrow absorption lines of depth ~ 0.9 continuum. This is small but quite significant and difficult to see even in *nightly* mean spectra. Apparently, the beam that contains enhanced intensity $(I + Q, I + U, I + V)$ – even for $q = u = v = 0$ – broadens the stellar spectrum, regardless of whether in the ordinary beam or in the extraordinary beam. This induces artificial features in Stokes q, u and v at wavelengths where the intensity spectra have strong gradients $\delta I / \delta \lambda$. The origin of this behavior is completely unknown. It is not intrinsic to the stars, since it occurs in all lines the same way in q, u, v. If it were due to the spectrograph, it should have cancelled out in the double-ratio in equations (6a) – (6c), which is not the case. We first presumed that one or both of the QWP's introduce this phenomenon. However, these features do not appear in our OMM data and it is more likely that our setup at UTSO introduced this behavior in a

way that lacks an obvious explanation.

In an attempt to eliminate this effect in the UTSO data, we convolved the mean intensity spectrum I_λ with a gaussian G_λ containing σ as a free parameter. From this we obtained a modified spectrum S_λ:

$$S_\lambda = \frac{I_\lambda}{I_\lambda \otimes G_\lambda}. \tag{2.30}$$

This function gives the form of a Mexican hat for narrow lines and resembles the observed spurious line polarization very well. We obtained a best fit with σ = 0.37 pixel (~ 0.68 Å) for all stars. Examples of this procedure are given in Fig. 2.6 and 2.7.

After subtraction of S_λ from individual nightly mean Stokes spectra at UTSO, we obtained the final wavelength dependent Stokes parameters $q(\lambda), u(\lambda)$ and $v(\lambda)$. To increase the precision without significant loss in resolution we binned all Stokes spectra to an effective resolution of 2 Å for the OMM data and 6 Å for the UTSO data.

2.6 Results

2.6.1 γ^2 Velorum

As noted in section 3, spectropolarimetric data of γ^2 Vel were obtained during an extended run at UTSO in Feb/March 1997. In this nearby binary system with an orbital period of 78.5 days (Schmutz et al. 1997, who also give a complete description of the orbit), the two wind components create a shock cone around the weaker-wind O star (St.-Louis et al. 1993). The variable excess emission in the lines of C III $\lambda\,5696$ Å and C IV $\lambda\,5808$ Å are presumed to be created by radiative cooling downstream along the cone. The opening angle of the cone depends on the
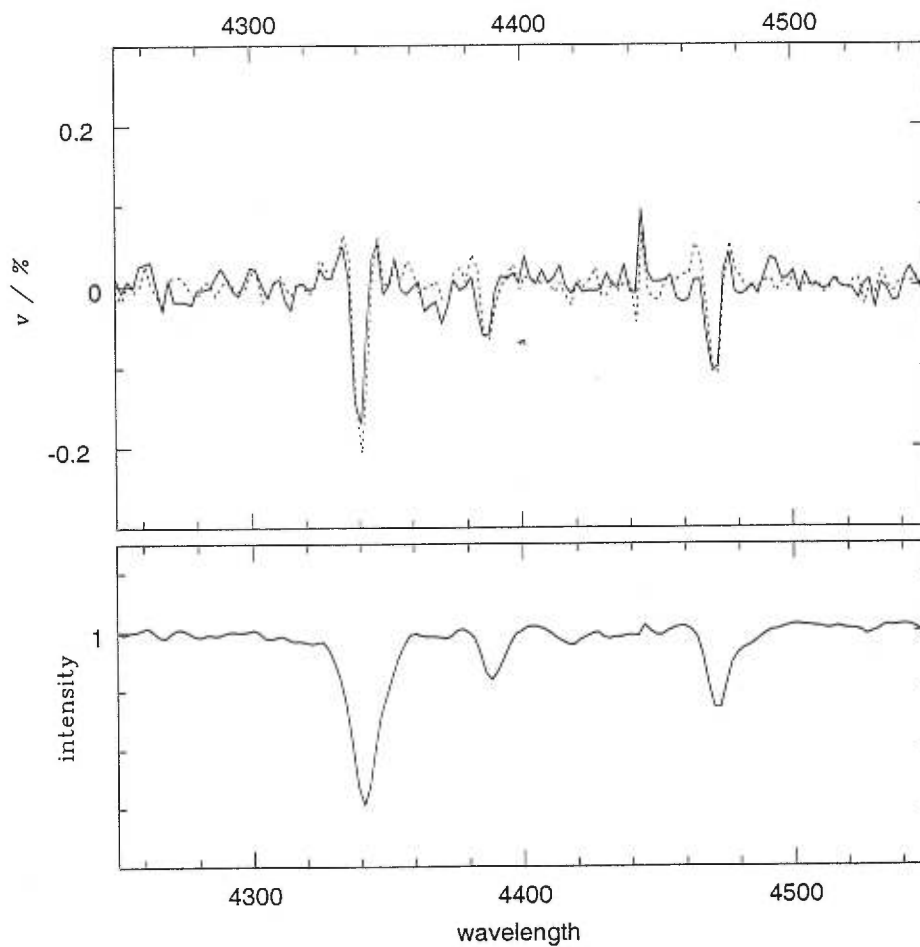
Figure 2.6. Simulation of polarization features with artificially broadened spectra, S_λ (see text). Bottom: Mean spectrum of $\eta\, Cen$. Top: Stokes v (solid) and S_λ (dashed).
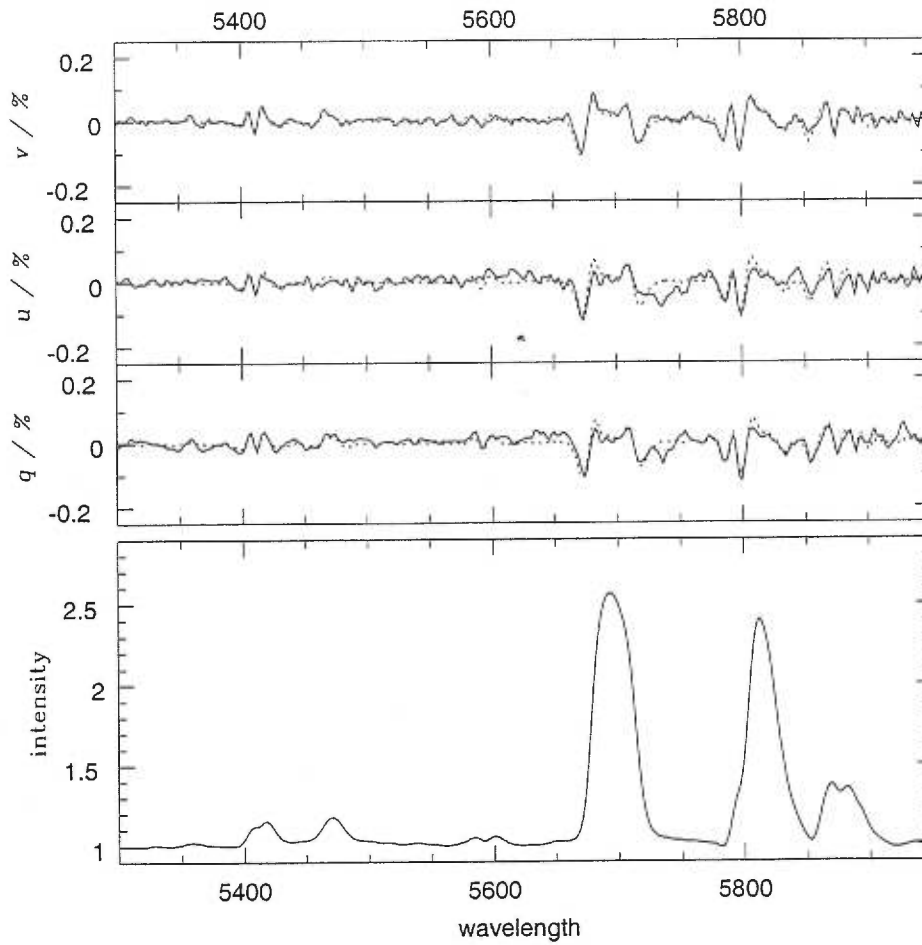
Figure 2.7. Simulation of polarization features with artificially broadened spectra, S_λ (see text). Bottom: Mean spectrum of γ^2 Vel. Top: Stokes q, u and v (solid) and S_λ (dashed).

relative wind momentum fluxes of the two stars. This shock-cone introduces a deviation from spherical symmetry in the wind so that, in principle, it could lead to phase-dependent intrinsic continuum polarization. Even more important to create phase-dependent continuum polarization, however, is the scatter of O-star light from free electrons in the asymmetrically located WR wind (see St-Louis et al. 1993 for γ^2 Vel and other WR+O binaries). On the other hand, WR emission-line flux in a binary will be essentially unpolarized, so that phase-dependent variations of depolarization will occur at the positions of the emission lines (see Moffat & Piirola 1994). We note that constant linear line depolarization can also occur for a flattened WR wind (Schulte-Ladbeck et al. 1992).

Our observations were carried out over orbital phases centered on periastron passage, i.e. $\phi = 0.0 \pm 0.2$. Figure 2.8 shows all four obtained Stokes parameters I, q, u and v, averaged over the whole run.

Orbital phase effects have probably diluted the net line polarization, which is expected to be largest at orbital phases when the stars are seen at quadrature. Unfortunately, individual nightly mean spectra are not of sufficient S/N to extract this information. We report significantly different values in both Stokes q and u across strong emission lines compared to the continuum. Since γ^2 Vel is known to show phase-dependent broadband polarization, especially near periastron (St-Louis et al. 1993), it is reasonable to assume that we are seeing line depolarization effects here. We draw attention to additional linear depolarization in the electron scattering (redward) wing of C III $\lambda 5696$.

We find no significant circular polarization across any lines along the whole mean spectrum, above the instrumental level of $\sim 0.03\,\%$.
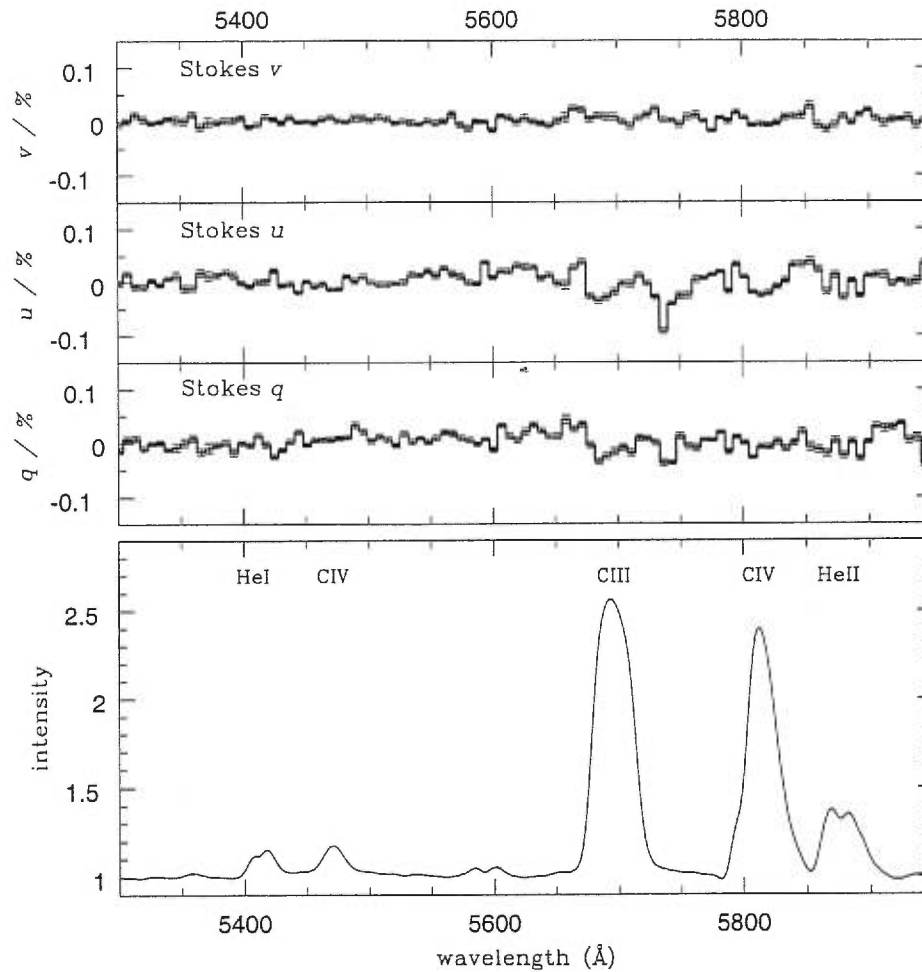
Figure 2.8. Mean rectified intensity spectrum of γ^2 Vel and mean normalized Stokes parameters q, u and v for the whole run combined, after removal of the spectral broadening effect. The polarimetric data have been binned by a 3-pixel box-car; 2σ errorbars are indicated.
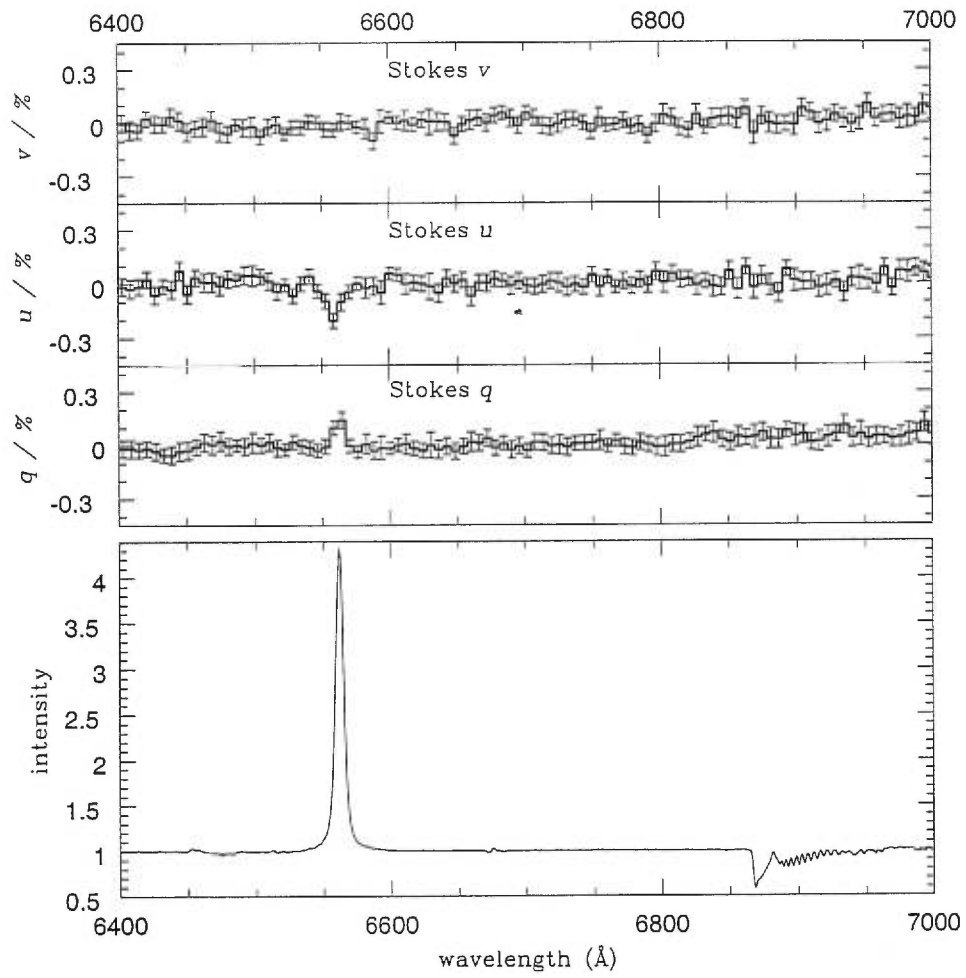
Figure 2.9. Global mean rectified intensity spectrum including Hα, and mean Stokes q, u and v for γ Cas. 2σ errorbars are indicated for bins of 5 pixels.
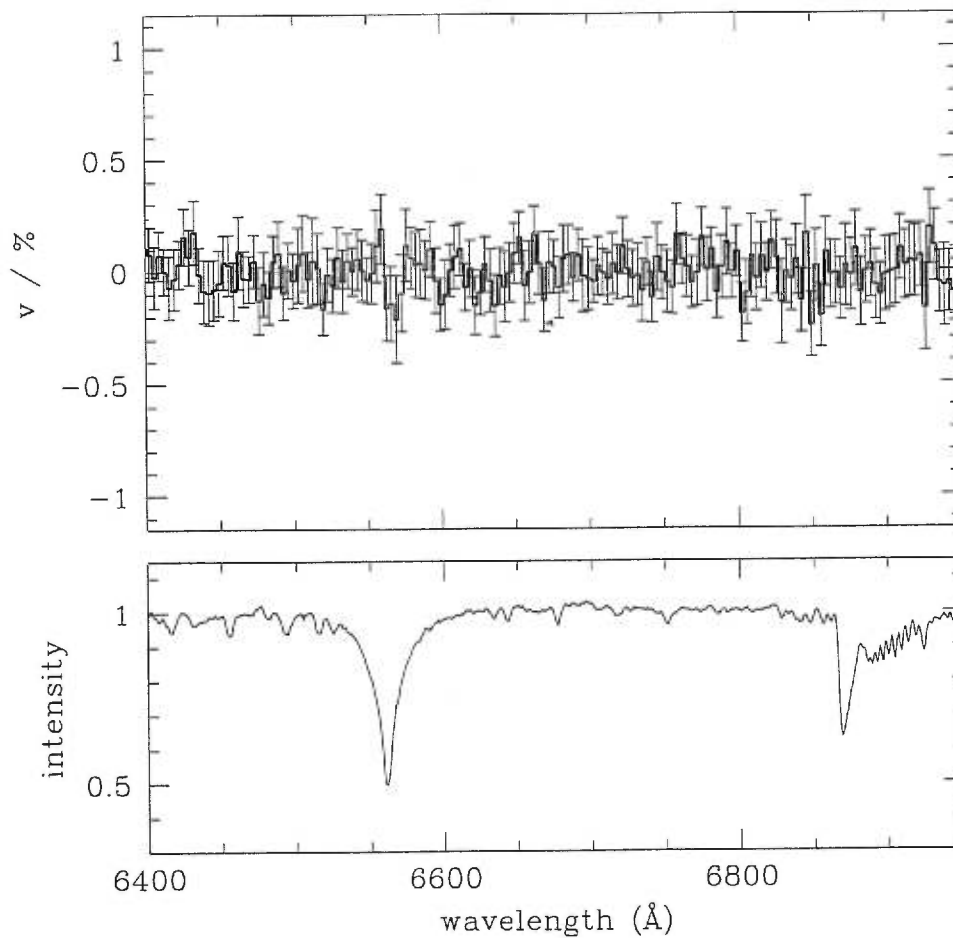
Figure 2.10. Mean rectified intensity spectrum of 53 Cam and mean normalized Stokes v for Dec 21. The polarimetric data have been binned to 5 pixels; 2σ errorbars are indicated.

Though 1σ errorbars are about 0.1% in Stokes v, we report significant rise and fall of $\sim 0.15\%$ on the blue and red sides, respectively, of the centre of Hα, as expected at this phase from previous work (Borra & Landstreet 1980).

2.6.4 θ^1 Ori C

The brightest star in the Orion trapezium is the O7 V star θ^1 Ori C. This star, one of the closest O stars in the sky, is the principle ionization source of M 42 and spectroscopically variable in the optical (Conti 1972, Walborn 1981) as well as in the UV (Walborn & Panek 1984). Stahl et al. (1993) and Walborn & Nichols (1994) report an asymmetry in its wind and a stable 15.4-day modulation over at least 15 years. They conclude that this behavior is reminiscent of a magnetic oblique rotator with a surface field of about 1800 Gauss. Reported X-ray modulation in the 15-day cycle (Gagné et al. 1997; Babel & Montmerle 1997) is compatible with a surface field of several 100 G. This proposed magnetic field and the wind asymmetry makes θ^1 Ori C a strong candidate for showing phase-dependent circular as well as linear polarization effects across its lines.

We observed this star during 2 nights (Dec 21/22 and 22/23) at OMM. The average intensity and Stokes q and u (2nd night only) and v (1st night only) spectra are shown in Fig. 2.11. Note that the nebular Hα emission in $I(\lambda)$ has not been removed.

No obvious line polarization features are seen above the $\sigma \sim 0.2\%$ instrumental level.

2.7 Summary

We have introduced a new type of polarimeter unit which, mounted at the Cassegrain focus of any telescope and combined with a standard CCD spectro-
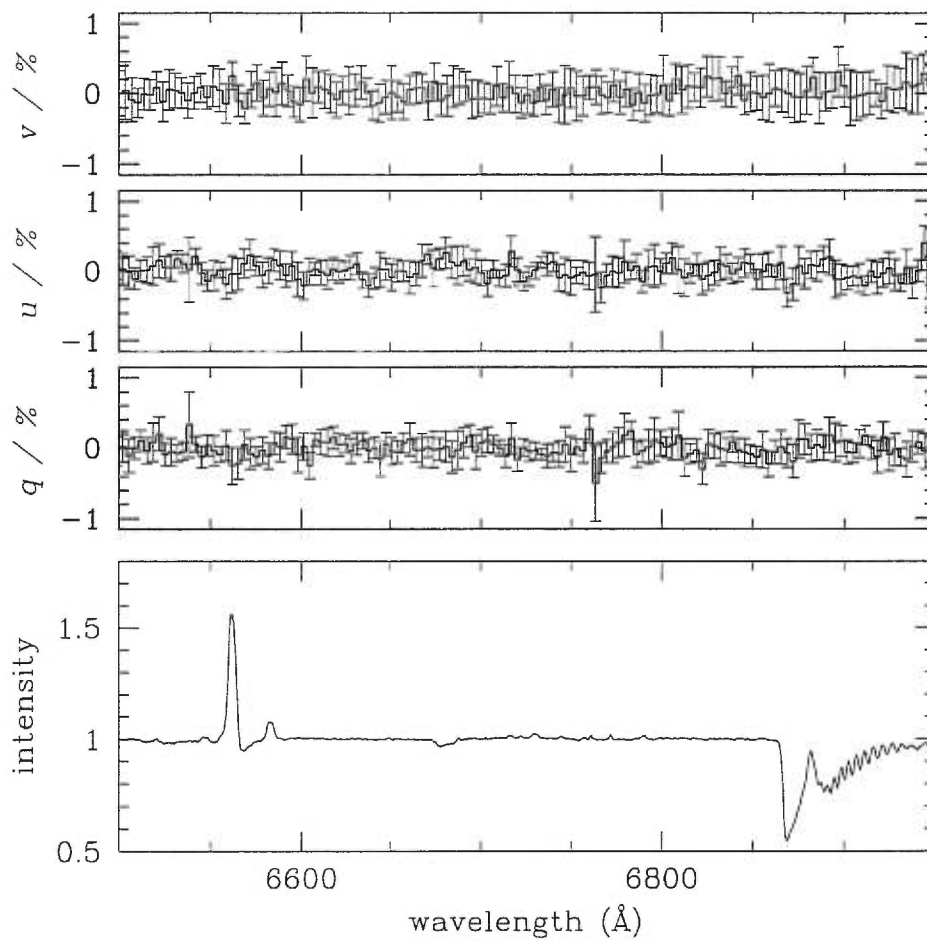
Figure 2.11. Mean rectified intensity spectrum including Hα, and mean Stokes q, u and v for θ^1 Ori C. 2σ errorbars are indicated for bins of 5 pixels.

graph, is able to measure all four Stokes parameters as a function of wavelength in a quasi-simultaneous manner. The combination of two independently rotatable quarter-wave plates with a Wollaston polarizer as beamsplitter creates a double beam which contains all polarimetric information about the stellar target. An extraction technique is devised that leads to spectra in q, u and v, whose precision is limited only by stochastic photon noise (Poisson errors), whereas intensity spectra are limited by flat field noise. We also describe different deviations from ideal for the optical elements. We discuss the behavior of "achromatic" QWP's with respect to chromatism and rotation position, as well as limitations in the use of optical fibers.

During three extended runs at two different telescopes we obtained polarimetric spectra for all four Stokes parameters of several hot star prototypes with the new William-Wehlau Spectropolarimeter. Despite some instrumental problems, we see both line linear depolarization due to Thomson scattering and circular polarization due to Zeeman splitting.

1. For the WR+O binary γ^2 Vel we report polarization features across its strong emission lines. Schulte-Ladbeck et al. (1992) showed that this is due either to a flattened WR wind and/or phase-dependent asymmetries between the O-star and the scatterers mainly in the WR wind.

2. We confirm previously measured polarization variations across the Hα emission line of the brightest Be star visible in the sky γ Cas, but with higher precision.

3. We detect a circular polarization feature in Hα in the strong magnetic Ap star 53 Cam.

4. For the bright Trapezium star θ^1 Ori C we fail to find any polarization feature in Hα at the 0.2% level. Future attempts will have to improve on this precision and secure better phase coverage.

These results establish the William-Wehlau spectropolarimeter as a viable new instrument for measuring all wavelength dependent Stokes parameters of stars. Some improvements will be attempted, e.g., better QWP's, dielectric aperture, and more stable illumination of the fibers. Future preference will be given to large telescopes, because of the small amount of polarization in stellar objects.

2.8 Acknowledgements

T.E., A.F.J.M., M.D., J.B.R, N.P. and P.B. wish to note that the original principal investigator for this instrument, William H. Wehlau, unfortunately passed away in February 1995 while attending a scientific meeting in Cape Town, S.A. We wish to express our deepest respect for his high level of competence and leadership during the planning and early construction stages of the spectropo-

Figure 2.12. WILLIAM H. WEHLAU (1926 - 1995)

larimeter that now carries his name.

References

Babel, J., Montmerle, T. 1997, ApJ, 485, L29

Bailey 1989, in The AAT User's Manual No. 24

Borra, E.F., Landstreet, J.D. 1977, ApJ, 212, 141

Borra, E.F., Landstreet, J.D. 1980, ApJS, 42, 421

Cohen, M.H. 1996, "The LRIS Polarimeter" in: Keck User's Manual

Conti, P.S. 1972, ApJ, 174, L79

Donati J.-F., Semel M., Carter B.D., Rees D.E., Cameron A.C. 1997, MNRAS, 291, 658

Eversberg, T. 1996, *"Spectropolarimetry: A New Window for Stellar Physics"*, Pre-Doctorate Thesis, Université de Montréal, in: The Hot Star Newsletter, No.33

Gagné, M., Caillault, J.-P., Stauffer, J.R., Linsky, J.L. 1997, ApJ, 478, L87

Goodrich, R.W., Cohen, M.H., Putney, A. 1995, PASP, 107, 179

Hanuschik, R.W. 1996, A&A, 308, 170

Harries, T.J. 1995, "Spectropolarimetry as a Probe of Stellar Winds", Ph.D. thesis, University College London

Landstreet, J.D. 1988, ApJ, 326, 967

Martin, P.G., Campbell, B. 1976, ApJ 208, 727

Mathys, G., Stenflo, J.O. 1986, A&A, 168, 184

Miller, J.S., Robinson, L.B., Goodrich, R.W. 1988, in: *Instrumentation for Ground-based Astronomy*, ed. L.B. Robinson (New York: Springer), 157

Moffat, A.F.J., Piirola, V. 1994, ApJ, 413, 724

Poeckert, R., Marlborough, J.M. 1977, ApJ, 218, 220

Schmidt, G.D. 1988, in: G.V. Coyne, A.M. Magalães, A.F.J. Moffat, R.E. Schulte-Ladbeck, S. Tapia, D.T. Wickramasinghe (eds), *Polarized Radiation of Circumstellar Origin*, Vatican Observatory, p. 85

Schmutz, W., Schweickhardt, J., Stahl, O., Wolf, B., Dumm, T., Gäng, T., Jankovics, I., Kaufer, A., Lehmann, H., Mandel, H., Peitz, J., Rivinius, Th. 1997, A&A, 328, 219

Schulte-Ladbeck, R.E., Meade, M., Hillier, D.J. 1992, in: L. Drissen, C. Leitherer, A. Nota (eds), *Nonisotropic and Variable Outflow from Stars*, ASP Conference Series, Vol. 22, p. 118

Serkowski, K. 1962, in: *Advances in Astronomy and Astrophysics*, 1, 247

Serkowski, K. 1974, in: *Methods of Exp. Phys.*, Vol.12, Chap.8

Serkowski, K., Mathewson, D. L., Ford, V. L. 1975, ApJ, 196, 261

Smith, M. 1998, ApJ, in press

Stahl,O., Wolf,B., Gäng, Th., Gummersbach, C.A., Kaufer,A., Kovacs,J., Mandel,H., Szeifert,Th. 1993, A&A, 274, L29

St-Louis, Drissen, L., Moffat, A.F.J., Bastien, P. 1987, ApJ, 322, 870

St-Louis, Moffat, A.F.J., Drissen, L.,Bastien, P., Robert, C. 1988, ApJ, 330, 286

St-Louis, N., Willis, A.J., Stevens, I.R. 1993, ApJ, 415, 298

Tinbergen, J., Rutten, R 1992, The WWH User's Manual

Vats, V. 1997, Karl Lambrecht Corp., Chicago, private communication

Walborn, N.R. 1981, ApJ, 243, L37

Walborn, N.R., Panek, R.J. 1984, ApJ, 286, 718

Walborn, N.R., Nichols, J.S. 1994, ApJ, 425, L29

Chapter 3

Spectropolarimetry of the WR+O Binary γ^2 Velorum During Periastron Passage

THOMAS EVERSBERG[1], ANTHONY F.J. MOFFAT[1,2]
AND SERGEY V. MARCHENKO

Département de Physique, Université de Montréal, C.P.6128, Succ. Centre Ville,
Montréal H3C 3J7, Canada, and Observatoire du Mont Mégantic

3.1 Abstract

We present low resolution ($\sim 6\,\text{Å}$), high signal-to noise spectropolarimetric observations obtained with the new William-Wehlau spectropolarimeter for the apparently brightest Wolf-Rayet star in the sky, the 78.5 d WR+O binary γ^2 Velorum. Quasi-simultaneous monitoring of all four Stokes parameters $I(\lambda)$, $q(\lambda)$, $u(\lambda)$ and $v(\lambda)$ was carried out over an interval of 31 nights centered on periastron. All emission lines in our observed wavelength interval (5200 – 6000 Å)

---

[1]Visiting Astronomer, University of Toronto Southern Observatory, Las Campanas

[2]Killam Research Fellow of the Canada Council for the Arts

show highly stochastic variations over the whole run. The phase-dependent behavior of the excess emission in the C III $\lambda\,5696$ line can be related to the wind-wind collision phenomenon.

Varying features of Stokes q and u are seen across the strong lines, probably as a result of variable electron scattering of mainly continuum light. The spherical symmetry of the WR wind is thus broken by the presence of the O companion and clumping in the WR wind. Similar features in the extended red wing of the C III $\lambda\,5696$ emission line remain unexplained. No obvious circular line polarization features are seen across any emission line above the $3\sigma \sim 0.03\%$ instrumental level.

3.2 Introduction

γ^2 Velorum (WR11 = HR 3207 = HD 68273: WC8+O9I) is the apparently brightest WR star in the sky. It is a nearby binary system ($d = 258^{+41}_{-31}$ pc: Schaerer et al. 1997; van der Hucht et al. 1997) with an orbital period of 78.53 days (Schmutz et al. 1997, who also give a complete description of the orbit), and has the potential to represent a prototype of wind – wind interaction for massive stars with strong winds. Between the two stars the winds come to a complete stop at the stagnation point and material flows along a shock-cone that wraps around the weaker-wind O star (e.g., Stevens et al. 1992). The shock region, due to collision at supersonic wind velocities, creates highly excited material that leads to excess emission via fast radiative cooling of the shocked gas (e.g., St.-Louis et al. 1993). Bartzakos (1998) used modified minimum spectra of the C III $\lambda\,5696$ line to estimate the collision excess in a number of short-period (2 – 16 day) WC+O binaries. For γ^2 Vel, such a method has been slow in coming, probably because of its inconveniently long orbit and presence of short-term stochastic multi-scale structures in the C III $\lambda\,5696$ line of γ^2 Vel (Lépine, Eversberg & Moffat 1999). It was only after completing this project that we became aware of the spectroscopic

study of Schweickhardt et al. (1999).

In this paper we concentrate on: (1) search for periodic line profile variations, following the contradictory reports of Jeffers, Stiff & Weller (1985 and references therein) and Taylor (1990); (2) behaviour of the C III $\lambda\,5696$ line during periastron passage, in the anticipation that for WC stars this particular line should be the best indicator of a wind-wind collision in the optical (Bartzakos 1998); (3) search for any manifestation of a magnetic field and deviations from spherical symmetry in the WR wind.

The relatively long orbital period remains a practical handicap for a better understanding of γ^2 Velorum. For this reason we have attempted to answer some of these questions by observing prominent emission lines mainly around periastron passage, when the orbital configuration changes fastest.

3.3   Observations and data reduction

γ^2 Velorum was observed during a five week run in Feb/March 1997 with the William-Wehlau spectropolarimeter mounted on the 0.6m telescope at the University of Toronto Southern Observatory (UTSO) on Las Campanas, Chile. We obtained spectra in all four wavelength-dependent Stokes parameters I, $\frac{Q}{I} \equiv q$, $\frac{U}{I} \equiv u$ and $\frac{V}{I} \equiv v$ during 21 nights between Feb 18 and March 20 within $\Delta\phi \sim \pm 0.2$ of periastron passage ($\phi = 0.00$; O star in front at $\phi = 0.03$; WR star in front at $\phi = 0.61$). Individual spectra in I were obtained every ~ 3 minutes, providing a typical $S/N \sim 400/pix$ in the continuum (~ 600 in the strong CIII $\lambda\,5696$, CIV $\lambda\,5806$ emission lines). Using the Garrison spectrograph (Garrison & Beattie 1990), the 3-pixel spectral resolution was about $6\,\text{Å}$ (~ 320 km/s) in the wavelength range $5200 - 6000\,\text{Å}$, covering mainly the He II $\lambda\,5411$, C IV $\lambda\,5471$, C III $\lambda\,5696$, C IV $\lambda\,5802/12$ and He I $\lambda\,5875$ emission lines. Unfortunately, the data for nine nights (Feb 22 – March 2) are of no use due to problems discovered

later with the CCD readout.

As a consequence of non-perfect behavior (as predictable for a fiber-fed system) of the polarimeter unit (see Eversberg et al. 1998b, who also give a detailed description of the data calibration procedure) we had to normalize the mean Stokes parameters $q(\lambda)$, $u(\lambda)$ and $v(\lambda)$ to zero, so that only relative line polarization could be obtained. This means that we were not able to estimate the degree and orientation of *broadband* polarization on the sky. Only relative line polarization and its variability were detectable.

3.4 Results and Discussion

With our insufficient orbital coverage and low spectral resolution we do not attempt to improve the orbital parameters. However, as a quick check we measured the central wavelengths of all prominent WR emission lines by fitting a single Gaussian profile.

Our velocity measurements for C IV $\lambda 5471$ match best the predicted emission line orbit (Schmutz et al. 1997). This is not surprising because this line is most Gaussian-like in form, unblended and well isolated. C IV $\lambda 5802/12$ also fits fairly well, although this line is not of pure Gaussian form and is blended. All other moderately strong emission lines tend to follow the general shape of the orbital motion, but with increased amplitude. This increase is especially evident in He I $\lambda 5875$ and, to a lesser extent, in C III $\lambda 5696$ emission. This is primarily caused by the additional emission component changing its position on top of the underlying broad emission line as the stars go through periastron (see below).

95

3.4.1 Stochastic short term variations

After co-adding all nightly spectra to yield a mean for each night and Doppler correcting them into the WR rest-frame using the Schmutz et al. orbit, we co-added all nightly means to a global mean of the whole run. This global mean was then subtracted from the individual spectra in the WR frame, thus allowing us to study short-term (∼hourly) variations. The resulting grey-scale plots of these residuals and the global mean are shown in Figs. 3.1 – 3.3, for three consecutive intervals in orbital phase.

In order to explore the global variability we calculate the standard deviation of pixel i:

$$\sigma_i = \sqrt{\frac{1}{n-1}\sum_{j=1}^{n}(I_{ij} - \bar{I}_i)^2} \quad , \tag{3.1}$$

where I_{ij} is the rectified intensity of pixel i of the jth spectrum and $\bar{I}_i$ is the global mean spectrum at pixel i. The results are shown in Fig. 3.4 (bottom). Inspection of Figs. 3.1 – 3.3 allows us to conclude:

1. C III λ 5696 – The most prominent nightly residuals are found in this line, which is already known to show stochastically emerging subpeaks with gradual motion away from the line center (Lépine, Eversberg & Moffat 1999: 2-night high-resolution observations around phase $\phi = 0.26 - 0.29$). Though our data are of lower resolution, we can confirm this kind of *stochastic* variability over a much longer time-scale and far broader phase coverage. The movement of these subpeak features is well established in WR stars (e.g., Lépine 1998; Lépine & Moffat 1999) as well as in the O supergiant ζ Puppis (Eversberg, Lépine & Moffat 1998a) and interpreted as due to regions of higher density moving radially outwards from the star and seen in projection in the line of sight.

2. C IV λ 5802/12 – In accordance with the idea of wind stratification (Kuhi 1973; Schulte-Ladbeck et al. 1995, and references therein), C IV λ 5802/12 is as-
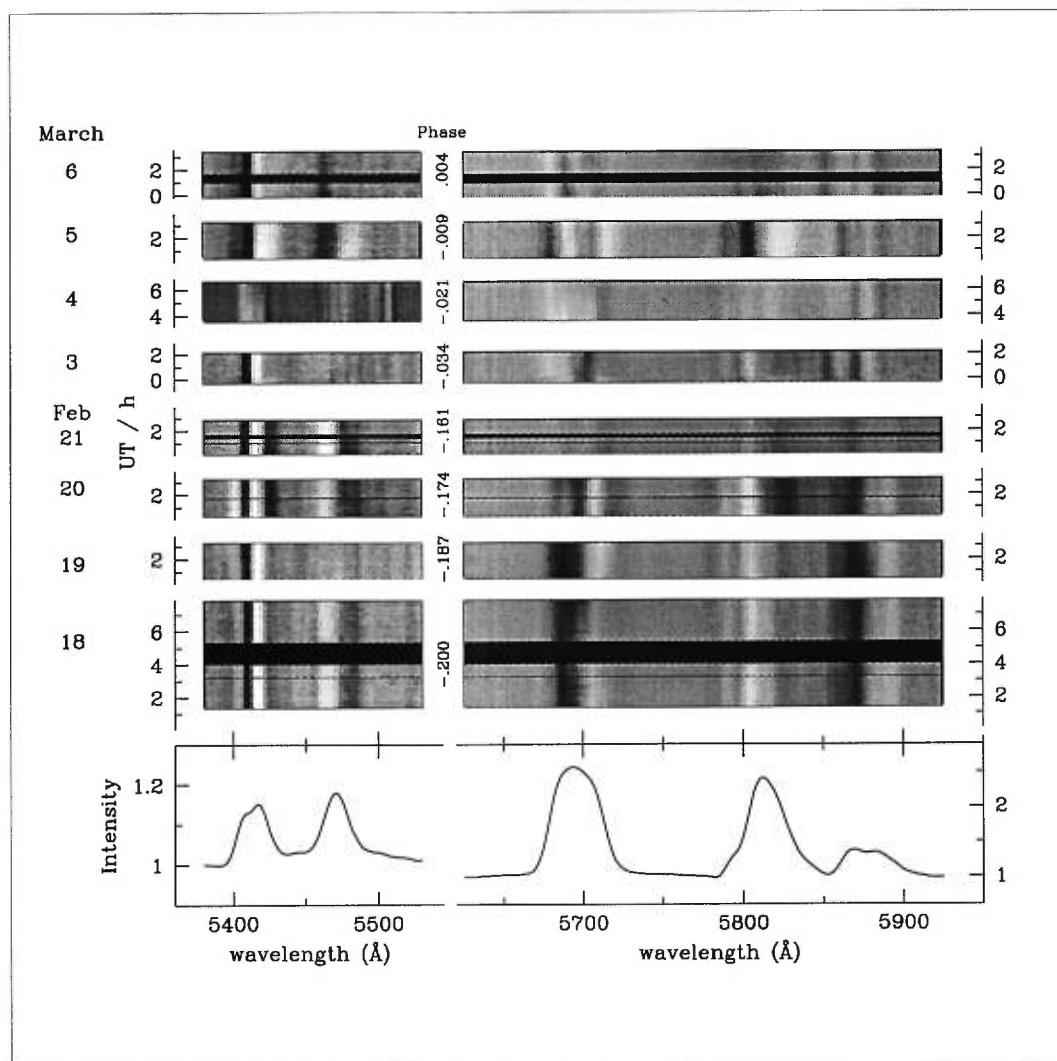
Figure 3.1. Observed spectra of γ^2 Vel shifted to the WR frame for the nights of 1997 Feb 17/18 to March 5/6. **Top:** Greyscale plots of residuals from the mean rectified spectrum of the whole observing run plotted in time (stretched appropriately to fill in small time gaps) vs. wavelength. The greyscale range is $z = 0 \pm 0.1$ for the wavelengths $\lambda\lambda$ 5380 – 5530 Å (left) and $z = 0 \pm 0.2$ for the wavelengths 5620 – 5920 Å (right), z being the residual in continuum units. Different phases and respective UT dates and times are indicated. **Bottom:** Global (whole run) mean spectrum in the WR frame.
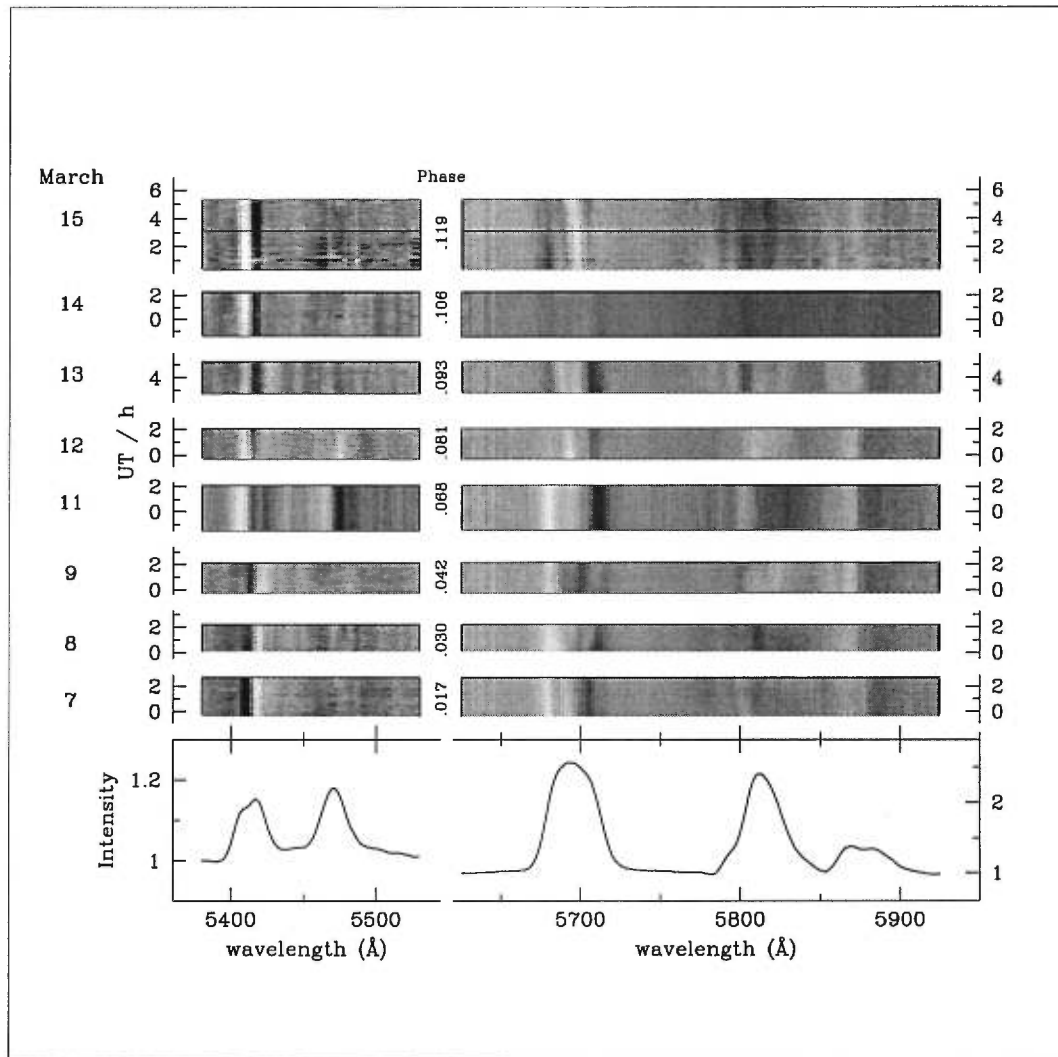
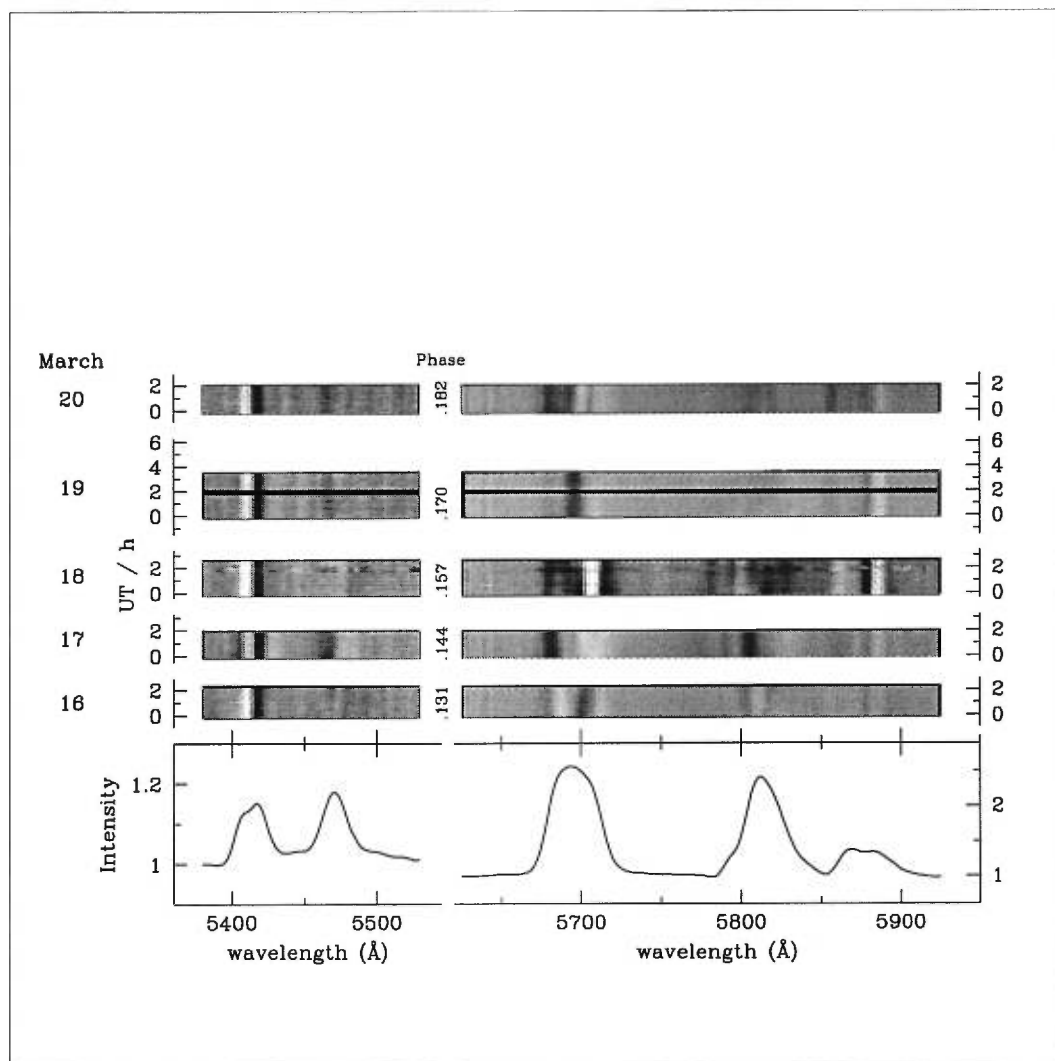Figure 3.2. Same as Fig. 3.1 but for the nights 1997 March 6/7 to 14/15.

Figure 3.3. Same as Fig. 3.1 but for the nights 1997 March 15/16 to 19/20.

sumed to be formed closer to the WR star than C III λ 5696. One might expect to detect stochastic variability in C IV λ 5802/12 if the *whole* wind is structured. The variations are indeed detectable in C IV , but slightly smaller than in C III (Fig. 3.4). We find no clear correlation between the deviations in C III λ 5696 and C IV λ 5802/12, partly because of the blended nature of the C IV line.

3. All the other three major observed emission lines are weaker and the variability is sometimes close to the limit of detectability with our low spectral resolution. The two Helium lines He II λ 5411 and He I λ 5875 are also affected by absorption of the O star component. This absorption is easily detected in He II λ 5411, crossing the emission from blue to red during our run, in agreement with the predicted orbit. For He I λ 5875 the O-component absorption is much less clear. A stochastic component of variability seems to dominate in this line, being loosely correlated with the variations in the C III λ 5696 line. Variability in the C IV λ 5471 line is also detectable but without sufficient quality to draw quantitative conclusions. Allowing for statistical fluctuations, the variation profile across the line, $\sigma(\lambda)$ (Fig. 3.4, bottom), roughly follows the same basic shape of the line profile $I(\lambda)$ itself, with $\frac{\sigma(\lambda)}{I(\lambda)-I_c} \sim 5$ % for C III λ 5696, $\sim 4\%$ for C IV λ 5802/12, ~ 10 % for He II λ 5411 and He I λ 5875, and ~ 3 % for C IV λ 5471.

3.4.2 Periodic short-term variations

Do the observed emission lines show *periodic* variations on short time-scales?

There are numerous, though controversial reports about short-term variability in the spectrum of γ^2Vel, summarized in Jeffers, Stiff & Weller (1985): the profiles (or the line flux measured in the narrow-band filters centered on prominent emission lines) show rapid, sometimes periodic variations on a typical time scale of 150-200 sec. Far longer, P=1.26 h and/or P=2.0 h, coherent variations were discovered by Taylor (1990) in extensive narrow-band photometric

data (HeII 4686 line and adjacent continuum) obtained at the South Pole.

Our data set allows us to search for periodic line profile variations in the relatively broad range, 6 min $\leq$ P $\leq$ 15d, on the high-quality spectra taken every $\sim$3 min over a typical interval of 2 – 3 hours in each of 21 nights during the 31d run. Visual inspection of the individual spectra shows no apparent short-term ($\sim$minutes) variability. However, the spectra do vary on a much longer ($\sim$hours) time scale.

In order to search for a periodic component in the line profile variations, we have calculated power spectra (PS) using the technique of Scargle (1982). The raw PS were then reprocessed with the CLEAN algorithm in order to remove (reduce) the aliases and spurious features introduced by the unevenly spaced nature of the data (see Roberts, Lehár, & Dreher 1987). The calculations were performed for each wavelength pixel, using intensity readings in the spectra rebinned in a similar manner and Doppler corrected for orbital motion to the WR frame.

We started by analyzing individual nights, each consisting of 40-73 spectra. From here on we refer to the results obtained for the C III λ 5696 Å emission line only (CIV λ 5802/12 behaves similarly). We find no significant, periodic variations in the CLEANed PS over the $(50-75)\,d^{-1} \leq \nu \leq 250\,d^{-1}$ frequency domain, with amplitudes exceeding the 3σ level of $\sim$15% of the line intensity. The nightly PS show some rise, roughly as ν^{-1}, toward lower frequences, $\nu \leq (50-75)\,d^{-1}$, with typically 3-5 broad peaks slightly exceeding the 3σ level. We disregard these details as true indicators of periodic variations for two reasons: 1) the low-frequency structures are practically never repeated in consecutive nightly PS; 2) far more important, the peak structure is mimicked by the adjacent continuum. We know that the continuum is not involved in any *periodic* short-term activity (Taylor 1990). Thus, we interpret these low-frequency features as low-amplitude remnants of imperfectly CLEANed spectral windows, i.e. as artefacts arising from the uneven data sampling and finite lengths of the data records.

With no positive periodic detection in any of the nightly data sets, we combined the observations into blocks of 3 consecutive nights and repeated the analysis. The results are invariably negative, with no periods of A $> 3\sigma$ ($\sim$6% of the line intensity) for $(50 - 75)\,d^{-1} \leq \nu \leq 250\,d^{-1}$. There is some rise in the PS toward lower frequences, $\nu \leq (50 - 75)\,d^{-1}$, with broad peaks superposed on the $\sim \nu^{-1}$ sloped PS. Even larger blocks of $\sim$week intervals bring the detectability limit down to $A \leq 3\%$ of the line intensity, with no significant periodicity. The last step is to analyse the complete data set. For this we averaged the spectra of a given night into (2-5) group averages (depending on the level of variability and the number of spectra for the given night) and calculated the PS for the resulting 54 group means. Again, there is no indication of significant periodicity in the $0.07\,d^{-1} \leq \nu \leq 10\,d^{-1}$ frequency interval.

The only positive result we can infer from this exhaustive search is the $\sim \nu^{-1}$ rise in the low-frequency part of the PS, probably indicating that we have detected aperiodic variations on timescales of $\Delta t \geq 0.5$h.

3.4.3 Long-term variations

To monitor the phase-locked, long-term WR line variability through periastron passage, we created nightly mean residuals, plotting them in Fig. 3.4.

Significant long-term variations occur across the lines. All major lines but He II λ 5411 show some excess variability on their blue flanks. This is not explainable by purely stochastic variability due to uniformly distributed clumps in a spherically symmetric wind, but can be related to binary-induced effects (see sect. 3.4.4). The strong variations in the He II line are mainly due to the O star absorption feature, clearly detected as moving across the line during our run and producing symmetric peaks in $\sigma(\lambda)$ in Fig. 3.4.

In Fig. 3.5 we show the measured nightly-averaged equivalent widths, W_λ, for
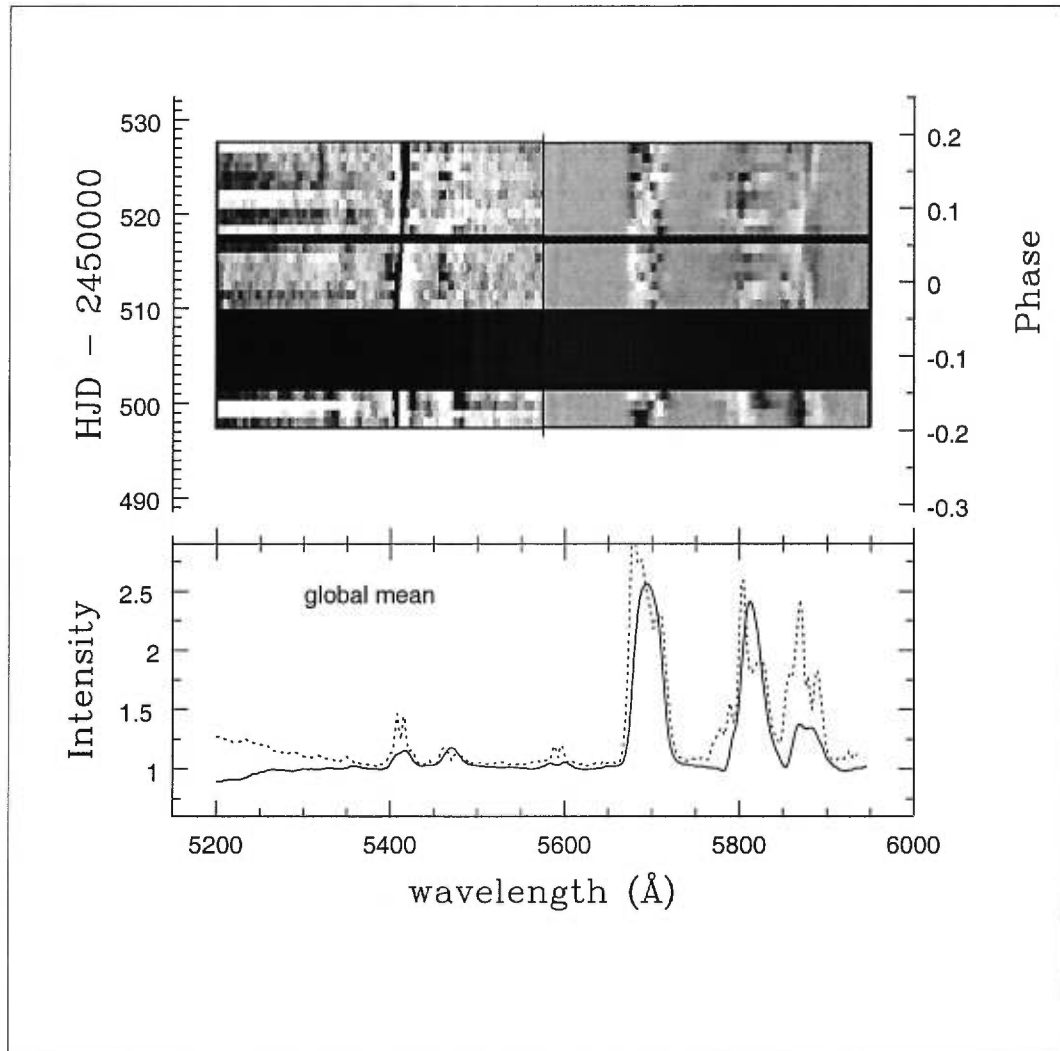
Figure 3.4. Long-term line variability. **Bottom:** Mean rectified spectrum (solid) and standard deviation σ (dashed) for the whole observing run in the WR frame. The σ profile is expanded by a factor 20 and shifted by 1 in intensity, to match the mean rectified line profile as closely as possible. **Top:** Greyscale plot of residuals from the global mean rectified spectrum of each night plotted in time (stretched appropriately to fill in time gaps) vs. wavelength. The spectra have been Doppler corrected into the WR rest-frame by using the orbit determined by Schmutz et al. (1997). The greyscale range is z= 0 ±0.1 for the wavelength interval 5200 – 5575 Å and z= 0 ±0.2 for 5575 – 5950 Å.

the five prominent emission lines, corrected for the phase-dependent continuum variations of Marchenko et al. (1998b).

As one can see, the C III $\lambda 5696$ and He I $\lambda 5875$ line fluxes slightly increase before and then decrease after periastron passage with a maximum around closest approach, as was previously observed in C III $\lambda 5696$ by St-Louis (1996). In contrast to C III and He I , the three other lines, all of higher ionization level, show no significant dependence on orbital phase. Additionally, there are large stochastic equivalent width variations in all prominent emission lines far exceeding the measurement errors. The phase-dependent changes in the C III $\lambda 5696$ and He I $\lambda 5875$ fluxes roughly follow a $1/r$ dependence, where r is the orbital separation, as expected for the excess emission formed in the wind-wind collision zone (Stevens et al. 1992)

3.4.4 C III excess

Although both He I $\lambda 5875$ and C III $\lambda 5696$ reveal similar phase-dependent long-term variations, here we concentrate on C III , since it is stronger and less blended than He I . The C III $\lambda 5696$ line is assumed to consist, in principal, of four different components: (a) emission from a constant, presumably spherically symmetric WR outflow (see below), (b) stochastic sub-features due to clumping in the WR wind (Lépine et al. 1998), (c) phase-dependent excess emission created by colliding wind in a shock cone around the O star and (d) heating of the WR wind by the O star. Effect (d) is seen even in some binaries with relatively large separation, e.g., the 21 day WN5+O binary WR 141 (Marchenko et al. 1998a). We do not consider WR atmospheric eclipses, as such are proved to be important in γ^2 Vel (Schweickhardt et al. 1999) only around phases when the WR star is in front; these phases are not covered by our observations.

Disentangling these four components is a delicate problem, though success-
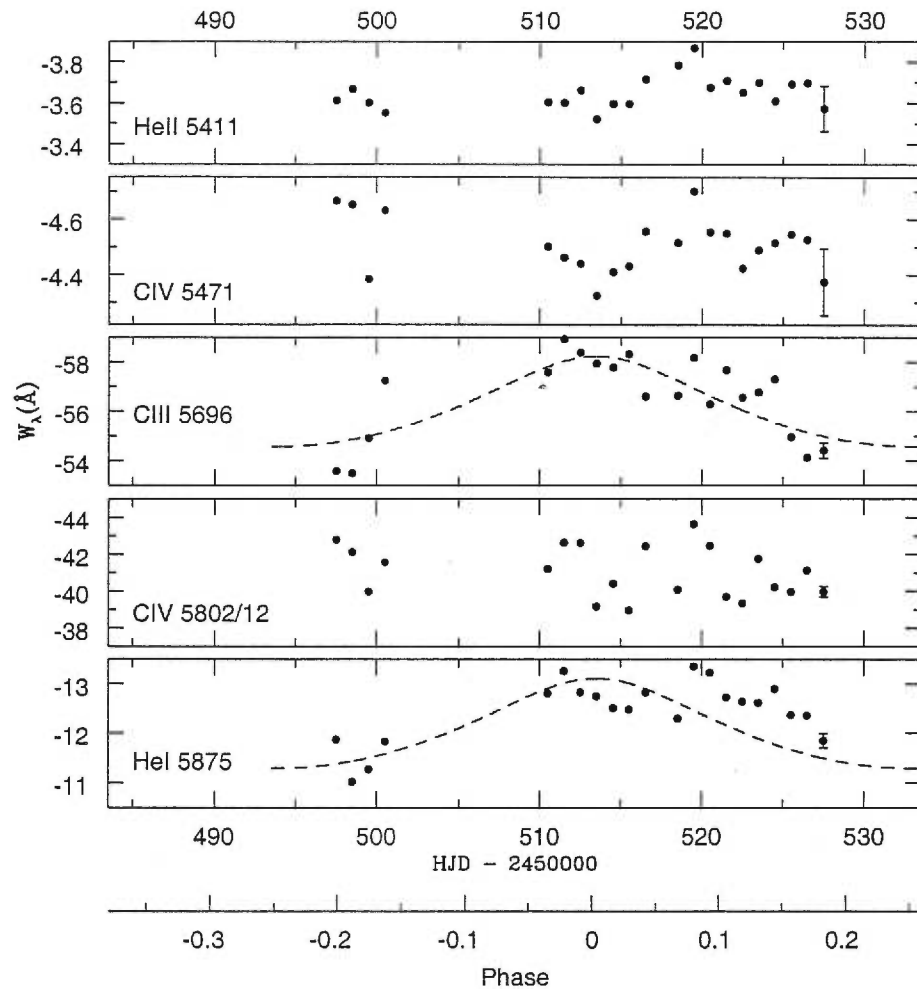
Figure 3.5. Equivalent widths of the nightly average emission lines, corrected for the phase-dependent continuum variations (Marchenko et al. 1998b). The typical 2σ errors estimated in accordance with Chalabaev & Maillard (1983) are indicated on the last data point of each plot. Dashed lines represent the relative inverse separation (arbitrary scale and zero point) between the two binary components.

fully done for (a) and (c) in several WR+O binaries (e.g., Marchenko et al. 1997; Moffat et al. 1998; Moffat, Marchenko & Bartzakos 1996; Bartzakos 1998; Bartzakos, Moffat & Niemela 1995). We have tried to distinguish between the excess emission and the globally spherically symmetric (however, locally clumpy) outflow under the following assumptions:

1. Emission arising from sources (c) and (d) is expected to be separation dependent, being weakest at apastron. This is indeed seen for γ^2 Vel in Fig. 3.5 as well as in the data of Schweickhardt et al. (1999). In this case the *minimum* spectrum in the WR frame over an extended observing run for a highly elliptical binary might represent the spherically symmetric WR outflow fairly well.

2. In the present data set, the largest projected separation between the two components occurs at $\phi = \pm 0.2$. In a zeroth approximation we use the actual minimum profile of the whole run as a representation (in reality an upper limit) of the spherical wind. We use this on γ^2 Vel to test the shock-cone model developed by Lührs (1991, 1997).

Following this recipe, we Doppler corrected all the spectra of γ^2 Vel into the WR rest-frame and derived a global *minimum* spectrum. This minimum spectrum was then subtracted from the nightly mean spectra to obtain nightly excess emission spectra. The resulting grey-scale plot, the global minimum, mean and maximum spectra of the whole run for the wavelength interval 5640 – 5940 Å are shown in Fig. 3.6.

As one can clearly see in Fig. 3.6, excess emission above the minimum in C III λ 5696 and, less clearly, He I λ 5875 is phase dependent. This feature moves from the red to the blue line flank and back during the run. This excess emission causes large deviations in the RV curves of He I λ 5875 and C III λ 5696 from the 'normal' orbital motion, as mentioned above.

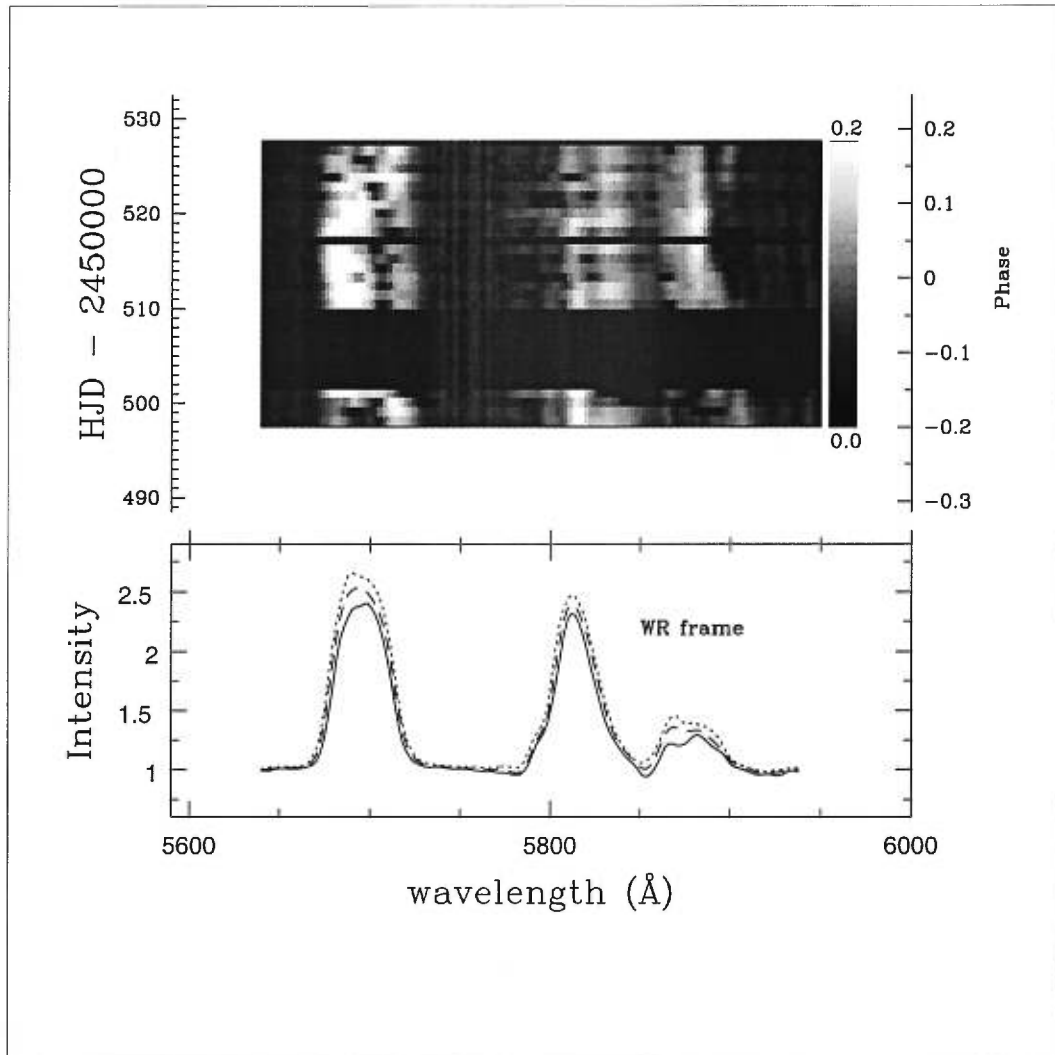Lührs (1991, 1997) has developed a simple model to describe the phase-

Figure 3.6. Nightly excess emission spectra above the minimum level. **Bottom:** Global minimum (solid), mean (dashed) and maximum (dotted) profile for the whole observing run in the WR frame. **Top:** Greyscale plot of residuals from the global minimum spectrum of each night plotted in time (stretched appropriately to fill in time gaps) vs. wavelength. The spectra have been Doppler corrected to the WR frame by using the orbit determined by Schmutz et al. (1997). The greyscale ranges over z= 0 – 0.2, as indicated on the right.

dependent variations of the excess emission in WR+O binaries with *circular* orbits. Assuming optically thin emission from a hot plasma wrapping around the O star component and moving with velocity v_s along a cone with opening half-angle Θ, deflected in the orbital plane by an angle $\delta\phi$ due to the Coriolis effect associated with orbital motion, one finds (cf. also Moffat et al. 1998) that the double-peak excess emission from the cone has an average velocity $\bar{v}$ and peak-to-peak width $2v_\star$, of:

$$\bar{v} = v_s \cos\Theta \sin i \cos(\phi - \delta\phi) \tag{3.2}$$

and

$$2v_\star = 2v_s \sin\Theta\sqrt{1 - \sin^2 i \cos^2(\phi - \delta\phi)}, \tag{3.3}$$

with ϕ the orbital phase $\in \{0, 2\pi\}$ and i the inclination. For the analysis of γ^2 Vel with an eccentric orbit we follow Moffat et al. (1998), by replacing ϕ by $w + \omega - \pi/2$ and $\delta\phi$ by δw, with w the true anomaly and ω the usual periastron angle:

$$\bar{v} = v_s \cos\Theta \cos(w + \omega - \delta w - \pi/2) \tag{3.4}$$

and

$$2v_\star = 2v_s \sin\Theta\sqrt{1 - \sin^2 i \cos^2(w + \omega - \delta w - \pi/2)}. \tag{3.5}$$

In our situation with the high intrinsic noise level of the variations and the uncertainty in the appropriate template profile to extract the excess emission, $\bar{v}$ and $2v_\star$ are not clearly defined. For this reason we calculated a more robust value of a weighted average LOS velocity $\bar{v}$ with

$$\bar{v} = \frac{\sum_i I_i \cdot v_i}{\sum_i I_i} \tag{3.6}$$

and a weighted average width 2σ to characterize the peak separation, adding a

constant $2v_c$:

$$2v_\star \to 2\sigma + 2v_c = 2\sqrt{\frac{\sum_i I_i \cdot (v_i - \bar{v})^2}{\sum_i I_i}} + 2v_c, \tag{3.7}$$

with v_i the LOS velocity and I_i the residual line intensity at pixel i. The newly introduced constant $2v_c$ reflects the fact that the bow-shock emission is likely to be significantly broadened due to large-scale turbulence (Walder & Folini 1998) in the wind-wind collision zone.

To test our procedure we also created a true minimum and various smoothed (boxcar of 3, 5, 7 and 9 pixel) minimum spectra from the γ^2 Vel data and a minimum template from the smoothed C III line of WR 135 (data from Lépine & Moffat 1999). The latter template was produced by normalizing the C III line of WR 135 in height and width to C III in γ^2 Vel via simple comparison of its lower, less variable part. Note that WR 135 has the same subtype and even wind terminal velocity as the WR component in γ^2 Velorum. Smoothing of the minimum spectra of γ^2 Vel does not significantly change the output results. However, the WR 135 template was found to be unsatisfactory, due to the subtle differences in the uppermost parts of the profiles. Thus, we retain the true minimum (no smoothing) profile of γ^2 Vel in our modeling (Fig. 3.7).

As we face the serious problem of the unknown true minimum spectrum, with the additional complication from the presence of large stochastic line variations, we are not able to perform a quantitatively meaningful multi-parametric fit to find the values of v_c, v_s, θ, δw and i. Instead, whenever possible, we use known or otherwise reasonable values, for these parameters.

The short-dashed and long-dashed lines in Fig. 3.7 show the predictions of the Lührs model for two values of δw. Willis et al. (1995) estimated $\Theta \sim 25°$ from their ROSAT X-ray observations. In fact, the opening angle might be at least a factor of 2 larger, judging by the appearance of the O-star high-velocity absorption ~ 0.09 in phase *before* periastron passage (St-Louis et al. 1993). Also, the revised $\dot{M}$ of the WR star ($\dot{M} = 0.7 - 3.0 \times 10^{-5}$: Schmutz et al. 1997; Schaerer et al.
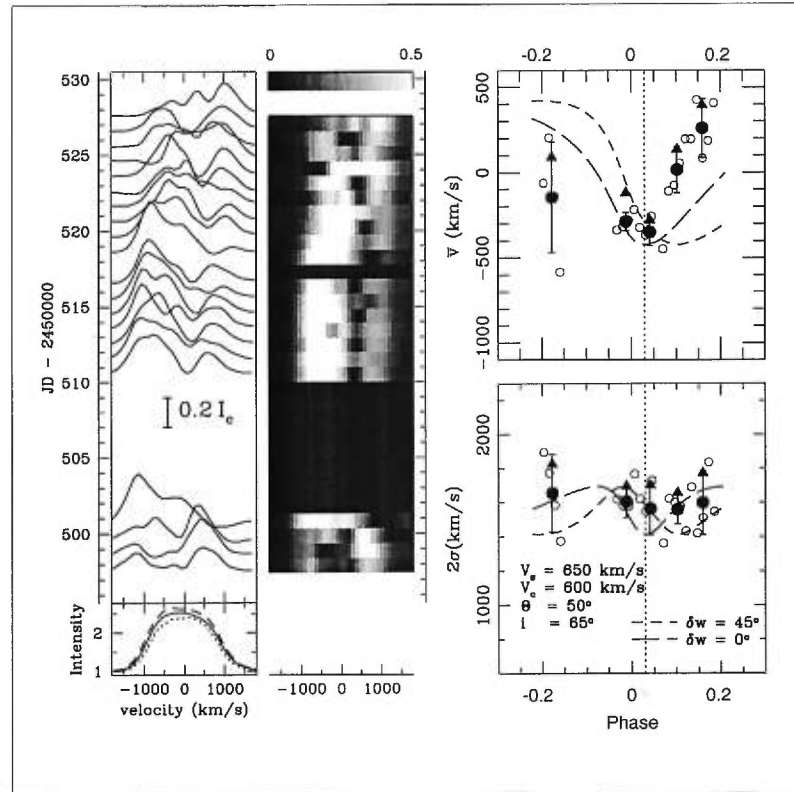
Figure 3.7. Extracted C III $\lambda\,5696$ excess emission spectra of γ^2 Vel for different orbital positions in the observer's frame. **Left, Top:** Intensity plot of nightly residuals from the minimum spectrum of the whole observing run plotted in time vs. LOS velocity. **Left, Bottom:** Global maximum (long-dash), mean (solid) and minimum (dotted) line profile of C III $\lambda\,5696$. **Center:** Greyscale plot of nightly residuals from the minimum line profile plotted in time (stretched appropriately to fill in time gaps) vs. line-of-sight velocity. The greyscale range is z= 0 – 0.2. **Right:** Comparison of the observed average velocities (**top**) and line widths (**bottom**) of the excess emission with the Lührs model. Open circles: Excess using the global minimum for each night. Filled circles: Average excess emission of 4-night bins (2σ errorbars are indicated). Filled triangles: Average excess emission of 4-night bins including back scattered light. The vertical dotted lines indicate the position when the O star is in front of the WR component. The short-dashed curves represent the theoretical calculation using Lührs' model with $\delta\omega = 45°$; the long-dashed curves for $\delta\omega = 0°$.

1997; Nugis et al. 1998) leads to $\Theta = 45° - 68°$, using the formalism from Usov & Eichler (1993) and Canto, Raga & Wilkin (1996). The latter value of Θ must be treated as an upper limit due to reclassification of the O component from O9I to O8III (Schaerer et al. 1997), with potential diminishing of $\dot{M}(O\,star)$. We assume that the Coriolis deflection δw lies somewhere between 0° and 45°, judging by the phase-dependence of the X-ray flux. First, we fix the stream velocity, $v_s = 650$ km/s, the cone-opening half-angle $\Theta = 25°$ (Stevens et al. 1996), $i = 65°$ and two different values of the Coriolis deflection, $\delta w = 0°$ (long-dash) and $\delta w = 45°$ (short-dash). Note that the model is not very sensitive to the choice of i within the proposed range $i = 65° \pm 8°$ (Schmutz et al. 1997). This leaves us with the only unaccounted free parameter $2v_c$. Formally chosen as $2v_c \sim 2\sigma_{turbulent}$ (up to 400 km/s in γ^2 Vel: Lépine et al. 1999) it does not apply in practice to the observational data. Obviously, this parameter is heavily biased by the subtraction of a probably inadequate template. Because of the nature of this bias, we expect $2v_c$ to be somewhere between $2v_{turbulent} \sim 400$ km/s and $2v_{shock} \cong 2300 - 2600$ km/s (twice the velocity of the WR wind entering the wind-wind collision zone – cf. St.Louis et al. 1993). Indeed, we find $2v_c = 1200$ km/s as a reasonable compromise to match the data.

With the above parameters we find that the modeled variations in $\bar{v}$ far exceed the observed amplitude. This can be counteracted by increasing the opening angle Θ. This additionally affects δw, requiring $\delta w \ll 45°$. The possibility of increasing Θ is related to the revised $\dot{M}(WR)$, as mentioned before, and also to the strong wind braking effect (sudden deceleration of the WR wind by the O star radiation just before it enters the bow-shock zone) predicted for this system (Gayley et al. 1997). We therefore change Θ from 25° to 50°, taking this as a tentative estimate. The change brings the calculated $\bar{v}$ much closer to the data.

However, despite the qualitative similarity of the observed and modeled $\bar{v}$ curves, there are large systematic deviations. The first reason for this might be the

unaccounted presence of backscattered light, especially important around periastron passage. We include this process in our model, however rather schematically, approximating the scattered light by a Gaussian profile of fixed central intensity and half-width. We also allow for the Doppler shift of this component in accordance with the orbital motion as well as a $\delta w = 45°$ phase deflection (as an upper limit of the redistributed flux). This deflection is based on the consideration of overheating of the O star surface by the X-ray flux coming from the bow-shock head (cf. Gies et al. 1997).

Inclusion of backscattered light does not remove the disparity between the modeled and observed $\bar{v}$. We have no feasible explanation for these deviations. However, we can conclude that the backscattered light plays a relatively minor role in the observed phase-related line-profile variations. We share this conclusion with St.-Louis et al. (1993). Considering the number of assumptions required to obtain the minimum C III profile, along with the strong profile variations unrelated to the wind-wind collision, our model provides only a qualitative indication that the wind-wind collision is likely at work in this system.

Some support for our results comes from an independent study. Recent analysis of optical line emission and its variability in γ^2 Vel has been carried out by Schweickhardt et al. (1999). By comparing their data from an extended observing run with a model for occultation effects developed by Auer & Koenigsberger (1994), they conclude that the observed line profile variability around periastron passage in C III 4650 (partly blended with C IV 4658) cannot be explained by occultation. They therefore state that the excess C III 4650 emission arises, at least partly, from wind-wind collision in γ^2 Vel.

The most interesting detail readily seen in Fig. 2 of Schweickhardt et al. (1999) is the swift change, by as much as 1000 km/s, of the velocity of the excess emission in C III 4650 at ϕ between -0.15 and -0.10. This is confirmed by our observations in Fig. 3.7, where one sees a ~ 500 km/s jump in $\bar{v}$ for C III $\lambda 5696$ at

$\phi \sim -0.15$. This phenomenon repeats over many orbital cycles; hence, we discard stochastic wind variability as a cause. We note that around periastron passage, the changing wind momentum balance (cf. Gayley et al. 1997) may provoke crashing of the WR wind onto the O star surface. This may significantly change the mass load into the wind-wind collision zone as well as its geometry (phase-variable Θ and reduced δw) and physical conditions, increasing the emissivity from the wind-wind collision component (note the rise in W_λ of He I and C III in Fig. 3.5), thus creating much stronger extra blueshifted emission, and, finally, shifting the WR profile to negative velocities. It is relevant to note that the wind velocity of the O star tends to be lower during periastron passage (Stevens et al. 1996), which might signify an abrupt change in the dynamics of the wind-wind collision process.

Another detail to be mentioned is the pronounced asymmetry between the ingress- egress behavior of the excess emission, suggestive of more gradual lift-off of the shock from the O star surface after the initial swift crushing. This asymmetry is probably created by the orbital motion of the components, in direct analogy to another highly eccentric colliding-wind binary, ι Orionis (Pittard 1998).

Now we are able to explain the excess variability in the blue wing of the Carbon and He I lines in Fig. 3.4. According to the Lührs model with allowance for crashing of the WR wind onto the O star, strong excess emission is expected to shift to the blue when the O-star is $\sim$ in front, i.e., around periastron passage. This introduces larger values for the scatter σ in the blue wing of our data. This is clearly detected in all the five strong emission lines, except He II $\lambda\,5411$, where the excess emission is masked by the strong O star absorption.

3.4.5   Polarization

The shock-cone introduces a deviation from spherical symmetry in the WR wind so that, in principle, it could lead to phase-dependent intrinsic continuum polarization. However, an even more important source of phase-dependent *continuum* polarization is the scatter of O-star light off free electrons in the WR wind (see St-Louis et al. 1987 for γ^2 Vel and other WC+O binaries). On the other hand, *WR emission-line* flux in a binary will be practically unpolarized. This might cause some phase-dependent variations of polarization occurring at the positions of the emission lines (see Moffat & Piirola 1994). In general, a flattened WR wind can also cause some line depolarization (cf. Harries et al. 1998), which however is not expected to vary with phase in a binary system.

To obtain sufficient accuracy in q, u and v we co-added all nightly Stokes parameters, Doppler corrected into the WR rest-frame to global mean Stokes q, u and v spectra normalized to zero for the whole run, consisting of ~ 80 hours of exposure time in total. The result is shown in Fig. 3.8.

We draw attention in Fig. 3.8 to the depressions ($\sim 0.05\%$) in Stokes q and u across the two strong lines of C III λ 5696 and C IV λ 5802/12, significantly above the 3σ noise level, $\sim 0.03\%$. We calculate this precision limit from the featureless $v(\lambda)$ spectrum between 5600 and 5950 Å[1]. The He I λ 5875 line also shows complex structure, although closer to the noise limit. Phase-locked q, u variations in the continuum light, clearly seen around periastron passage in broadband polarization (St-Louis et al. 1987), have probably diluted the line polarization effect due to phase-smearing, which for q and u is expected to be the largest at quadratures. Additionally, any regular variations across the line profiles are masked by omnipresence of the strong stochastic component.

---

[1]We define the noise of pixel i as $\sigma_i/\sqrt{N}$, with the σ_i as defined in eq. (1) and N as the number of rectified polarization spectra. We assume that the $v(\lambda)$ spectrum is entirely noise dominated. The photon statistics and observation technique are *identical* in q, u and v.
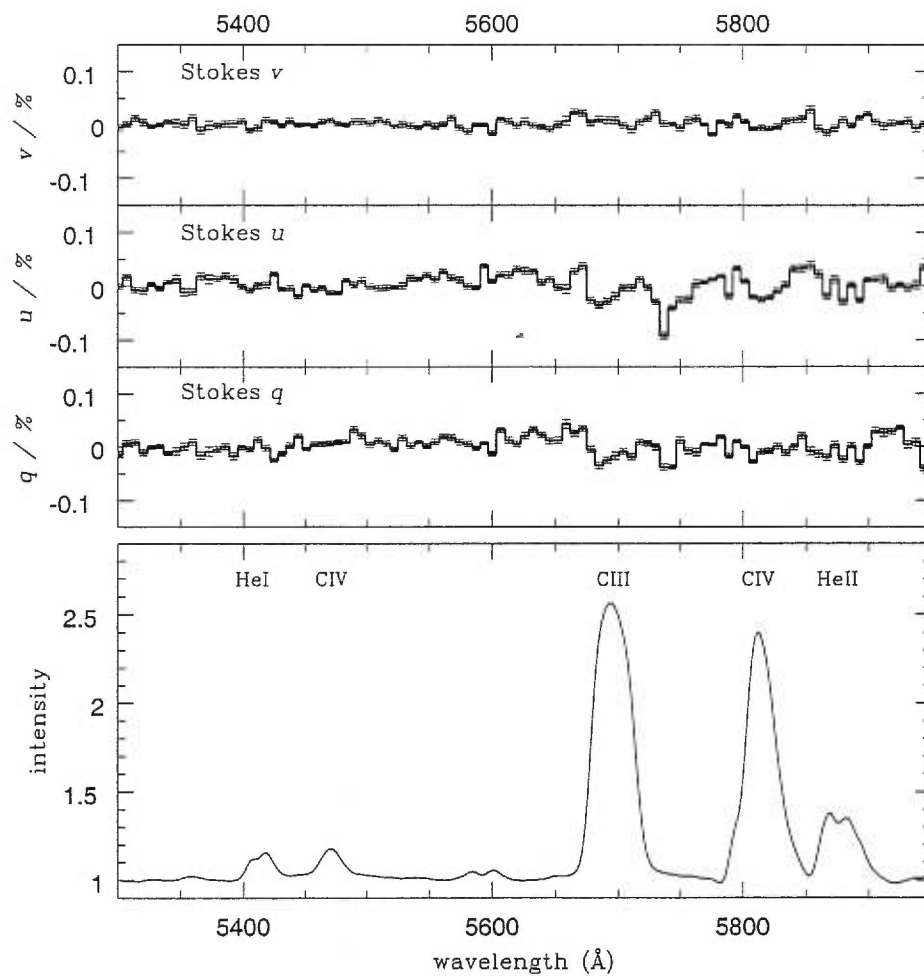
Figure 3.8. Mean rectified intensity spectrum (**bottom**) and mean Stokes q, u and v normalized to zero (**top**) for the whole observing run in the WR frame. The polarimetric data have been binned by a 5-pixel box-car. Formal 2σ errorbars are indicated.

We find no significant circular polarization along the whole mean v_λ spectrum, in excess of the instrumental level of $3\sigma \sim 0.03\%$, although there are hints of variability at the blue edges of C III $\lambda 5696$, C IV $\lambda 5802/12$ and He I $\lambda 5875$. The technique of magnetic field measurement has been described by Landstreet & Borra (1977a, 1977b), Borra & Landstreet (1980) and Landstreet (1977, 1982). Landstreet followed Unno (1956) by using the Milne-Eddington approximation for the source function with presence of polarized light. For this case he derived

$$< v >= 4.67 \times 10^{-13} z B_e \lambda^2 (dI/d\lambda)/I, \qquad (3.8)$$

with $< v >= (v_{red} - v_{blue})/2$, where v_{red} and v_{blue} are the fractional polarizations in the red and blue line wings, respectively; z is the Landé factor and B_e is the net effective longitudinal component of the magnetic field in Gauss. In our case we have no recognizable differences between v_{red} and v_{blue}. For this reason we take $< v > \leq 0.03\%$ (our calculated noise level).

Instead of estimating a magnetic field strength in an absorption line star with a visible photosphere we use this equation for the emission lines from the extended wind in γ^2 Vel. By using eqn. (8) we ignore the Doppler shifts experienced by flux coming from different parts of the stellar wind. On the other hand Mathys (1999) points out that eqn. (8) requires a correction factor of 4/5 to be applicable for emission line stars. By using eqn. (8) and this correction with the Landé factor $z = 1$ for this transition $(3^1 P^0 - 3^1 D)$, the slope of the line flanks and the central line intensity of C III $\lambda 5696$, we translate the instrumental noise level into an upper limit on the net effective magnetic field in γ^2 Velorum: $B_e \leq 280$ Gauss.

3.5 Summary

We have presented phase-dependent spectropolarimetry for the WR+O binary γ^2 Velorum, obtained with the new William-Wehlau spectropolarimeter. In the wavelength range $5200 - 6000$ Å this includes the dominant lines of He II

λ 5411, C IV λ 5471, C III λ 5696, C IV λ 5802/12 and He I λ 5875. All four Stokes parameters I, q, u and v have been obtained quasi-simultaneously during an extended run through periastron passage ($\phi = $ -0.2 to 0.2). We note the following:

1. All five observed major emission lines show small-scale peaks over the broad underlying emission profiles, stochastically changing from night to night and in some nights moving towards the blue/red line wings. These subpeaks are assumed to be a manifestation of localized high density regions (clumps, blobs) created by radiative instabilities (Owocki 1994), outwardly propagating in the wind (cf. Lépine 1998). Their presence in lines of different ionization implies that the whole wind is affected by clumping.

2. Measurements of the line equivalent widths also show significant stochastic variability in the stronger lines of C III λ 5696, C IV λ 5802/12 and He I λ 5875.

3. The variation profiles across the lines, $\sigma(\lambda)$, roughly follow the shape of the emission line profiles themselves, with $\sigma_\lambda/(I_\lambda - I_c) \sim 3 - 10\%$, depending on the line. This indicates that the whole wind is affected by stochastic variations.

4. We find no evidence for a coherent periodic component in the line profile variations of γ^2 Vel, from $\sim$ 6 minutes to 15 days.

5. We make an attempt to disentangle the components of the phase-dependent, variable emission under certain assumptions. This reveals some interesting wind-wind collision effects, with a hint of crashing of the WR wind onto the O star during periastron passage.

6. We report a weak polarization change across the strong emission lines of C III λ 5696 and C IV λ 5802/12, which could be related to the phase-dependent asymmetry created by the O-star light scattered off by free electrons in the WR wind_(Moffat & Piirola 1994).

7. No definite circular polarization is detected in the emission lines above the

instrumental 3σ threshold of 0.03 %, placing an upper limit on the net effective magnetic field in the WR wind, $B_e \leq 280\,\mathrm{G}$.

3.6 Acknowledgments

References

Auer, L.H. & Koenigsberger, G. 1994, ApJ, 436, 869

Bartzakos, P. 1998, Doctoral thesis, Université de Montréal

Bartzakos, P., Moffat, A.F.J., Niemela, V.S. 1995, IAU symp. 163, 406

Borra, E.F., Landstreet, J.D. 1980, ApJ, 212, 141

Cantó, J., Raga, A.C., Wilkin, F.P. 1996, ApJ, 469, 729

Chalabaev, A., Maillard, J.P. 1983, A&A, 127, 279

Eichler, D., Usov, V. 1993, ApJ, 402, 271

Eversberg, T., Lépine, S., Moffat, A.F.J. 1998a, ApJ, 494, 799

Eversberg, T., Moffat, A.F.J., Debruyne, M., Rice, J., Piskunov, N., Bastien, P.,
    Wehlau, W.H., Chesneau, O. 1998b, PASP, 110, 1356

Garrison, R.F., Beattie, B. 1990, JRASC, 84, 246

Gayley, K. G., Owocki, S.P., Cranmer, S.R. 1997, ApJ, 475, 786

Gies, D.R., Bagnuolo, W.G., Jr, Penny, L.R. 1997, ApJ, 479, 408

Harries, T.J., Hillier, D.J., Howarth, I.D. 1998, MNRAS, 296, 1072

Jeffers, S., Stiff, T., & Weller, W.G. 1985, AJ, 90, 1852

Kuhi, L.V. 1973, ApJ, 180, 783

Landstreet, J.D. 1977, AJ, 85, 611

Landstreet, J.D. 1982, ApJ, 258, 639

Landstreet, J.D., Borra, E.F. 1977a, ApJ, 212, L43

Landstreet, J.D., Borra, E.F. 1977b, ApJ, 224, L5

Lépine, S. 1998, PhD Thesis, Université de Montréal

Lépine, S. & Moffat, A.F.J. 1999, ApJ, in press

Lépine, S., Eversberg, T., Moffat, A.F.J. 1999, AJ, in press

Lührs, S. 1991, Doctoral thesis, University of Münster

Lührs, S. 1997, PASP, 109, 504

Marchenko, S.V., Moffat, A.F.J., Eenens, P.R.J. 1998a, PASP, 110, 1416

Marchenko, S.V., Moffat, A.F.J., Eenens, P.R.J., Cardona, O., Echevarria, J., Hervieux, Y. 1997, ApJ, 485, 826

Marchenko, S.V., Moffat, A.F.J., van der Hucht, K.A., Seggewiss, W., Schrijver, H., Stenholm, B., Lundström, I., Setia Gunawan, D.Y.A., Sutantyo, W., van den Heuvel, E.P.J., De Cuyper, J.-P., Gómez, A.E. 1998b, A&A, 331, 1022

Mathys, G. 1999, Proc. IAU Coll. No. 169, in press

Moffat, A.F.J., Marchenko, S.V., Bartzakos, P. 1996, Rev. Mex. AA, conf. series, 5, 38

Moffat, A.F.J., Marchenko, S.V., Bartzakos, P., Niemela, V.S., Cerruti, M.A., Magalhães, A.M., Balona, L., St-Louis, N., Seggewiss, W., Lamontagne, R. 1998, ApJ, 497, 896

Moffat, A.F.J., Piirola, V. 1994, ApJ, 413, 724

Nugis, T., Crowther, P.A., Willis, A.J. 1998, A&A, 333, 956

Pittard, J.M. 1998, MNRAS, 300, 479

Owocki, S.P. 1994, ApSpSc, 221, 3

Roberts, D. H., Lehár, J., & Dreher, J. W. 1987, AJ, 93, 968

Scargle, J. D. 1982, ApJ, 263, 835

Schaerer, D., Schmutz, W., Grenon, M., 1997, ApJ, 484, L153

Schmutz, W., Schweickhardt, J., Stahl, O., Wolf, B., Dumm, T., Gäng, T., Jankovics, I., Kaufer, A., Lehmann, H., Mandel, H., Peitz, J., Rivinius, Th. 1997, A&A, 328, 219

Schulte-Ladbeck, R.E., Eenens, P.R.J., Davis, K. 1995, ApJ, 454, 917

Schweickhardt, J., Kaufer, A., Schmutz, W., Stahl, O., Wolf, B. 1999, Proc. IAU Coll. No. 169, in press

Stevens, I.R., Blondin, J.M., Pollock, A.M.T. 1992, ApJ, 386, 265

Stevens, I.R., Corcoran, M.F., Willies, A.J., Skinner, S.L., Pollock, A.M.T., Nagase, F., Koyama, K. 1996, MNRAS, 283, 589

St-Louis, N. 1996, Rev. Mex., Astron. Astroph. (Ser. Conf.), 5, 76

St-Louis, N., Drissen, L., Moffat, A.F.J., Bastien, P., Tapia, S. 1987, ApJ, 322, 870

St-Louis, N., Willis, A.J., Stevens, I.R. 1993, ApJ, 415, 298

Taylor, M. 1990, AJ, 100, 1264

Unno, W. 1956, Pub. Astr. Soc. Japan, 8, 108

van der Hucht, K.A., Schrijver, H., Stenholm, B., Lundström, I., Moffat, A.F.J., Marchenko, S.V., Seggewiss, W.; Setia Gunawan, D.Y.A., Sutantyo, W., van den Heuvel, E.P.J., De Cuyper, J.-P., Gomez, A.E. 1997, New Astronomy, 2, 245

Walder, R., Folini, D. 1998, A&A, 330, L21

Willis, A.J., Schild, H., Stevens, I.R. 1995, A&A, 298, 549

CONCLUSIONS AND FURTHER PROSPECTS

Conclusions

Wolf-Rayet and O stars and their extended atmospheres show various types of variability. This can be triggered by radially outward moving clumps of plasma, rotationally induced discrete absorption components (DAC) and non-radial pulsations (NRP), extended oscillating equatorial disks and wind-wind interaction in hot star binaries introducing shock-cones. Stochastic variability was detected only in WR stars, so far, and the question was raised if their progenitors, the O stars, show such variability. We answered this question by observing a prototype O star, the early-type O supergiant ζ Puppis:

- We discovered small-scale structures in the He II λ 4686 line of ζ Pup, indicating stochastic density fluctuations (clumps) in the outward moving wind.

- After a detailed investigation we showed that the clumps in He II are formed very close to the stellar surface and are moving radially away from the star. Their acceleration is lower than previously assumed.

- We conclude from variability of the He II λ 4686 line that the whole wind in this line is affected by clumps, similar to WR winds.

- As a consequence of our observations, previously calculated mass-loss rates on the base of a smooth wind are probably overestimated. This likely applies not only to ζ Pup in particular, but to all O stars.

The observation of ζ Pup (a star of 2nd mag) was carried out with the 3.6m Canada-France-Hawaii Telescope. This was indeed a unique campaign, obtaining high signal-to-noise at very high spectral resolution. Encouraged by this success, we completed the construction of the William-Wehlau spectropolarimeter for the observation of hot stars in all four Stokes parameters. This has the tremendous opportunity of obtaining the full description of any stellar light beam; its intensity and all polarization vectors over an extended wavelength range. Besides various technical problems, spectropolarimetry is restricted to sources of large intrinsic polarization or for more typical low levels to big telescopes (longer exposure times would significantly compromise the data quality on short time scales, important for rotating hot stars). Hot stars produce relatively small polarization levels as a rule, so that larger optics are necessary.

Considering the exhausting tests with this new instrument we found some interesting problems, which are probably a general restriction to fiber-fed polarimeter units using multi-layered retarders.

- We found that imperfect framing of the four layers in our two quarter-wave plates introduce varying retardation angles, and hence polarization effects, depending on the orientation angle of the plates. Although this effect can be computed and rejected by a simple reduction procedure it is indroduced by an avoidable manufacturing error. If this problem can be solved by using non-airspaced layers is still an open question.

- A more serious problem is the non-constant sensitivity function of the fibers with respect to the geometrical positions on the apertures. This is clearly proved by a perfect instrumental behavior using overall illumination of the apertures. In our case this is done via flat-fielding. Because of the unpredictable movement of the stellar images during exposure this behavior introduces stochastic variability of broadband polarization. Using Fabry lenses to image the whole telescope aperture on the fibers one could avoid this

problem. For the William-Wehlau spectropolarimeter this idea was rejected due to constructional considerations. If this behavior is due to non-perfect surfaces of the fiber apertures one could carefully glue them onto a transparent plastic plate with a surface of high acuracy.

The compact and simple design of the William-Wehlau spectropolarimeter enables the observer to transport it to various telescopes in both hemispheres. This was carried out during a number of observing campaigns at the Observatoire du Mont Mégantic (OMM) in Québec and at the University of Toronto Southern Observatory (UTSO) in Chile. The results for the WR+O binary γ^2 Velorum, observed through periastron passage at UTSO, are introduced in the present work.

- γ^2 Vel shows highly stochastic variability in all five major observed emission lines, indicating that the whole wind in different excitation stages is clumped. This is most prominent in the strong C III λ 5696 emission, where spectacular features suddenly occur in some nights, only to disappear and be replaced by others in the next night. We confirm previous observations of clumping in C III but over a much longer time scale.

- We find a strong dependence of the C III λ 5696 and He I λ 5875 equivalent widths on the stellar separation ($W_\lambda \sim 1/r$) and significant stochastic variability of W_λ itself.

- We find no evidence for any periodic line variability on time scales from $\sim$ 6 minutes to $\sim$ 15 days.

- Using the minimum profile of the whole run and applying some simple assumptions, we are able to separate out the variable excess emission in the C III emission line, which is shown to be created in a shock-cone around the weaker-wind O star component. The presence of a shock-cone is supported

by the model for wind-wind collisions recently developed by Lührs. However, the results are less clear than in other attempts to apply this model for other systems. By comparing our data with another independent recent investigation of γ^2 Vel, we noticed a swift velocity change in excess C III just before periastron passage. It is possible that we are seeing evidence for the crashing of the WR wind onto the O star surface, provoked by a changing wind momentum balance as the two stars approach each other towards periastron passage.

- Average polarization features of the whole run are found to be significant across C III λ 5696 and C IV λ 5802/12. From circular polarization measurement across the WR lines, we estimate an upper threshold for any magnetic field to be $B_e \sim 280$ Gauss in the system's wind.

Further prospects

The clumpy structure of hot star winds has some interesting implications. One of the most important is the question about the real material input into the interstellar environment. As seen in this report, the winds are filled by density inhomogenities. However, the contrast among these inhomogenities is unknown, as well as the number and size distribution of structures in the wind. It seems that far more structures are present than previously assumed. It may even be possible that fractal structures dominate the wind. If this is true, we need the capacity to observe the real 2-dimensional picture of a hot star with clumpy wind to answer this question. With the advent of advanced high resolution interferometry it should be possible soon to resolve directly at least the closest hot-star winds.

Whether magnetic fields play a role in triggering the mass-outflow, is one of the most intriguing and unanswered questions in the context of hot star winds. No definite value of any magnetic field in any hot star (except Ap and Bp stars) has been measured so far. However, there is every indication that magnetic fields must be present in at least some hot stars. For this reason, the use of spectropolarimety is of high interest for a *direct* detection of the magnetic field. We should make an effort to increase the reliability and accuracy of spectropolarimetric devices to answer this important question.

References

(for the text outside the published papers in chapters 1–3)

Barker, P.K., Landstreet, J.D., Marlborough, J.M., Thompson, I., Maza, J. 1981, ApJ, 250, 300

Beals, C.S. 1929, MNRAS, 90, 202

Borra, E. & Landstreet, J.M. 1980, ApJS, 42, 421

Cassinelli, C.P. & Haisch, B.M. 1974, ApJ, 188, 101

Chandrasekhar, S. 1934, MNRAS, 94, 522

Chandrasekhar, S. 1946, ApJ, 103, 351

Chiosi, C. & Meader, A. 1986, Ann. Rev. Astr. Ap., 68, 415

Conti, P.S. 1976, Mem. Soc. Roy. Sciences Liége, 6e Sér., Tome IX, p.193

Crowther, P.A., Smith, L.J., Hillier, D.J., Schmutz, W. 1995, A&A, 293, 427

Donati, J.-F., Semel, M., Praderie, F. 1989, A&A, 225, 467

Drissen, L., St.-Louis, N., Moffat, A.F.J., Bastien, P. 1987, ApJ, 322, 888

Drissen, L., Robert, C., Moffat, A.F.J. 1992, ApJ, 386, 288

Eversberg, T., Lépine, S., Moffat, A.F.J. 1998, ApJ, 494, 799

Hanuschik, R.W. 1996, A&A, 308, 170

Harries, T.J. 1995, Ph.D. thesis, UCL, London

Harries, T.J. & Howarth, I.D. 1996, A&A, 310, 553

Henriksen, H. 1994, ApSpSc, 221, 25

Kudritzki, R.P., Simon, K.P., Hamann, W.-R. 1983, A&A, 118, 245

Landstreet, J.D. 1979, AJ, 85, 611

Langer, N., Hamann, W.-R., Lennon, M., Najarro, F., Pauldrach, A.W.A., Puls, J. 1994, A&A, 290, 819

Lépine, S., Eversberg, T., Moffat, A.F.J. 1998, ApJ, 514, 909

Lührs, S. 1997, PASP, 109, 504

McLean, I.S., Coyne, G.V., Frecker, J.E., Serkowski, K. 1979a, ApJ, 228, 802

McLean, I.S., Coyne, G.V., Frecker, J.E., Serkowski, K. 1979b, ApJ, 231, L141

Moffat, A.F.J., Drissen, L., Lamontagne, R., Robert, C. 1988, ApJ, 334, 1038

Moffat, A.F.J. & Robert, C. 1992, in: A.S.P. Conference Series, Vol. 22, p. 203

Moffat, A.F.J. & Piirola, V. 1993, ApJ, 413, 724

Nordsieck, K.H. 1992, in: ASP Conference Series, Vol. 22, p. 114

Owocki, S. 1994, ApSpSc, 221, 3

Poeckert, R. & Marlborough, J.M. 1977, ApJ, 218, 220

Puls, J., Kudritzki, R.P., Herrero, A., Pauldrach, A.W.A., Haser, S.M., Lennon, D.J., Gabler, R., Voels, S.A., Vilchez, J.M., Wachter, S., Feldmeier, A. 1996, A&A, 305, 171

Robert, C. & Moffat, A.F.J. 1989a, ApJ, 343, 902

Robert, C., Moffat, A.F.J., Bastien,P., Drissen L., St-Louis, N. 1989b, ApJ, 347, 1034

Robert, C., Moffat, A.F.J., Bastien, St-Louis, N.,P., Drissen L. 1990, ApJ, 359, 211

Robert, C. 1992, Ph.D. thesis, Département de Physique, Université de Montréal

Robert, C., Moffat, A.F.J., Drissen L., Lamontagne, R., Seggewiss, W., Niemela, V.S., Cerruti, M.A., Barrett, P., Bailey, J., Garcia, J., Tapia, S. 1992, ApJ, 397, 277

Roberts, D.H., Lehár, J., Dreher, J.W. 1987, AJ, 93, 968

Scargle, J.D. 1982, ApJ, 263, 835

Schmutz, W., Schweickhardt, J., Stahl, O., Wolf, B., Dumm, T., Gäng, T., Jankovics, I., Kaufer, A., Lehmann, H., Mandel, H., Peitz, J., Rivinius, Th. 1997, A&A, 328, 219

Schulte-Ladbeck, R.E., Nordsieck, K.H., Nook, M.A., Magalhães, A.M., Taylor, M., Bjorkman, K.S., Anderson, C.M. 1990, ApJ, 365, L19

Schulte-Ladbeck, R.E., Nordsieck, K.H., Taylor, M., Nook, M.A., Bjorkman, K.S., M.A., Magalhães, A.M., Anderson, C.M. 1991, ApJ, 382, 301

Schulte-Ladbeck, R.E., Meade, M., Hillier, D.J. 1992, in: L. Drissen, C. Leitherer, A. Nota (eds), Nonisotropic and Variable Outflow from Stars, ASP Conference Series, Vol. 22, p. 118

Schulte-Ladbeck, R.E., Nordsieck, K.H., Taylor, M., Bjorkman, K.S., M.A., Magalhães, Wolff, M.J. 1992a, ApJ, 387, 347

Schulte-Ladbeck, R.E., Nordsieck, K.H., Code, A.D., Anderson, C.M., Babler, B.L., Bjorkman, K.S., Clayton, G.C., Magalhães, A.M., Meade, M.R., Shepherd, D., Taylor, M., Whitney, B.A. 1992b, ApJ, 391, L37

Schulte-Ladbeck, R.E., Eenens, P.R., Davis, K. 1995, ApJ, 454, 917

Schwarzschild, M. 1950, ApJ, 112, 222

Schweickhardt, J., Kaufer, A., Schmutz, W., Stahl, O., Wolf, B. 1998, IAU Colloqium No. 169, Heidelberg

Semel, M. 1989, A&A, 225, 456

Semel, M., Donati, J.-F., Rees, D.E. 1993, A&A, 278, 231

Serkowski, K. 1962, in: Advances in Astronomy and Astrophysics, 1, 247

Serkowski, K. 1970, ApJ, 160, 1083

Stevens, I.R., Blondin, J.M., Pollock, A.M.T. 1992, ApJ, 386, 265

St.-Louis, N., Drissen, L., Moffat, A.F.J., Bastien, P., Tapia, S. 1987, ApJ, 322, 870

St.-Louis, N., Moffat, A.F.J., Drissen, L., Bastien, P., Robert, C. 1988, ApJ, 330, 286

St.-Louis, N., Moffat, A.F.J., Lapointe, L., Efimov, Yu.S., Shakhovskoy, N.M., Fox, G.K., Piirola, V. 1993, ApJ, 410, 342

St.-Louis, N., Willies, A.J., Stevens, I.R. 1993, ApJ, 415, 298

St.-Louis, N., Dalton, M.J., Marchenko, S.V., Moffat, A.F.J., Willis, A.J. 1995, ApJ, 452, 57

St.-Louis, N. 1996, in: *Colliding Winds in Binary Stars*, Rev. Mex., Astron. Astroph., 5, 76

van der Hucht, K. 1996, in: Proc. 33rd Liége Coll., p.1

Willis, A.J. 1991, Proc. IAU Symp. No. 143, p.265

ACKNOWLEDGEMENTS

A short story

DURING OUR SECOND ENGINEERING RUN WITH THE SPECTROPOLARIME-
TER AT ELGINFIELD OBSERVATORY, THE INSTRUMENTAL OUTPUT WAS COM-
PLETELY WRONG. WE COULDN'T FIND THE REASON. AFTER SOME DISCUSSION
JOHN RICE MADE A DECISION... *"Let's pull out the quarter-wave plates..."*. AND
SO WE DID. HE PLACED THEM ON THE TABLE, LOOKED THROUGH WITH A PO-
LARIZER... TURNED THE POLARIZER... LOOKED AGAIN... ?! ... STARED AT THE
WALL ... *"Well...!?!??"* ... AGAIN THROUGH THE QUARTER-WAVE PLATES ... ?!!
... AGAIN AT THE WALL ... *"Hmmm...!"* ... MOUTH OPEN, EYEBROWS TWISTED...
AND SUDDENLY SAID: *"One is turned by 90 degrees!"*

Thank you John for this impressive lesson!